3D food printing: monitoring, quality assessment and adaptation with machine vision

Yizhou Ma

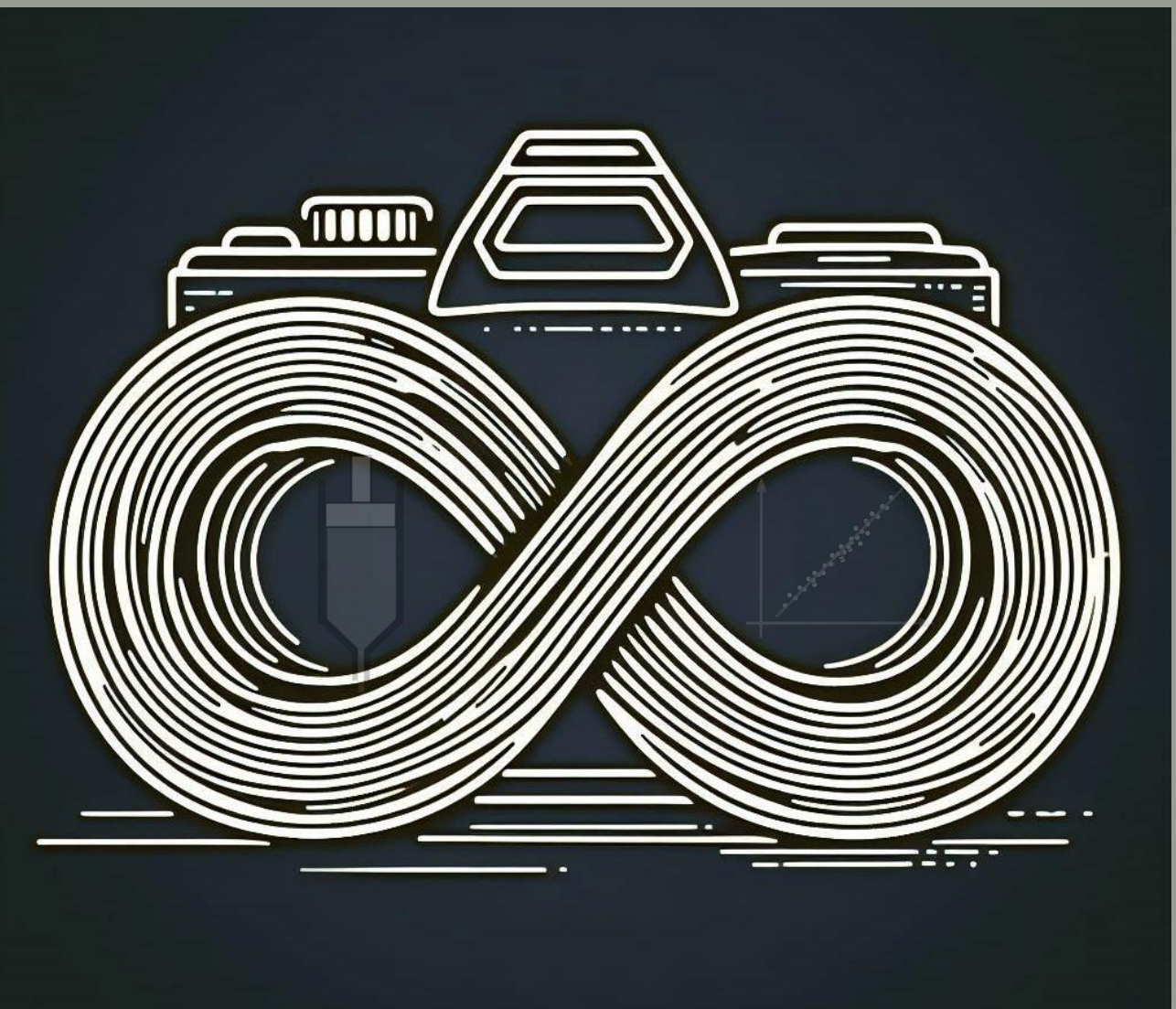

Propositions

1. Food materials are compressible during extrusion-based 3D food printing.
   (this thesis)

2. Printer-derived parameters are more meaningful than instrumental rheology for 3D food printing.
   (this thesis)

3. Data science is in essence a streamlined decision-making process.

4. The best value of artificial intelligence for food science is to predict human sensory perception.

5. Meat is only a flavoring agent in the future of cooking.

6. Realization of complexity impedes drawing conclusions.

Propositions belonging to the thesis, entitled

3D food printing: monitoring, quality assessment and adaptation with machine vision

Yizhou Ma
Wageningen, 28 June 2024

3D food printing: monitoring, quality assessment and adaptation with machine vision

Yizhou Ma

Thesis committee

Promotors
Prof. Dr Remko M. Boom
Professor of Food Process Engineering
Wageningen University & Research

Prof. Dr Maarten A. I. Schutyser
Personal chair at the Laboratory of Food Process Engineering
Wageningen University & Research

Co-promotor
Dr Lu Zhang
Assistant professor at the Laboratory of Food Process Engineering
Wageningen University & Research

Other members
Dr Leonard Sagis, Wageningen University & Research
Prof. Dr Mario Jekle, University of Hohenheim, Germany
Dr Leyla Özkan, Eindhoven University of Technology
Dr Thomas Kodger, Wageningen University & Research

This research was conducted under the auspices of VLAG Graduate School

(Biobased, Biomolecular, Chemical, Food and Nutrition Sciences)

3D food printing: monitoring, quality assessment and adaptation with machine vision

Yizhou Ma

Thesis
submitted in fulfilment of the requirements for the degree of doctor
at Wageningen University
by the authority of the Rector Magnificus,
Prof. Dr C. Kroeze,
in the presence of the
Thesis Committee appointed by the Academic Board
to be defended in public
on Friday 28 June 2024
at 11 a.m. in the Omnia Auditorium.

Yizhou Ma
3D food printing: monitoring, quality assessment and adaptation with machine vision
183 pages.

PhD thesis, Wageningen University, Wageningen, the Netherlands (2024)
With references, with summaries in English

DOI: https://doi.org/10.18174/654521

Table of contents

Chapter 1 Introduction

The food sector always explores new technologies to produce safe, healthy, delicious, and sustainable food products that fulfill the evolving needs of consumers. Personalized foods with customizable design, sensory properties, and nutritional value are attracting growing interests from both individuals and food manufacturers (Derossi et al., 2020). A personalized sensory experience can lead to wellbeing and enjoyment of various food products, while a personalized diet can potentially improve the nutritional intake and thus health. Producing personalized foods requires extensive understanding of food ingredient functionality, processing parameter optimizations, and automated production techniques that allow on-demand preparation. A flexible and autonomous production tool is therefore needed to achieve such production need, and among many technologies, 3D printing presents itself as an enabling method for such personalized food production (Derossi et al., 2021).

1.1. 3D printing for food production

Over the past decades, 3D printing has matured into a rapid production technique in various manufacturing fields including aerospace, construction, and pharmaceutics. 3D printing offers design flexibility and on-demand production that decouples manufacturing from large equipment and fixed production schedules. Among its applications, 3D food printing was first introduced by Periard et al. (2007) in the "Fab@Home" 3D printing model. The concept of a generalized 3D printer was developed to print a wide range of materials including foods based on the extrusion-based printing mechanism similar to 3D printing thermoplastics. Other than extrusion-based 3D printing, technologies such as powder-bed 3D printing also have been explored for food applications (Jonkers et al., 2020; Zhu et al., 2022). However, as its name suggests, powder-bed 3D printing produces food structures using powdered foods, which makes its application unfeasible with most non-powder food materials. Therefore, this thesis will focus on extrusion-based 3D food printing because of its popularity and compatibility to various food materials.

To fabricate food structures using the extrusion-based 3D printing principle, food materials are generally first filled into a holding vessel such as a syringe, extruded through a small nozzle (with a typical diameter of 0.5 – 2 mm), and then deposited onto a motorized platform to print a food structure layer-by-layer. The extrusion-based printing mechanism is intuitive and analogous to piping icing onto a cake. In the context of 3D printing, the "piping" action is automated with a syringe pump and a motorized stage. Generally, the

material is liquified before filling the syringe or liquified in the printer by heating and pressurizing, to allow consistent extrusion from the nozzle. After deposition on the stage, the material has to transition into a solid or a solid-like paste, to ensure retention of the printed shape. This liquid-to-solid transition can be a first order process such as crystallization, or second order (e.g. glass formation, or development of a yield stress). In practice, extrusion-based 3D food printing can be performed either at room temperature or at elevated temperature to allow the liquid-to-solid transition. For example, a dense tomato puree can be extruded and 3D-printed at room temperature as it will develop a (Bingham) yield stress after being deposited, whereas 3D printing of a chocolate structure requires melting for extrusion followed by cocoa butter crystallization upon deposition. Typically, an extrusion-based 3D printer is equipped with a syringe heater to expand its printing material capabilities. The extrusion force can come from different sources such as compressed air, a mechanical piston, or a mechanical screw. Regardless the source of the extrusion force, the goal is to push food material through the thin nozzle and form a continuous filament to deposit food materials layer-by-layer. It is possible to attach multiple printheads onto a mechanical stage, which allows 3D printing of multiple food materials or multiple copies at once. Such an integrated device makes it possible to produce food structures rapidly and flexibly.

Since its debut through Fab@Home, food technologists have started to experiment with extrusion-based 3D printing of various food materials. Suitable food materials for 3D printing are viscoelastic materials such as gels or doughs. Typical food materials used for 3D food printing applications include vegetable puree, cookie dough, jam, chocolate paste, etc. These food materials can be directly 3D-printed into creative and visually appealing designs to attract consumer interests. An iconic 3D food printing material is chocolate. Due to its suitable physical properties and popularity with consumers, specialized chocolate 3D printers have been developed and can now be found in bakeries, chocolatiers, and restaurants. Because its initial attempts stimulated the interests of the food industry and research institutions, since 2015, a fruitful number of scientific studies have been conducted to explore 3D food printing as a potential method to produce foods.

1.2. Advances and challenges of 3D food printing

After experimenting with ready-to-print food materials, food technologists focused on formulating 3D printable food materials from various ingredients. For example, different food hydrocolloids (carrageenan, alginate, xanthan, etc.) have been used to formulate hydrogels and sometimes encapsulated systems for 3D food printing applications (Liu et al., 2019). Using hydrocolloids changes the rheological properties of food printing materials and improves the stability of 3D-printed food structures (Kim et al., 2018). Sensory evaluations of 3D-printed foods were also reported in various studies, to show the added values of using 3D printing. By customizing food designs, 3D-printed foods can provide unique sensory experiences by altering the texture and flavor perceptions of the consumers. Specific applications of 3D food printing emerged towards special consumer groups. 3D-printed foods are formulated and fabricated for patients with dysphagia to accommodate swallowing difficulties with soft and flowable food materials with an appealing appearance (Pant et al., 2021). Personalized snack bars were 3D-printed and served to Dutch military personnels as an exploratory study of on-demand food personalization (Caulier et al., 2020). Moreover, with the design flexibility in the food printing materials, functional materials have been prepared to achieve 4D printing applications of foods. On top of the 3 physical dimensions, time is here considered as the 4th dimension: 4D printed foods can show changes in color, shape, and mechanical behavior (Teng et al., 2021).

Previous research focused on formulating suitable food printing material and developing prototypes of personalized 3D-printed foods (Derossi et al., 2021). These studies were often realized based on extensive trial-and-error experiments, which leads to excessive investment in time and raw materials. Minimal research effort has been devoted to automatically optimize 3D food printing parameters for a diverse range of food materials. Moreover, the performance of 3D food printing is often manually inspected by experienced operators, making it difficult to standardize and scale up to meet the growing demand of the market. The relatively inefficient operation of 3D food printing makes it challenging to establish streamlined production of personalized foods. Even with successful proof-of-concept applications, 3D food printing at this moment still lacks the availability of robust software and hardware (i.e. 3D printer, controller, and accessories) to achieve timely and accurate printing of foods that are ready for the consumer market.

1.3. Monitoring food processes with machine vision

3D food printing is a demonstration of food production being digitized and automated with advanced manufacturing techniques. The idea of designing in digital space and fabricating food structures on-demand exemplifies the power of automation in today's manufacturing. To better monitor and control manufacturing, standardized data collection methods based on sensing techniques become necessary. Implementing sensors into food processes becomes more common, made possible by the reduced hardware costs, abundant computational resources, and progress in algorithmic development. Among all types of sensors, digital cameras are gaining popularity due to their compatibility with existing hardware and advancements in data analysis. Specifically, machine vision technologies integrate cameras with processing equipment to collect image and video data, extract meaningful information, and derive control actions. Machine vision has accomplished various tasks in our daily life including production quality inspection, autonomous vacuum cleaning, fruit sorting and packing, etc. 3D food printing as used in this thesis serves as a concrete example of a food process that benefits from better use of sensing and control, but the results will also be relevant for other types of food processes.

Analyzing images of food or food processes is not a new idea. Since the 1980s, food scientists have applied image analysis methods to measure the physical dimensions of food products, extract light intensity to quantify compositions in microscopic images, and guide the sorting process of fruits and fishery goods (Gunasekaran, 1996; Kaláb et al., 1995). Monitoring food quality has been a primary application of machine vision in food processing since its detection mode is similar to that in human (visual) inspection. In recent years, multi-modal imaging techniques have been developed based on hyperspectral imaging, 3D imaging based on lidar sensors, and infrared thermography. These techniques enable the detection of "invisible" properties such as food composition and temperature changes during food processing (Feng & Sun, 2012). Notably, an advancement of machine vision in food production is the transition from inspection and monitoring to controlling a process. Integrating image acquisition, data analysis, and actuation (i.e. parameter adjustments) is a new field for machine vision application in food manufacturing. The concept of vision controllers allows implementing the information learned from machine vision into a specific action or adjustment of the process. Some early demonstrations of such integrated systems have been applied to fruit

sorting and meat packing, with the expectation that such machine-vision-based systems will be further integrated into the production of formulated foods (Nandi et al., 2014; Taheri-Garavand et al., 2019). Outside of the food industry, machine vision techniques have been applied to monitor and perform corrective actions on 3D thermoplastic printing (A. Petsiuk & Pearce, 2020; A. Petsiuk & Pearce, 2022). Therefore, 3D food printing allows itself as a potential field of first application for machine vision-based food process control due to its small physical footprint, rapid manufacturing speed, and capability of printing a diverse range of food materials.

The data collected by machine vision technologies can be transformed into predictive models, to better understand the process dynamics. Accumulation of structured data can be used to create a set of data-driven models that focuses on pattern recognition and statistical learning from existing data. Vision systems combined with artificial neural networks have been applied for quality inspection and process control purposes (Fan et al., 2013). Such a data-driven approach bypasses mechanistic modelling of complex physical phenomena, various length scales, and heterogenous structures, which are often seen in food systems. Because these models primarily concern linking inputs with outputs, such black-box models can however struggle with interpretability, and are generally only reliable within the parameter space covered by the dataset. To overcome these difficulties, a combination of white and black box models (i.e. "grey box models") can be used to both leverage mechanistic insights and embrace complex patterns found in prior data. Such models found their first applications in postharvest technology (Verboven et al., 2020). The combination of sensing technologies and mass and heat transfer models can establish a solid basis to virtually represent a physical fruit production process. Irrespective of the modeling methods, a constant pursuit involves rapidly collecting and effectively utilizing vision data to optimize future food productions.

1.4. Aims and outline of this thesis

Sensor integration and predictive modeling have empowered the digital optimization of diverse manufacturing processes. The central hypothesis of this thesis therefore is that machine vision techniques can improve the extrusion-based 3D food printing performance by automating its parameter optimization for a diverse range of food materials. To explore this hypothesis. this thesis aims to develop a set of methods to digitally monitor, evaluate,

and optimize the 3D food printing process based on machine vision. A combination of monitoring and modelling techniques is expected to streamline the 3D food printing process to achieve "first-time-right" manufacturing. Specifically, image-based techniques are developed to rapidly and automatically measure material flow and physical dimensions of 3D-printed food structures. The obtained information is connected to fundamental theories in food rheology and used to guide printing parameter optimizations such as adjusting printing pressure, speed, and extrusion retraction. Meanwhile, the auto-collected data are fit into predictive models based on the grey-box modelling principle. In the meantime, the image-based measurements were contextualized to assess their consumer-relevance and to determine corrective actions.

Figure 1.1 offers an overview of the chapters in this thesis. Specifically, **chapter 2** provides an overview of the state-of-the-art development of 3D food printing for personalized food production. While application studies indicated that 3D food printing can customize appearance, texture, and flavor of foods, we identified a lack of research effort into 3D food printer development and digital optimization of 3D food printing processes.

To implement digital optimization of 3D food printing, various machine vision techniques are developed by following its process steps, namely filament formation (1D), layer stacking (2D) and finally structure building (3D). **Chapter 3** focuses on quantifying and predicting the line extrudability of food materials with diverse rheological properties. The chapter demonstrates automated data collection and data-driven model development based on insights from mechanistic models and machine learning. Following the learnings from Chapter 3, **Chapter 4** takes a different approach to characterize food material extrudability through near-real-time measurements. This chapter then evaluates the feasibility of using measured material flow information for calibration-based control optimization.

After optimizing the 1D line extrudability of food materials, this thesis proceeds with optimization of the structural stability and layering accuracy in the 2D space. **Chapter 5** applies thermographic imaging to monitor the structural deformation of hot-extrusion food printing. The obtained temperature and deformation data are connected to various rheological measurements to understand the best practice of hot-extrusion food printing.

Then, **Chapter 6** develops an automated image analysis method to evaluate the layer printing accuracy of foods. This method is contextualized based on human assessment to identify relevant corrective actions to achieve consumer-perceivable layer accuracy for 3D food printing. Finally, **Chapter 7** demonstrates an application of modulating food texture through digital designs. This chapter characterizes the fracture behavior of food structures with different designs and illustrates the application of 3D food printing as a method to reliably print food texture designs. Based on all findings in this thesis, **Chapter 8** summarizes the main takeaways from this digital optimization effort and provides additional reflections on extending digital optimizations to other forms of food processes.

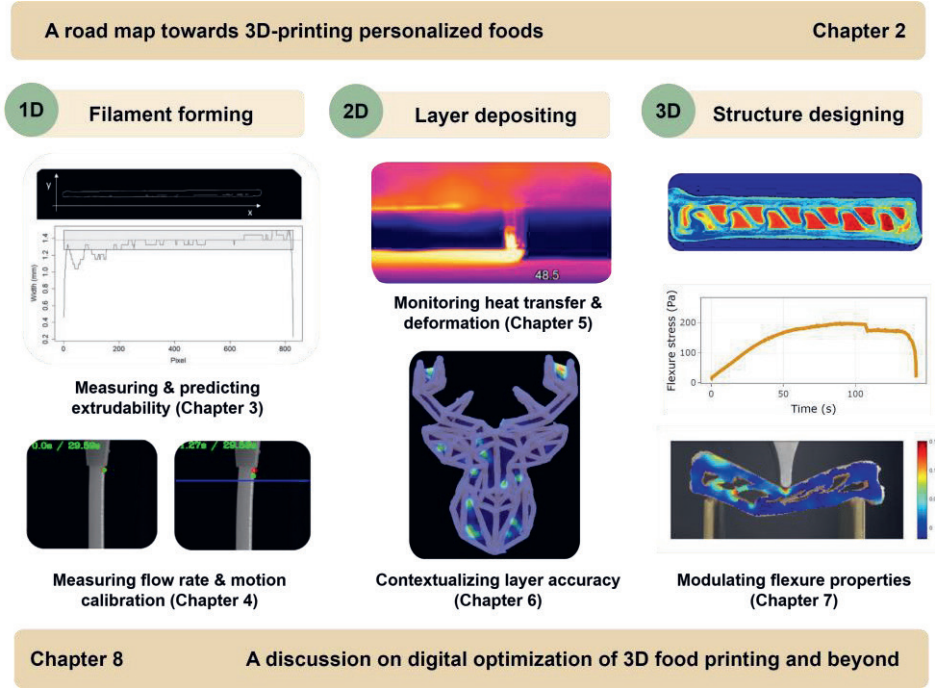

Figure 1.1. A graphic overview of experimental chapters in this thesis.

Chapter 2 Formulated food inks for extrusion-based 3D printing of personalized foods: A mini review

This chapter has been published as: Ma, Y., & Zhang, L. (2022). Formulated food inks for extrusion-based 3D printing of personalized foods: a mini review. Current Opinion in Food Science, 44, 100803.

Chapter 2

Abstract

3D food printing is an emerging technology to structure foods from digital designs. A number of food inks are formulated to 3D/4D print foods with customized appearance. This mini review focuses on the recent developments in 3D printing of personalized foods with modified sensorial properties (e.g. texture and flavor). Varying sensory perceptions of printed food could lead to eating behavior changes among consumers and potentially achieve personalized nutrition. Modifying geometric designs and varying spatial distributions of ingredients are common techniques to alter sensorial properties of printed foods. The high degree of customization of 3D food printing indicates its potential as an on-demand production tool for personalized foods. Nevertheless, we suggest that longitudinal consumer insights and robust printers are needed to further achieve 3D printing of personalized foods.

2.1. Introduction

3D printing, also known as additive manufacturing, refers to the construction of 3-dimentional objects from digital designs. Since 2007, researchers attempt to develop 3D food printing technology to customize food designs, personalize nutrition, simplify the food supply chain, and broaden future food sources (Derossi, Caporizzi, Paolillo, Oral, et al., 2021). Extrusion-based 3D printing is the most common technology to print food materials, compared to other technologies such as laser sintering or inkjet printing. In extrusion-based printing, a motorized syringe extrudes food materials onto a platform, and the object is built layer by layer based on a predesigned digital model. A variety of food materials has been formulated as food inks for 3D printing purposes. The food inks are often viscoelastic, to provide necessary structural integrities while remain extrudable through the printing nozzle (Wilms et al., 2021.).

To develop such food inks, researchers adopted existing food materials (i.e. chocolate and cookie dough) into 3D printing applications (Hao et al., 2010; Lipton et al., 2015). Also, various food hydrogels, protein dispersions, and emulsion gels were formulated to be 3D-printable (Siacor et al., 2021). These adopted and formulated food inks are often studied for their 3D-printability (e.g. extrudability and self-supporting stability). Successful printing of those inks into stable shapes showcased 3D printing as a way to customize food designs. Customizable foods can assist designing personalized diets which could lead to eating behavior improvement and better nutritional well-being for long-term health of individuals (Celis-Morales et al., 2017; Zeevi et al., 2015). The increased degree of customization can also adjust functional nutrient dosage, release profile, and duration similar to 3D-printed medicine (Tan et al., 2020). Therefore, 3D food printing shows its potential use to produce on-demand and personalized foods that meet preferences and nutrition needs from consumers.

In previous reviews, authors have discussed a wide range of food materials in terms of printing feasibility, formulations, printing parameters, and post-processing techniques for 3D printing (Siacor et al., 2021; Zhang et al., 2021). In this mini review, we focus on various extrusion-based food inks that are developed for producing personalized foods. We discuss food personalization via 3D printing from three aspects, i.e. appearance customizations, flavor and texture modifications, and eating behavioral influences. The common

personalization strategies are listed and discussed to provide guidelines for future sensorial modifications. Finally, we point out several challenges and opportunities to further realize personalized foods through 3D printing.

2.2. The food ink evolution for personalized foods

Food inks have been developed to enable various degrees of customization for 3D food printing. An evolution of food inks with increasing technical complexity and consumer involvement is observed from the recent research outcomes. In this section, we discuss the food ink evolution for personalization based on appearance customizations, texture and flavor modifications, and satiety and eating behavioral influences.

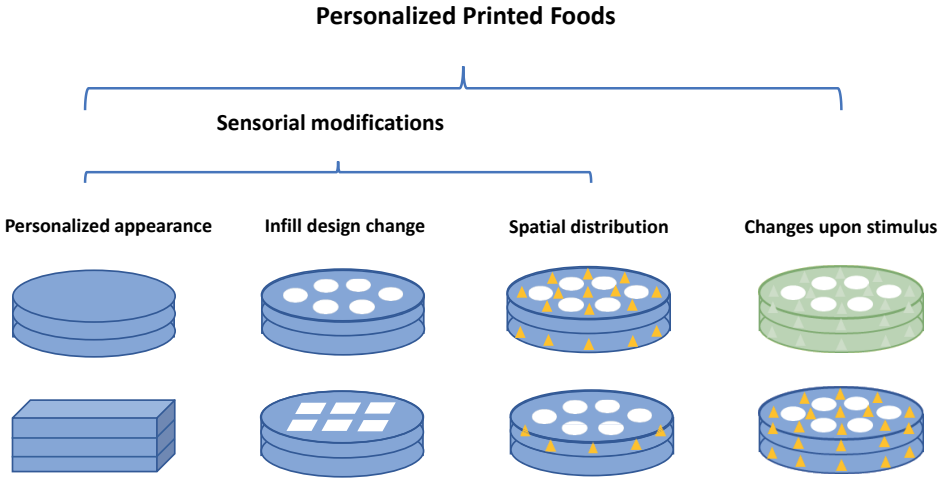

Figure 2.1. Schematic illustrations of 3D/4D printed foods that are personalized at different levels: white cycles and rectangles indicate different infill designs in the structure; orange triangles indicate functional ingredients that are distributed differently in structures; and color change is indicated by the change from green to blue color as an example of stimulus-responsive transformations of 3D-printed foods.

2.2.1. Appearance customization

The early attempts of extrusion-based 3D food printing focused on printing food inks into customizable shapes. Those food inks were often adopted from ready-to-eat or prepared recipes. Lipton et al. listed then-available food inks such as chocolate, meat pastes, vegetable purees, and cookie dough (Lipton et al., 2015). Because of chocolate's unique material properties and popularity among consumers, specialized chocolate printers were developed

and commercialized for confectionary design and manufacturing purposes. Several fundamental studies also investigated how chocolate compositions and processing influence its printability (Rando & Ramaioli, 2021). In recent studies, a variety of printable food inks has been developed such as protein gel, starch gel, and emulsions. Godoi et.al. reviewed the 3D printability of food inks as influenced by their compositions (ratios of macronutrients), which is strongly linked to the rheological properties of the inks (Godoi et al., 2016). In some other studies, additives such as hydrocolloids are often formulated into food inks to improve their 3D-printability (Zhang et al., 2021). These food inks were generally developed to showcase 3D printing as a tool to fabricate foods with a stable and customized shape (see Figure 2.1), rather than providing certain functionalities.

Moving beyond printing food into customizable and stable shapes, researchers utilized 4D printing to further modify appearance of printed foods. Over time, 3D-printed food materials can have color, shape, or flavor transformations (i.e. the 4th dimension) induced by internal or external stimulus such as pH, the availability of water (e.g. hydration or dehydration), and heat (e.g. microwave cooking) (see Figure 2.1) (Teng et al., 2021). As reviewed by Teng et al., functional ingredients such as colorants, dielectric regulators (i.e. salts and syrup), flavors, and bioactive compounds are formulated into the base inks for 4D food printing. For example, a color change of printed food was achieved by dual-extruding layers of two types of potato starch gels containing either anthocyanin (as the functional material) or lemon juice (as a pH stimulus) (Ghazal et al., 2019). Over a period of 30 min, the color of the printed layers of anthocyanin-containing gel intensified due to change of its pH which is caused by the redistribution of hydrogen ions within the matrix. In another study, shape changes of starch-based foods were induced by microwave dehydration. He et al. investigated the degree of shape changes as controlled by changing ink formulations, microwave power, and infill patterns (He et al., 2020). This study suggested that the addition of syrup and salts can influence both the rheological properties of the food ink and structural changes induced during microwave cooking. To summarize, in the case of 4D printing, functional properties of the food inks are specifically developed to showcase appearance customizability of 3D printing for personalized food designs.

2.2.2. Textural and flavor modifications

As a structuring tool, 3D printing can alter micro- and macro-structure of foods. By using digital design software, the infill density and pattern for a 3D object can be controlled. The change in infill can subsequently impact the texture of the printed food structure (see Figure 2.1). Derossi et al. structured bigger pores in cereal cubes via 3D printing compared to those produced by conventional processing methods. As a result of the microstructure changes, the hardness, chewiness and cohesiveness of 3D-printed samples after baking were higher than the manual-shaped ones. The authors further conducted textural modifications through a controlled generation of pores in the food matrix, to "program" the texture of cereal-based foods (Derossi, Caporizzi, Paolillo, & Severini, 2021). A similar approach was found in developing 3D-printed potato snacks varying in texture by changing infill patterns and densities during printing (Liu et al., 2020; Liu & Zhang, 2021). Modifying the infill of a food design has become the common method to alter food texture, providing opportunities for customizable food texture via 3D printing.

While texture modifications of printed foods are often characterized by instrumental analysis (e.g. texture profile analysis), data obtained from sensory panels are still limited in literature. Therefore, it is sometimes difficult to confirm texture modifications would result in actual changes of consumer perceptions. Mantihal et al. evaluated the sensorial properties of 3D-printed chocolate with different levels of infills (Mantihal et al., 2019). Although the hardness of samples with various infill levels differed significantly as measured by a texture analyzer, the sensory study found no significant difference in hardness perceived by 30 semi-trained panelists. In a different study (Zhu et al., 2021), the authors modified the infill patterns of 3D-printed protein bars to examine the hardness perceived by 70 untrained panelists. This study showed that the concentric infill pattern resulted in higher perceived hardness compared to the rectilinear and layered patterns, which agreed to the instrumental analysis. Meanwhile, the authors found that modifying infill patterns did not impact consumer liking of the protein bars and suggested that 3D printing can be a viable technique for textural modifications of solid foods. For future research, combining instrumental analysis with sensory tests could provide further knowledge about how changes in food structure could impact its texture.

Flavor modifications were also attempted in previous studies by controlling the spatial distribution of ingredients in a food matrix using 3D printing (see Figure 2.1). Modifying flavor perceptions can potentially improve consumer preferences and achieve sugar, salt, and fat reductions in food formulations. For example, a chocolate layer with varied levels of thickness (as a way to change sugar content) was deposited onto rice waffles using 3D inkjet printing to create bite-to-bite difference of sweetness (Zhu et al., 2020). The sensory evaluation showed that the bite-to-bite variation created by 3D printing affected sweetness, expected fullness, and liking of the samples. The study concluded that the flavor modifications by 3D food printing can contribute to healthier food designs, creating similar sensory perceptions with less undesirable ingredients such as sugar. In a different study, dual-extrusion was used to stack salted and unsalted layers to structure starch snacks (Fahmy et al., 2021). Based on results from a trained sensory evaluation, the inhomogeneous distribution of salt enhanced the saltiness perception, which can be used as a strategy for salt reduction in real food applications. Similarly, different lemon mousse formulations were layered into one structure to provide layer-by-layer variations in sweet and sour perceptions (Chow et al., 2021). Although no significant difference in preference was found between the multisensory layered and control samples, the authors suggested that the multisensory layered design can be tailored towards preferences of specific consumer groups. Also, flavor modifications can be achieved using 4D printing. A controlled release of encapsulated cinnamaldehyde and pepper red pigments was developed for 3D-printed buckwheat snacks by microwave heating (Guo et al., 2021). Upon microwave cooking, the buckwheat snacks released spicy flavors from cinnamaldehyde and changed color. Combining functional food inks with different 3D printing strategies (e.g. dual- or coaxial-extrusion of multiple materials), we can summarize sensorial modifications of 3D-printed personalized foods through altering appearances, textures, and flavors (see Table 2.1).

The available sensory studies provided empirical data to show the impact of food designs via 3D printing on texture and flavor perceptions. However, 3D food printing's specific influence on consumer preferences still remains challenging to characterize due to the lack of longitudinal consumer studies. On the individual level (i.e. consumer studies), a feedback loop for consumer preferences is needed to fully test the concept of personalized food produced by 3D printing. In an exploratory study, the authors collected consumer insights

from 12 Dutch soldiers after consuming 3D printed foods for 4 weeks (Caulier et al., 2020). The soldiers consumed and rated personalized snack bars based on texture (crunchy or soft) and flavors (distribution of fillings). The study reported that an increase of personalization improved the overall liking of the snack bars, indicating that 3D printed foods can tailor their sensory profiles based on consumer needs. To further advance food personalization, consumer involvement is needed to test whether texture and flavor modifications based on 3D printing can fulfill consumer needs and improve food liking.

Table 2.1. Representative studies that achieved sensorial modifications of food through 3D printing

Modifications	**Modification aim**	**Printing materials**	**Modification strategies**	**References**
Appearance	Color changes	Starch gels	Dual-extrusion to achieve acid fusion among anthocyanin-containing layers	(Ghazal et al., 2019)
Appearance	Shape changes	Purple sweet potato purees	Controlling infill patterns and dielectric properties during microwave heating	(He et al., 2020)
Appearance / Flavor	Color and aroma changes	Buckwheat dough	Controlled release of aroma and color compounds by microwave heating	(Guo et al., 2021)
Texture	Hardness and chewiness changes	Cereal-based snacks	Infill densities and patterns to generate different porous structures	(Derossi et al., 2021)
Texture	Hardness and fracturability changes	Potato snacks	Infill densities and patterns modifications	(Liu et al., 2020; Liu et al., 2021)
Texture / Preference	Hardness and overall preference	Dark chocolate	Infill densities modifications	(Mantihal et al., 2019)
Texture / Preference	Hardness, chewiness, and overall preference	Protein bar filled with chocolate	Infill patterns modifications	(Zhu et al., 2021)
Flavor / Preference	Sweetness, expected fullness, and overall preference	Chocolate on rice waffle	Spatial distribution of chocolate on a single layer	(Zhu et al., 2020)
Flavor	Saltiness	Starch-based snacks	Dual-extrusion of salted and unsalted layers	(Fahmy et al., 2021)
Flavor	Sweetness and sourness	Lemon mousse	Dual extrusion to create layer-by-layer flavor variations	(Chow et al., 2021)
Flavor	Customizable flavor profiles	Snack bar	Spatial distribution of different flavor fillings	(Caulier et al., 2020)

2.2.3. Satiety and eating behavioral influences

Changing food perceptions may lead to positive changes in eating behavior among consumers. To study such effect, consumer involvement is needed. A food personalization system named "FoodFab" offered a proof-of-concept for personalizing calory intakes on the individual level (Lin et al., 2020). The system aims to alter the food's internal structure and overall appearance (i.e. size) to influence chewing time, which can subsequently determine the perceived satiety. Based on the calorie requirement of the user, the system calculates the necessary chewing time and print a specific cookie by altering the infill patterns and density. This study shows the infill density and size significantly affected both the chewing time and perceived satiety of the participants, when the infill pattern and overall calory/mass of the samples were kept the same. Specifically, the sample with the lowest infill density hence the largest size required the longest chewing time and was perceived with the highest increase of satiety. FoodFab served personalized foods based on individual's calorie needs and created the feedback loop by asking the perceived satiety level. Although with limited food options and only targeting satiety, the concept provided in this study may be expanded to other personalization objectives such as reducing sugar and fat intakes and dosing nutraceuticals.

2.3. Challenges and outlooks

While the variety and functionality of food inks keep expanding, applications of 3D food printing to prototype and produce personalized foods remain at the conceptual stage. Here, we propose a road map to produce scalable and deployable personalized foods based on 3D printing (see Figure 2.2).

On Stage 1, studies have leveraged insights from colloidal science and food engineering to develop food ink formulations with good 3D printability. However, most of the 3D food printers used in current studies are either custom-built or modified from a plastic printer. Limited commercial printers are available to 3D print food materials. Unlike printing plastics, food materials are diverse and complicated in rheological properties, requiring a wide range of printing conditions to achieve proper structuring (Wilms et al., 2021). Currently, due to the complexity in the rheological properties of food materials, extensive trail-and-error experiments are needed to find the proper printing conditions for a chosen food ink. The lack of quantitative printability evaluation made it difficult to achieve automated food

printing. In some recent studies, vision sensors (e.g. optical/thermal cameras) are used to study the extrusion-based 3D printing of food materials. The data acquired by these sensors during printing experiments are used to quantitatively evaluate 3D printability of food materials (Fahmy et al., 2020; Ma et al., 2021). Structured database of sensor and image data can further develop predictive models to link the printability of food inks to their rheological properties and printing conditions.

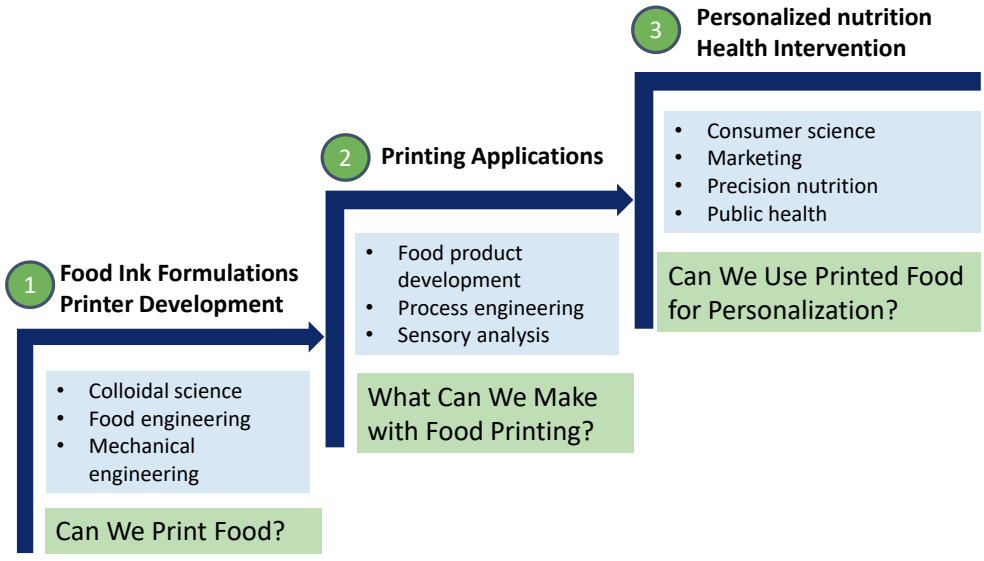

Figure 2.2. A proposed road map for 3D food printing as a tool to produce personalized foods. Stage 1: Food ink formulation and printer development. Expertise from colloidal science, food engineering, and mechanical engineering can help us to answer the question whether we can print food. Stage 2: Printing applications. Expertise from product development, process engineering, and sensory analysis can help us to find out what we can make using 3D food printing. Stage 3: Food personalization and health intervention. Expertise from consumer science, marketing, precision nutrition, and public health can understand whether printed foods can achieve food personalization.

In addition, the current 3D food printers featured in literatures were either modified from plastic or bioprinters which operate at relatively low throughput for proof-of-concept applications. Material elasticity and solidification limits the current printers to print at high speed and act as on-demand food production tools for consumer studies. To facilitate the production of personalized foods, robust food printers combined with integrated software controls are needed to adapt printing conditions based on food ink properties (Jayaprakash et al., 2020). The future spread of personalized foods well depends on the robustness of

food printers to accurately and timely produce food products as requested by individual users.

On Stage 2 (Figure 2.2), 3D food printing has been experimented as a product development tool to provide customizations and modifications discussed in earlier sections. Also, 3D bio- or food printing has been used to prototype and produce meat alternatives such as cultured meat or plant-based meat replacers, which may contribute to the sustainable development of food production.

To advance towards food personalization (Stage 3, Figure 2.2), we also need more insights from consumer and nutritional studies. Consumer studies focusing on individual customizations should be performed to examine the current 3D food printing capabilities and the consumer acceptance of 3D-printed foods. Meanwhile, recent studies have shown that 3D-printed foods can achieve sugar, salt, and fat reductions with the potential to maintain the original sensory profile (Shahbazi et al., 2021; Zhu et al., 2020, 2021). Therefore, longitudinal studies may be needed to link long-term consumption of 3D-printed foods with potential health benefits. Similarly, food inks were formulated to act as delivery systems for other bioactive compounds. Customizing nutrient delivery to fulfill specific nutritional needs can be a subsequent study topic for personalized foods based on 3D printing. In addition, food for special groups such as dysphagia patients can also be produced by 3D food printing. Several studies have explored the formulations and potential health benefits of using 3D food printing to produce foods for dysphagia patients (Lee et al., 2021; Pant et al., 2021).

2.4. Conclusions

The extrusion-based 3D food printing technology suits the needs for producing personalized foods. Thanks to the extensive development of functional food inks, 3D printing can alter appearance and sensorial properties of foods, to potentially meet consumer preferences and impact consumer eating behaviors. Controlling printing infills and the spatial distribution of ingredients are the common strategies to modify texture and flavor perceptions of printed foods. Future research is needed for longitudinal studies in terms of consumer acceptance of 3D food printing and potential health impacts by consuming printed foods.

To further advance personalized food productions, robust 3D food printers are also needed to timely and accurately fabricate food designs using a wide range of food inks.

Chapter 3 Predicting the extrudability of complex food materials during 3D printing based on image analysis and gray-box data-driven modeling

This chapter has been published as: Ma, Y., Schutyser, M. A. I., Boom, R. M., & Zhang, L. (2021). Predicting the extrudability of complex food materials during 3D printing based on image analysis and gray-box data-driven modelling. Innovative Food Science & Emerging Technologies, 73, 102764.

Chapter 3

Abstract

Material extrudability is a prerequisite for printing 3D structures with extrusion-based food printing. Food materials with different shear-thinning behaviors were printed to develop predictive models for extrudability. A dataset of 131 unique combinations of materials and printing parameters was collected. Image analysis was employed to rapidly quantify extrudability as determined by mode width, line height and width consistency of line filaments. The relation between the printing pressure and the volumetric flow rate followed a power-law relation, which characterizes the extent of shear-thinning of the food materials. Both regression and classification models were trained and tested using the random forest algorithm. The model performance indicated that extrudability can be predicted with moderate to high accuracy by using rheological measurements and printing parameters as inputs. The predictive workflow developed in this study provides a framework to quantitatively assess and predict extrudability for 3D printing of complex food materials.

3.1. Introduction

3D printing offers flexible and rapid prototyping for many sectors including medicine, engineering, manufacturing, art, and education (Dankar et al., 2018). Since 2005, 3D food printing technology has been developed as a tool to customize food designs, personalize nutrition, simplify the food supply chain, and broaden the future sources of our food (Liu et al., 2017). One of the common printing mechanisms for food materials is extrusion-based 3D printing. A motorized syringe controlled by a robotic system extrudes food materials onto a platform, and the object is built line by line and layer by layer based on a predesigned digital model. A variety of food materials such as soy protein, rice starch, and mashed potatoes have been formulated and printed into different geometries. These initial applications showed that extrusion-based 3D food printing has potential for rapid and flexible food product creations (J. Chen et al., 2019; Liu et al., 2020; Theagarajan et al., 2020).

Evaluating the printability of materials is key to success in developing 3D printing applications. Printability is defined as the ability of 3D printing to closely reproduce a target digital design (Telea & Jalba, 2011). 3D printability of food materials is known to be co-determined by their rheological properties. However, the detailed relation between rheology and printability has not been fully elucidated due to the complexity and variability in the composition of food printing materials (Liu et al., 2019). Previous research showed that the flow stress, storage modulus, and zero shear viscosity of food materials are all correlated to the printability in specific model systems (H. Chen et al., 2019; Costakis et al., 2016; Yang et al., 2018; Zhu et al., 2019). Besides rheological parameters, studies have identified that printing parameters such as layer height, infill percentage, and nozzle movement speed that co-determine the 3D food printability (Huang et al., 2019; Severini et al., 2018). Success in printing 3D structures requires accurate extrusion of individual line filaments (1D structures), also known as extrudability. Ensuring the extrudability of food materials is an important step towards achieving subsequent 3D printability aspects such as shape fidelity and retention over time (He et al., 2016; Schwab et al., 2020). Extrudability is assessed by continuous extrusion and the uniformity of the filament. Liu et al. (2019) suggested that yield stress and pseudoplasticity are closely related to the extrudability of food hydrocolloids. Moreover, printing parameters including printing pressure, nozzle speed, and nozzle height

have been identified as factors that co-determine the extrudability and printability of alginate/gelatin hydrogels (He et al., 2016).

Automatic, rapid and quantitative assessments of material extrudability are useful when developing novel ingredients for 3D food printing purposes (Pérez et al., 2019). In addition, practical employment of 3D printing should be robust against variations and changes in printing materials. Simple and automated methods are needed to optimize the printing parameters to achieve the best performance of the printing system. Several methods have been developed to assess the extrudability of biological and food printing materials. For example, a simple dispensing method was proposed by Paxton et al. (2017) to manually press printing materials through a syringe and evaluate continuous filament formation and morphology based on visual observations. This method constitutes a qualitative test for initial screening of printing materials, but lacks the evaluation of other printing parameters. Another common method is to measure the extruded line dimensions from microscopic and optical images. He et al. (2016) measured the printed line width of hydrogels using a digital microscope, and other studies have used image analysis software such as ImageJ to manually measure line dimensions from optical images (Lanaro et al., 2017; Nijdam et al., 2021). Recently, Fahmy et al. (2020) developed a camera-based method to automatically measure the extrudability of cereal-based printing materials. This technique can measure line width distribution, end-line oozing, and stable line width based on image analysis algorithms, allowing rapid and automated extrudability assessment.

Data collected from quantitative extrudability assessments can be used to develop predictive models and estimate extrudability for new materials. To date, studies of variable interactions in 3D food printing rely on methods such as response surface methodology (RSM) to optimize the printing parameters. Severini et al. (2016) explored the effects of the printed layer height and infill percentage on the printability of wheat dough using RSM. Based on the RSM models, the study identified key printing parameters for printability and concluded that breaking strength (a measurement of printability) of the final product was related to the infill percentage of printing. These studies applied statistical models based on materials with similar compositions, which limits their validity and applicability over a broader range of materials and system parameters.

In non-food 3D printing, Elbadawi et al. (2020) applied machine learning algorithms to predict the printability of pharmaceutical tablet materials using a combination of rheological properties and printing parameters. This study collected the variables that were known to represent tablet rheology in pharmaceutical manufacturing and modelled the complex relationship between materials and printing parameters to predict the printability of unknown tableting materials. This hybrid modelling approach is known as "gray-box modelling", which combines mechanistic insight (white box models) and data-driven models (black box models) to maximize the predictability in manufacturing (Roupas, 2008). Specifically, variables derived from mechanistic studies are used as inputs for data-driven models to predict the parameter of interests. Gray-box models are especially useful to reduce the mechanistic model complexity and improve data-driven model interpretability. In 3D food printing, several physio-chemical phenomena happen simultaneously: non-Newtonian flow, heat transfer, and fusion (adhesion and confluence) of materials (Rando & Romaioli, 2021). Various printing parameters can further impact the printing results. To best model this complex process, gray-box models can combine data-driven model frameworks with the partial understanding of the physiochemical phenomena during food printing to predict material's extrudability. In addition, the use of generic material properties and printing system parameters may make the resulting models applicable to a wider range of materials and conditions.

In this study, we aim at developing predictive models to estimate the extrudability and line geometry prior to printing 3D food structures. Specifically, we applied image analysis to automatically measure the extrudability of food materials as determined by mode width, line height and width consistency of the printed filaments. An experimental dataset of 131 unique material-and-printing parameter combinations was collected from printing experiments. Regression and classification models were trained and tested to predict the extrudability using both the rheological properties of the materials and the printing parameters as inputs. This study thus demonstrates a gray-box modelling approach to automate data collections and predict parameters of interest in 3D food printing, which can control 3D printers with adaptivity to different materials and ensure robust and reliable operations.

3.2. Materials and methods

3.2.1. Printing Materials

Concentrated sodium caseinate dispersion (48%, w/w) was kindly supplied by FrieslandCampina (Wageningen, the Netherlands) and was kept at – 20 °C prior to the experiments. The sodium caseinate concentrate was thawed overnight at 4 °C, tempered to 80 °C for 10 min in a water bath, diluted with deionized water to a final concentration of 34%, and used as the low shear-thinning (LST) printing material for the printing experiment. Commercial food products with complex compositions were purchased from a local supermarket (Albert Heijn, the Netherlands) for printing experiments (Table 3.A1). Specifically, two brands of processed cheese slices (Cheddar, ERU, the Netherlands; Cheddar, Country Cow, the Netherlands) and 2 brands of cheese spreads (Goudkuipje Naturel, ERU, the Netherlands; Crème de Brie, Président, Lactalis, France) were used as medium shear-thinning (MST) printing materials. One chocolate spread (Speculoos Original, Lotus, the Netherlands) and one coconut butter spread (Creamy Original, Voilife, Greece) were used as high shear-thinning (HST) printing materials. All printing materials were stored at 4 °C and tempered at 18 °C before the subsequent experiments.

3.2.2. Shear Viscosity Measurement

Shear viscosity tests were performed using a rheometer equipped with a heating cap (Anton Paar Physica MCR502, Anton Paar GmbH, Graz, Austria). A 20-mm cone and plate geometry with a 2° angle was used. The printing materials were loaded on a preheated plate at different measuring temperatures between 27 to 50 °C. The specific measuring temperatures for shear viscosity match with the printing temperatures listed in Table 3.1. The top cone was brought down to leave a 0.085-mm gap, excessive material was carefully removed, and the rim of the sample was coated with high viscosity paraffin oil to prevent water evaporation during measurement. The shear rate was increased from 0.1 to 100 s^{-1} logarithmically in 250 s, and the corresponding viscosity was recorded at a fixed temperature between 27 to 50 °C. The power law equation (1) that describes the behavior of non-Newtonian fluids was fitted to the measured shear viscosity data.

$$\mu = K\dot{\gamma}^{n-1} \qquad (1)$$

where μ is the viscosity (Pa·s), K is the flow consistency coefficient (Pa·s^n), n represents the flow index (-), and $\dot{\gamma}$ is the shear rate (s^{-1}). For values $n < 1$, the fluid is considered shear-thinning.

3.2.3. 3D printing experiment

Extrusion-based 3D printing was carried out using an in-house developed printer which was modified from an air-pressured dispensing system (DR-2203, Nordson EFD, USA) (Schutyser et al., 2018). The printing materials were carefully loaded into a printing syringe, and the syringe was closed off with a pressure cap and tempered at printing temperatures between 27 and 50 °C for 10 min prior to printing in a temperature-controlled syringe holder with an electric heating element.

3.2.3.1. Flow rate measurement

The printing system performed a point extrusion for 10 s at various pressures and printing temperatures between 27 and 50 °C. The dispensed materials were weighed and converted to volume to determine the volumetric flow rates. At least 5 different pressures were used to dispense the printing materials in triplets. From preliminary data analysis, we found that a power-law equation best fitted the measured averaged volumetric flow rates and printing pressures, with the highest coefficient of determination (R^2). Therefore, equation 2 was used to determine the flow rate exponent (b) and flow rate coefficient (m).

$$Q = m\Delta P^b \quad (2)$$

where Q is the volumetric flow rate (mm^3 · s^{-1}), m is the flow rate coefficient (× 10^5 mm^3 · s^{-1} · Pa^{-1}), ΔP is the printing pressure (× 10^5 Pa), and b is a dimensionless flow rate exponent (-).

3.2.3.2. Line extrusion

The printing platform was controlled by the Visual PathBuilder software (V3.9.7.0, Ratioserv Software Engineering GmbH, Austria) to print 50-mm lines to assess the consistency in line extrusion. All lines were extruded at the same position on the platform relative to the extrusion nozzle's origin. We carried out a total of 131 unique combinations of materials and printing parameters in duplicates by varying printing temperatures, printing pressures, and nozzle speeds. The nozzle size and height (i.e. distance between the nozzle tip and the

printing platform) were kept constant for all lines at 1 mm. Detailed printing parameter ranges are shown in Table 3.1.

Table 3.1. An overview of printing parameter range used to assess line extrudability

Parameters	Range
Printing Pressure (×105 Pa)	[0.38 – 4.74]
Nozzle Speed (mm ·s-1)	[5 – 45]
Nozzle Size (mm)	1
Temperature (°C)	[27, 40, 45, 50]
Nozzle Height (mm)	1
Printing Length (mm)	50

3.2.4. Extrudability assessment

3.2.4.1. Camera set up and image collection

A top-view camera (A6000, SONY, Japan) equipped with a macro lens (focal length = 35mm, SEL1760Z, SONY, Japan) was mounted 40 cm above the dispensing platform. A black Teflon sheet was placed as the background to maximize contrast. A white tape with known width (24 mm) was used as a scaling object, and pictures (2000 × 3000 pixels) were taken within 10 s after the line extrusion (Figure 3.1A).

3.2.4.2. Image analysis preprocessing

The raw images of line extrusion were first smoothed by the Gaussian blur algorithm for denoising purposes. The smoothed images were set to gray scale using the Luma formula: 0.299R + 0.587G + 0.114B (Fahmy et al., 2020). We then marked the pixel positions of the extruded line as the area of interest and performed the Canny Edge Detection algorithm to extract the boundary of the extruded line as a binary image (Canny, 1986) (Figure 3.1B).

3.2.4.3. Line length, width, and height measurement

The line length was measured as the maximal length on the longitudinal axis of the extruded line. The line width was calculated as the maximal length on the transversal axis and was expressed as a distribution of width measured on a per-pixel basis along the longitudinal axis. The mode of the width distribution was used as the stable width of the extruded line. The width consistency index was calculated as a proportion of the width distribution measured within ± 5% of the mode line width (Figure 3.1C). The line height cannot be directly measured from the top-view camera setup, and therefore it was estimated by

approximating the cross-sectional area of the extruded line as flattened tube consisting of a rectangle with 2 semi-circular edges (eq. 3 and Figure 3.1D) (Greeff & Schilling, 2017):

$$H = \frac{\sqrt{4w^2 - 16A + 4\pi A} - 2w}{\pi - 4}; \quad A = \frac{QL_0}{Lv} \qquad (3)$$

H is the line height (mm), *w* is the measured mode line width (mm), A is the calculated cross-sectional area. Q is the volumetric flow rate ($mm^3 \cdot s^{-1}$), L_0 is the target line length of 50 mm, L is the measured line length (mm), and *v* is the printing speed ($mm \cdot s^{-1}$). The image analysis workflow is outlined in Figure 3.1 to highlight raw picture acquisition, preprocessed picture and quantitative measurements.

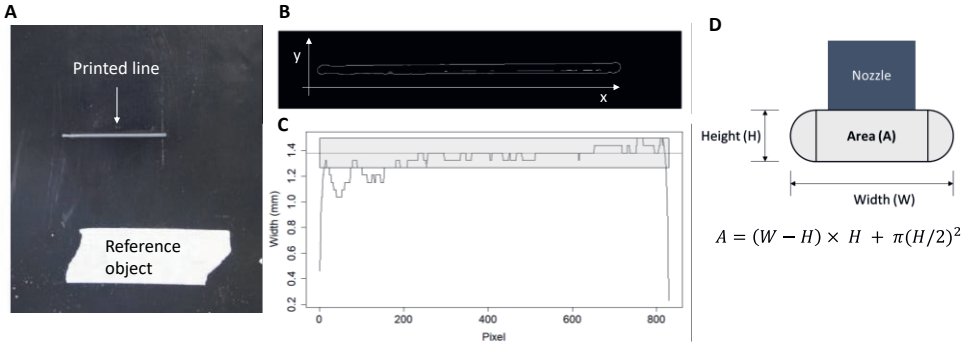

Figure 3.1. A: Original image obtained from the top-view camera. B: Extruded line boundary extracted from the Canny edge detection algorithm. C: Length, mode width, width consistency, and width distribution measured from the extruded line. The gray box represents the ± 5% variation of the mode width. D: Schematic representation of cross-sectional area of line filament (modified from Greeff & Schilling, 2017).

3.2.5. Predictive modelling of extrudability

3.2.5.1. Categorical evaluation of extrudability

Using continuous assessment of the extrudability from image analysis, we categorized the acceptability of the extrusion based on thresholds referenced from a common 3D printing "Slic3r" software's manual (Hodgson, 2021). The binary classification can simplify the decision-making for assessing the acceptability of line extrusions. The classification models can be further trained to directly predict the extrudability with simple outputs for material screening purposes. Based on the measured line length, mode width, line height, and width consistency, we created binary labels to categorize acceptable and unacceptable line

filaments based on each measurement. A mode width less than 1.7 times of the nozzle size was considered as an acceptable extrusion width. Acceptable extrusion height was calculated based on a similar approach. A threshold of between 0.6 to 0.8 times the nozzle size was set to determine acceptable and unacceptable extrusion heights. For width consistency, we set the consistent width to be > 80%, with the inconsistent widths being < 80%. Table 3.2 provides an overview of classification criteria and the number of data points per class. The binary labels were subsequently used to train and test classification models to predict extrudability.

Table 3.2. Line filament extrudability parameters classification, number of samples per class, and classification thresholds

Measurement	Acceptable (0)	Unacceptable (1)	Classification Thresholds
Mode Width (W)	67	64	$C_W = \begin{cases} 0 & if \quad \frac{W}{D} < 1.7 \\ 1 & if \quad \frac{W}{D} > 1.7 \end{cases}$
Line Height (H)	53	78	$C_H = \begin{cases} 0 & if \quad 0.6 < \frac{H}{D} < 0.8 \\ 1 & if \frac{H}{D} < 0.6 \quad or \frac{H}{D} > 0.8 \end{cases}$
Width Consistency (WC)	98	33	$C_{WC} = \begin{cases} 0 & if\ WC > 80\% \\ 1 & if\ WC < 80\% \end{cases}$

where C is the binary class, H is the line height, and D represents the nozzle size. For classifications, 0 represents acceptable extrusion and 1 represents unacceptable extrusion.

3.2.5.2. Model training and testing

The extrudability dataset was randomly divided to assign 70% of the data for model training and 30% for model testing. Regression models were trained using the flow index (n), consistency coefficient (K), flow rate exponent (b), flow rate coefficient (m), printing pressure, and nozzle speed as inputs to predict the mode width, line height, and width consistency. During our preliminary modelling attempts, *random forest* was the most accurate prediction algorithm compared to other regression models. The random forest algorithm operates as an ensemble of decision trees (Breiman, 2001). A subset of input variables is selected for developing a decision tree to estimate the output value. This process is repeated multiple times, and the final prediction output is determined by the mode of the output distribution. In our study, the predictive models were 10-fold cross-validated, and

optimal hyperparameters of the random forest algorithm (minimal note size, number of variables for splitting, and splitting rules) were determined based on the smallest root mean square error (RMSE).

Classification models were trained using the same inputs to predict acceptable and unacceptable extrusion based on mode width, line height, and width consistency (Table 3.2). The random forest models were cross-validated to select the optimal hyperparameters based on the highest classification accuracy. The variable importance was calculated for the optimized models based on the improvement of out-of-bag accuracy (OOB-accuracy) for each variable (Breiman, 2001). The variable importance can identify key factors that determines the line extrudability in 3D food printing.

The cross-validated regression and classification models were then validated using testing samples from the extrudability dataset. The testing RMSE and prediction accuracy were calculated and served as the final evaluation of the predictive models. Additionally, for regression models, the ratio of prediction to deviation (RPD) was calculated by dividing the RMSE by the standard deviation of the dataset to estimate the predictability level. A RPD value above 2 represents a moderate model predictability and above 3.5 represents a good model predictability (Williams, 2001). For classification models, the kappa reliability value was calculated to compare the model accuracy to random chance. A kappa value between 0.6 and 0.79 implies a moderate level of agreement and above 0.8 implies a good level of agreement. (McHugh, 2012).

3.2.6. Software packages and data availability

Image analysis and predictive modelling were achieved using an in-house program developed in the R programming language with the Tidyverse, imager, caret, and ranger packages (Barthelmé & Tschumperlé, 2019; Kuhn, 2008; Wickham et al., 2019; Wright & Ziegler, 2015). The extrudability dataset and the R codes in this study are available at https://git.wur.nl/yizhou.ma/food-extrudability-assessment-and-prediction.

3.3. Results & Discussion

3.3.1. Shear viscosity of printing materials

Shear thinning has been suggested as a desirable property for smooth extrusion in 3D food printing as it reduces the pressure needed for printing while stabilizing the geometry after extrusion (Liu et al., 2019). The shear viscosities of the printing materials measured at printing temperatures were fitted to the power-law viscosity model (eq.1) to derive the flow index (n) and consistency coefficient (K). All fits had coefficients of determination (R^2) greater than 0.98, indicating strong agreement between data and model. All printing materials used in this study were shear thinning ($n < 1$, Table 3.3). Based on food formulations and measuring temperatures, we obtained food materials that exhibit low ($n > 0.8$), medium ($0.2 < n < 0.8$), and strong ($n < 0.2$) shear thinning. In Table 3.3, the n and K values of processed cheese (MST-3 and 4) and sodium caseinate dispersion (LST-1) depended both on the temperature, which agrees with previous rheological studies of processed cheese and sodium caseinate (Lee et al., 2004; Zhang et al., 2020). Due to the temperature dependency of the shear viscosity, the printing temperature can be adapted to modify the shear thinning of printing materials for optimal food extrudability. Schutyser et al. (2018) suggested that increasing printing temperature results in softening of a sodium caseinate dispersion and in a reduction of its viscosity. After extrusion, the sodium caseinate cools to room temperature with a concomitant steep increase of viscosity to achieve a self-supporting printed structure. We also observed that differences in the compositions of the commercial food products lead to differences in shear thinning (Table 3.3). Since we used commercial food products in this study, the detailed formulations and manufacturing steps are unknown to us. However, the rheological properties of these semi-solid commercial food products are probably dominated by a limited number of functional ingredients and their interactions with other ingredients (Kim et al., 2018). As shown in Table 3.A1 various emulsifiers, melting salts, and gums are present in the printing materials, and these ingredients impact shear thinning of semi-solid food systems. Therefore, variations in product composition and temperature are probably reflected in the large range of shear thinning behavior in Table 3.3. Because this study focuses on modelling food extrudability based on shear-thinning behaviors, we used the n and K values as rheological variables in the subsequent predictive modelling steps.

Table 3.3. Consistency coefficients (K), the flow indices (n), flow rate exponents (b), and flow rate coefficients (m) of high-shear-thinning (HST), mid-shear-thinning (MST), and low-shear-thinning (LST) printing materials (Power law fits: $R^2 > 0.98$).

Material	Temperature (°C)	Viscosity power-law Equation		Flow rate power-law Equation	
		n	K (Pa·s)	b	m ($\times 10^5$ $mm^3 \cdot s^{-1} \cdot Pa^{-1}$)
HST-1	27	0.16	232	5.8	133
HST-2	27	0.18	158	4.1	313
MST-1	27	0.44	99.2	2.6	70.4
MST-2	27	0.46	92.0	2.7	114
MST-3	50	0.51	421	2.2	8.56
MST-3	45	0.53	258	2.3	8.63
MST-4	45	0.54	580	2.1	4.10
MST-4	40	0.56	383	2.4	4.36
LST-1	50	0.87	402	1.3	2.65
LST-1	45	0.95	929	1.1	1.05

3.3.2. Flow rate measurement

Next to the power-law fits of the rheological measurements, Table 3.3 also shows the power-law-fits of the flow rate measurements; also with R^2 greater than 0.98, indicating good model fitness. The flow rate exponents (b) of the printing materials are greater than 1, representing an exponential increase of the flow rate as a result of an in increase in the pressure difference. The flow rate coefficient (m) is a power-law fitted estimation of the flow rate ($mm^3 \cdot s^{-1}$) under 1×10^5 Pa of pressure (i.e. 1 bar). The m value varied from 1.05×10^5 to 3.14×10^7 $mm^3 \cdot s^{-1} \cdot Pa^{-1}$ indicating the large range of shear thinning properties of the printing materials. As shown in Figure 3.2, an inverse near-linear relationship is observed between the n and b values among high, medium, and low shear-thinning materials. This inverse relationship between n and b values indicates that the dependency of the flow rate on the printing pressure can be used for estimating of both n and b. The process of pushing materials through the printing nozzle is similar to the measurement process of a capillary rheometer described by Steffe (1996). In a capillary rheometer, a pressure difference is generated in a tube, and corresponding volumetric flow rate and pressure drop can be used to characterize various rheological properties of fluids and semi-solids. For power-law fluids, the shear rate in a capillary rheometer can be determined by the Rabinowitsch-Mooney equation (4), where Q is the volumetric flow rate, n is the flow index for power-law fluids, and τ is the shear stress that can be calculated from the radius (R) and

length (L) of the capillary and the pressure difference (ΔP) applied to the capillary (equation 5) (Steffe, 1996).

$$\frac{d\ln(Q)}{d\ln(\tau)} = \frac{1}{n} \quad (4)$$

$$\tau = \frac{R\Delta P}{2L} \quad (5)$$

The inverse relation shown in Figure 3.2 can be used to find the value for b. The Rabinowitsch-Mooney equation provides theoretical support that the b values obtained from this study can be used as a rheological feature to describe the shear thinning behavior. However, the flow rate coefficient m is determined by both the K and n values of the printing material and the printing nozzle geometry. Schutyser et al. (2018) applied a modified Poiseuille equation for power-law fluids to study printing pressure's impact on printability of sodium caseinate, and found a satisfactory model fit for n but not for K because it was influenced by wall slippage. In this study, we tested the empirically derived b and m values as potential substitutes for n and K values measured from traditional shear viscosity measured by a rheometer. Because the n and K values are measured within the printing system, they will include the wall effects and minimize geometric effects, which are both relevant for the operation of the printer. These shear-thinning features were further used for predictive model development to evaluate their predictability of food extrudability in 3D printing.

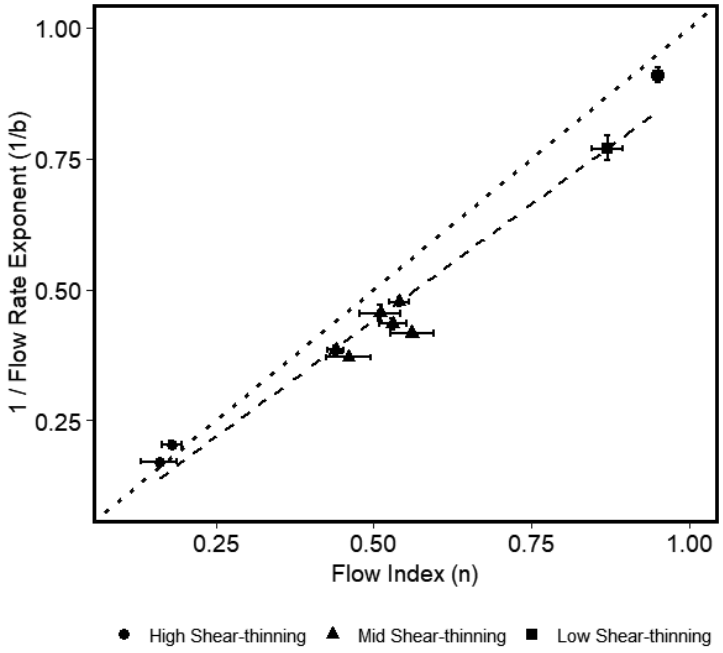

Figure 3.2. Flow index (n) vs. flow rate exponent (b) of high-shear-thinning (HST), mid-shear-thinning (MST), and low-shear-thinning (LST) printing materials. The error bars represent standard deviations from duplicate measurements. The dashed line represents the least-square fit of between the flow index and flow rate exponent ($R^2 = 0.96$). The dotted line represents the n = 1/b reference line.

3.3.3. Extrudability assessment

We used 131 unique combinations of materials and printing parameters to obtain a large range of line extrudability measurements. Figure 3.3 shows the distributions of occurrence of the mode width, line height, and width consistency measured by our image analysis technique. The mode width of the printed lines ranged between 0.97 to 3.48 mm. The nozzle size used for printing was kept at 1 mm, and a mode width larger than that was observed for almost all of the samples printed in this study. Expansion of the line width after extrusion, or "die-swell", is commonly reported in other 3D food printing studies, and generally thought to be caused by elastic (retardation) effects. A 30 to 60% increase of line width in comparison with the nozzle size was found during printing of starch and gelatin alginate hydrogels (Alruwaili et al., 2019; J. Chen et al., 2019). This expansion of the line width is also common in thermoplastic printing. An increase of printing pressure and flow rate have been associated to the die-swell phenomenon due to the retardation of polymer chains that became elongated during extrusion (Le-Bail et al., 2020). According to the common 3D

printing slicer software (Slic3r), up to 70% of line width expansion is considered acceptable when generating printing path from digital designs (Hodgson, 2021). When 3D printing the first layer, excessive pressure may be used to achieve an up to 200% wider line width to ensure adequate bonding of the material to the printing platform in the Slic3r program. Due to the rheological differences among food printing materials, a large range of line width and material properties should be considered when building a predictive model. The large range of line widths used in this study allows robust model training for the subsequent line width predictions.

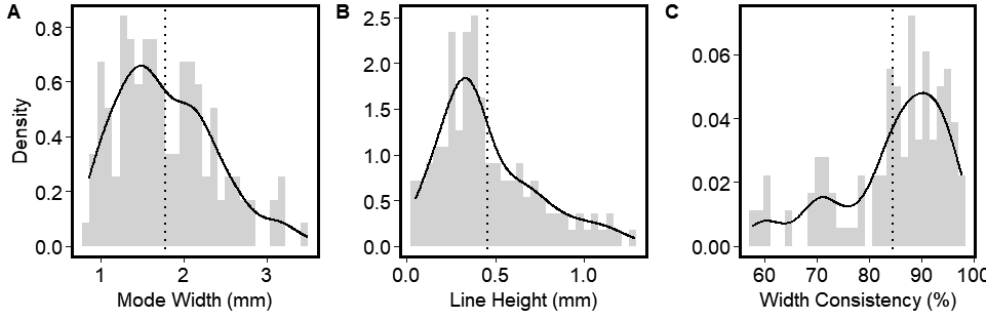

Figure 3.3. Distributions of mode width (A), line height (B), and width consistency (C) obtained from the extrudability assessment (n = 131). The gray bars represent the histogram, the dotted lines represent means, and the solid curves represent smoothed probability distributions of mode width, line height, and width consistency, respectively.

Because of the width expansion of the lines, the calculated line height was generally smaller than the nozzle size (Figure 3.3B). The increase of line width and the decrease of line height were likely attributed to the post-extrusion recovery of the printing materials, as proposed by Liu et al. (2019). After extrusion, food materials can experience a slow recovery of the viscosity from shear stress and heat, which may lead to further geometric expansion. While the die swells and viscosity recovery were not measured for each material, we assumed that all printed materials experienced geometric expansion, and the predictive models were trained to fit the final line filament geometry for the estimation of the extrudability. The recovery process is considered in slic3r programming. According to the developers, one can expect the line height to be ranged between 60 to 80% of the nozzle size. In our study, 53 out of the 131 lines were within the acceptable height range (Table 3.2).

Furthermore, Figure 3.3C showed a left-skewed distribution of the width consistency, indicating that most of the lines were extruded consistently. The width consistency represents the length fraction of the printed line with ± 5% width variation from the mode width. Extreme cases of inconsistent line printing can result in broken lines and rough surfaces (Liu et al., 2019). Fahmy et al. (2020) quantified oozing effects and initial extrusion delay, which both can lead to inconsistent line extrusion. Inconsistent line width is generally undesirable for printing because it may lead to poor retention of the shape when layering 3D structures (Paxton et al., 2017). Most of the existing studies conducted qualitative assessment of the width consistency, and no commonly-accepted qualitative method is available. Therefore, we could only establish an arbitrary threshold (80%) to classify acceptable and unacceptable categories for building classification models (Table 3.2). Further studies need to quantitatively evaluate the impact of the width consistency on 3D printability to select a consistency threshold for more generalizable and even better actionable predictions. Consistency data obtained from our study can be easily retrained based on any new thresholds established later.

3.3.4. Extrudability influenced by printing parameters

Prior to building multivariate predictive models, we separately examined the univariate relation of the printing pressure and nozzle speed with the extrudability. Figure 3.4A shows the mode width change as an exponential function of the printing pressure for high, medium, and low shear-thinning materials extruded under constant nozzle speed over the platform. The material with high shear thinning showed the strongest exponential increase of the mode width, which is consistent with the n and b relationship discussed in Section 3.2. Under constant nozzle speed, printing materials that exhibit stronger shear thinning generally required a smaller printing pressure, while a slight change in printing pressure led to large mode width differences and inaccurate printing (i.e. over-extrusion). Therefore, accurately extruding materials that exhibit strong shear thinning, requires more precise control over the printing pressure.

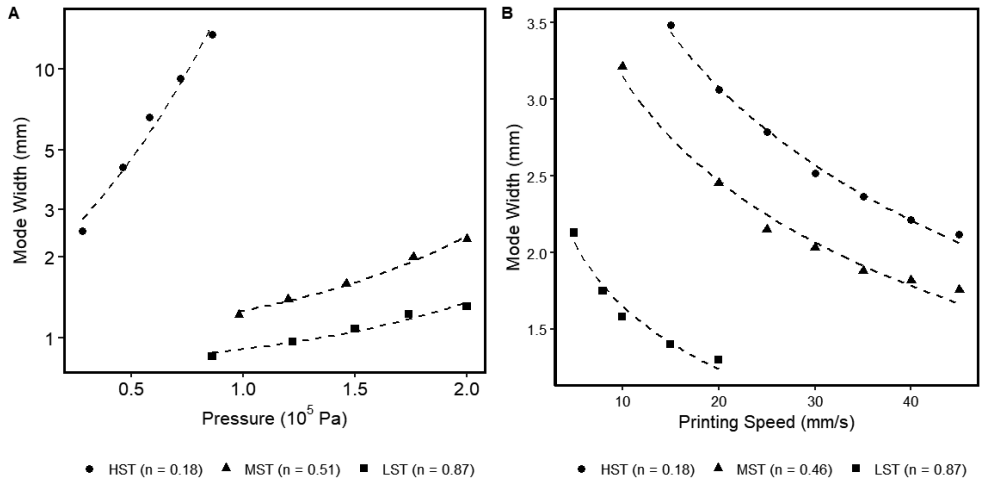

Figure 3.4. A: Pressure vs. mode width at constant printing speed (15 mm · s-1) and B: printing speed vs. mode width at constant pressure (0.58 × 105 Pa) for high-shear-thinning (HST), mid-shear-thinning (MST), and low-shear-thinning (LST) printing materials based on flow index (n) measurements. The dashed lines represent the least squared exponential (A) and natural logged (B) fits. Note that the mode width data for HST material higher than 4 mm were shown to illustrate the pressure and mode width relationship but excluded for predictive model development

Moreover, Figure 3.4B shows the effects of the nozzle speed on the mode width under constant printing pressure. An inverse natural log fit was observed between the nozzle speed and the mode width, which is consistent with a previous study from He et al. (2016). Lower nozzle speeds lead to a rapid increase of the mode width because too much material gets extruded at each line position. In contrast, an increase of nozzle speed led to a stretch of the line and thus reduced the line width. He et al. (2016) suggested that a relatively consistent line width can be printed within a range of nozzle speeds (i.e. within the stability zone). Exceeding the upper range of the zone may lead to width inconsistency and broken lines, whereas printing below the lower range of the stability zone may result in swift and uncontrolled increase of the line width. The univariate impacts of the printing pressure and the nozzle speed may provide helpful insights to fine-tune the printing parameters after reaching the general range of printing settings and material properties, using a multivariate model.

3.3.5. Prediction of extrudability

3.3.5.1. Regression predictions

The multivariate predictive models were built with the printing variables and 3 sets of rheological variables: (1) n and K only, (2) b and m only, and (3) n, k, b, and m combined. For regression models, the best hyperparameters were selected based on the model training, and the testing results reflect the final evaluation of the model performance (Table 3.4).

For mode width prediction, the model was able to predict the line width with a range of RMSE between 0.25 and 0.27 mm. The R^2 around 0.80 and RPD greater than 2 showed moderate regression predictability of the mode width. The regression model results for the line height showed good predictability with the RMSE around 0.070 mm, R^2 ranged from 0.93 to 0.94, and RPD greater than 3.5. The better predictability of the line height is likely caused by the line height calculations. The flow rate and printing pressure were a part of the height calculation, and they are closely related to the b and m values that are used as model inputs. Lastly, the testing model results showed a moderate predictability for the width consistency with a RMSE between 4.7 and 5.4%, R^2 ranged from 0.73 to 0.81, and RPD greater close to 2.

Table 3.4: Training and testing results of random forest regression predictions of mode width, line height, and width consistency of printing materials based on printing parameters and rheological properties

Parameter	Inputs[1]		Training			Testing		
	Printing parameters	Rheological properties	mtry[2]	RMSE[3]	R^2 [4]	RMSE	R^2	RPD[5]
Mode Width (mm)	P, v	n, K, b, m	6	0.26	0.81	0.27	0.83	2.3
		b, m	4	0.30	0.76	0.25	0.78	2.1
		n, K	4	0.28	0.79	0.26	0.79	2.1
Line Height (mm)		n, K, b, m	6	0.086	0.93	0.074	0.93	3.7
		b, m	4	0.096	0.92	0.062	0.94	4.1
		n, K	4	0.076	0.94	0.071	0.94	3.9
Width Consistency (%)		n, K, b, m	5	5.3	0.71	5.4	0.73	1.9
		b, m	3	6.1	0.63	4.7	0.81	2.3
		n, K	2	5.7	0.69	5.6	0.71	1.9

[1]input variables: P: printing pressure, v: nozzle speed, n: flow index, K: consistency coefficient, b: flow rate exponent, m: flow rate coefficient. [2]mtry = number of variable for splitting; [3]RMSE = root mean square error; [4]R^2 = coefficient of determination, [5]RPD = ratio of prediction to deviation.

Possible errors of extrudability predictions may come from variation in the post-extrusion viscosity recovery among printing materials (see Section 3.3; Liu et al., 2019). Further studies may focus on extracting meaningful features to characterize die swells and viscosity recovery

from shear stress and heat to better account for this variation. Including the dynamic post-extrusion recovery stage for each printing material may provide some improvement to the present extrudability model performance.

The moderate to high extrudability predictions suggest that models developed in this study can serve as the initial step to estimate the line extrudability of complex food formulations based on a rapid determination of the shear thinning behavior. For all three predictions, we observe minor predictability differences between including and excluding the n and K values as model inputs. The predictabilities were similar between using b and m or n and K as rheological variables in models. The prediction results based on b and m as rheological inputs are visualized in Figure 3.5. Therefore, the prediction results further confirm that using b and m values derived from flow rate measurements can sufficiently characterize material's shear-thinning behaviors for extrudability predictions. Our results imply that a simple printer test with a new printing material may provide printing parameter adaptations to ensure proper extrudability.

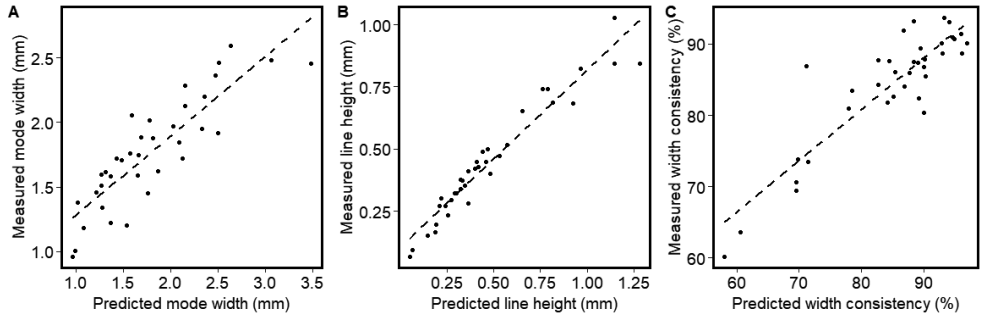

Figure 3.5. Predicted vs. measured mode width (A), line height (B), and width consistency (C) of the testing sets using printing pressure, nozzle speed, flow rate exponent (b), and flow rate coefficient as inputs. The dashed line represents the least-square linear fit between predicted and measured values.

3.3.5.2. Classification predictions and variable importance

To directly estimate the acceptability of line extrusion, we further simplified the prediction outputs by using the classification models to predict acceptable and unacceptable line filaments. Table 3.5 shows the classification results for acceptable line extrudability. We calculated the classification accuracy and kappa value to evaluate the final prediction results. According to McHugh (2012), the kappa value compares the prediction accuracy to the

accuracy from random chance, and a kappa value between 0.6 and 0.79 shows a moderate level of agreement. For the classification models developed in this study, the prediction accuracy ranged from 76.9 to 92.1% and the kappa value ranged from 0.54 to 0.75, indicating indeed moderate classification reliability of the models. The simple prediction outputs (acceptable vs unacceptable) can provide quick screening of food printing materials for 3D printing purposes, again using the printer itself instead of a professional rheometer.

Table 3.5: Training and testing of random forest classification predictions of mode width, line height, and width consistency of printing materials based on printing parameters and rheological properties

Parameters	Inputs		Training			Testing	
	Printing parameters	Rheological properties	mtry[2]	Accuracy	Kappa	Accuracy	Kappa
Mode Width (mm)	P, v	n, K, b, m	3	84.2%	0.65	84.6%	0.69
		b, m	4	78.5%	0.54	87.2%	0.69
		n, K	3	88.6%	0.77	76.9%	0.54
Line Height (mm)		n, K, b, m	6	82.9%	0.54	81.6%	0.54
		b, m	4	80.6%	0.46	84.6%	0.62
		n, K	4	85.3%	0.67	82.1%	0.63
Width Consistency (%)		n, K, b, m	2	91.5%	0.74	89.5%	0.71
		b, m	3	92.9%	0.79	89.5%	0.66
		n, K	3	90.2%	0.70	92.1%	0.75

[1]input variables: P: printing pressure, v: nozzle speed, n: flow index, K: consistency coefficient, b: flow rate exponent, m: flow rate coefficient. [2]mtry = number of variable for splitting.

The accuracy improvement was calculated and shown in Figure 3.6 to examine the importance of the variables for the classification predictions. Similar variable importance was observed from the regression analysis (data not shown). Printing pressure and nozzle speed show similar importance to mode width, line height, and width consistency predictions. The highly variable importance of the printing pressure and nozzle speed was also reflected in the univariate evaluation in Section 3.4. When including n and K as predictors, the variable importance of b and m were slightly less than for n and K. When excluding n and K in the model, b and m became more important. Based on Table 3.5, including n and K values as predictors had negligible impact on model performance. This is likely caused by the strong correlation between n and b (Figure 3.2), and the complex relationship between K and m (Section 3.3.2). The overall accuracy improvement was diluted when including the correlated variables. The variable importance calculations

confirmed results from previous studies that shear-thinning properties, printing pressure, and nozzle speed can determine extrudability and filament formation of 3D food printing.

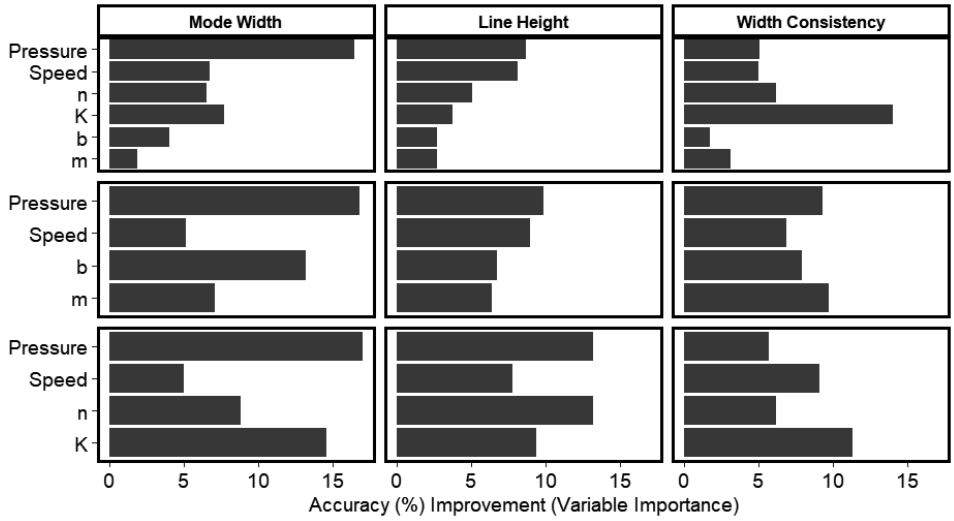

Figure 3.6. Out-of-bag classification accuracy improvement (variable importance) of mode width, line height, and width consistency predictions from models based on printing pressure, nozzle speed, flow index (n), consistency coefficient (K), flow rate exponent (b), and flow rate coefficient (m).

3.3.5.3. Extrudability prediction discussions

This study showcases a predictive workflow to predict the extrudability of food materials prior to printing 3D structures, using measurements that can be generated by the 3D printer itself. Printer-generated measurements would allow quick and automated printing parameter adjustments when printing materials with various rheological properties. The quick adjustments can potentially enhance the ease and robustness of extrusion-based 3D food printing of complex foods.

This predictive workflow uses rapid and automated data collection to predict the extrudability based on image analysis. The high-throughput, scalable, and reproducible data collection method here generated structured data for the subsequent predictive work. By deriving generic rheometric parameters from raw viscosity measurements, the gray-box model can extend its applicability to materials that have similar rheological characteristics rather than with similar compositions. The developed model in this study can be reproduced by others using the publicly available data and open-source codes (Section 2.6). Future

applications can also include more extrudability data of other food materials to further enhance the model's predictability using the existing framework.

The complex relationship among rheological properties, printing parameters, and extrudability was modelled by the random forest algorithm with moderate to high predictability. Following this workflow, future research can develop similar data-driven applications in 3D food printing and other food processing fields to optimize unit operations and improve production efficiency, reliability and robustness towards changes in material quality.

3.4. Conclusions

Extrudability as a critical initial step to successful 3D food printing was quantified using automated image analysis and predicted by data-driven models using generic rheological parameters as input, instead of raw data, which makes the models more widely applicable. The flow rate exponent (b) and coefficient (m) can be derived from a power-law equation that described the relation between volumetric flow rate and printing pressure. The b and m values can be used to characterize the shear-thinning behavior of complex food materials. Using as input variables b, m, printing pressure and speed, we successfully predicted the extrudability of complex food systems with moderate to high accuracy.

The "gray-box", data-driven framework presented in this study can be extended to assess 3D structures of printed food materials and predict the success of 3D printing by including indicators of rheological properties (e.g. zero-shear viscosity and yield stress) and printing parameters. The current printing experimental dataset can be further expanded to include the material relaxation dynamics after the extrusion. With larger sample size and meaningful features, robust predictive models of extrudability can help limit trial-and-error procedures when developing new food formulations for printing and optimizing printing parameters for new food materials. In addition, it can be used for in-service adaptation of the printer parameters to the properties of a new printing material.

Other aspects of printability such as adhesion and fusion of materials, shape fidelity and retention over time should also be considered when formulating food materials for 3D printing. Further studies may need to develop standardized methods to characterize

printability and fidelity of 3D printed foods and include these aspects as prediction targets to holistically ensure successful printing and expand practical utility of 3D food printing.

3.5. Appendix

Table A1. Ingredient lists and purchase dates of commercial food product used in this study

`	Purchase Date	Ingredients	Coded Names
Violife Creamy original	October, 2020	Water, coconut oil (23%), starch, sea salt, acidity regulator: glucono-delta-lactone, flavors, olive extract, vitamin b12.	HST-1
Lotus Speculoos Original	December, 2020	Original speculoos 58% (wheat flour, sugar, vegetable oils (sustainable and certified palm oil, rapeseed oil), candy syrup, raising agent (sodium hydrogen carbonate), soy flour, salt, cinnamon), rapeseed oil, sugar, emulsifier (soy lecithin), food acid (citric acid).	HST-2
ERU Goudkuipje	October, 2020	Cheese (milk), water, butter (milk), milk proteins, whey powder (milk), melting salts (e452, e339, e451), salt.	MST-1
Président Crème de Brie	December, 2020	Brie president (55%) (milk), reconstituted skimmed milk, butter (milk), milk proteins, melting salts (e339, e452), preservatives: potassium sorbate, thickeners: xanthan gum, carob flour.	MST-2
Country Cow Cheese Slices	October, 2020	Cheese (48%) (of which 50% cheddar), skimmed milk, butter, skimmed milk powder, melting salts (e452, e339), salt, citric acid e330, coloring (paprika extract e160c).	MST-3
ERU Slices Cheddar	December, 2020	55% cheese (of which 50% cheddar), water, milk proteins, whey powder, butter, melting salts (e452), salt, coloring (paprika extract).	MST-4

Chapter 4 Improving 3D food printing performance using computer vision and feedforward nozzle motion control

This chapter has been published as: Ma, Y., Potappel, J., Chauhan, A., Schutyser, M. A. I., Boom, R. M., & Zhang, L. (2023). Improving 3D food printing performance using computer vision and feedforward nozzle motion control. Journal of Food Engineering, 339, 111277.

Chapter 4

Abstract

3D food printing is an emerging technology to customize food designs and produce personalized foods. Food printing materials are diverse in rheological properties, which makes reliable extrusion-based 3D printing with constant printing parameters a challenge. Food printing often suffers from improper extrusion because of the varying elasticity of the food materials. In this study, a computer vision (CV)-based method is developed to measure the instant extrusion rate and width under constant extrusion pressure/force. The measured extrusion rate and extruded filament width were used to conduct a feedforward control of nozzle motion for a pneumatic 3D food printer. As a result, the CV-based control method improves extrusion line accuracy to 97.6 to 100% and prevents under-extrusion of white chocolate spread, cookie dough, and processed cheese. The method can also be used to customize filament width with less than 8% of deviation from the target. With a simple measurement setup and a user-friendly software interface, this CV-based method is deployable to most food printing applications to reduce trial-and-error experiments when printing a new food material.

4.1. Introduction

Extrusion-based 3D printing is the most common technique for food printing. It relies on deposition of a viscoelastic food material through a nozzle to build 3D food structures layer by layer. Food materials such as chocolate, cookie dough, protein dispersions, and hydrocolloid gels have been successfully printed into customized shapes that may tailor to specific consumer preferences (Hao et al., 2010; Y. Liu et al., 2019; Montoya et al., 2021; Sun et al., 2020). The flavor and texture of 3D printed foods can be customized by changing the spatial distribution of flavorings and controlling the geometric designs (Zhu et al., 2021, 2020), offering an advantage over mass produced foods (Derossi et al., 2021). More recently, 4D food printing applications were developed to create dynamic changes of color, shape, and flavor of 3D printed foods (Teng et al., 2021). Over the last 14 years, food researchers have gained insights about food material printability, printing material formulations, and printing parameter optimizations, with the aim to produce personalized foods in the future (Derossi et al., 2021).

3D printing of chocolate has already been successfully applied in food manufacturing due to chocolate's popularity among consumers and the development of specialized chocolate printers to ensure high product quality. The commercial chocolate printers can print manufacturer-optimized "chocolate inks" with a set of pre-determined settings provided by the manufacturer. However, unlike chocolate, other food materials do not have customized printers to streamline the printing process for high-quality printed foods. Currently, extrusion-based food printers are mostly modified units of fused deposition modeling printers and pneumatic bioprinters (Wegrzyn et al., 2012). Extensive trial-and-error experiments are still needed to determine the proper printing parameters for a given food material due to the large variations in the viscoelastic properties of food materials (Siacor et al., 2021).

One of the common defects in extrusion-based 3D food printing is under- or over-extrusion of filaments due to improper extrudability and the creation of a "die swell" (i.e. expanded extruded filament width) by food materials (Fahmy et al., 2020a). The extrudability and die swell of food materials are governed by various factors. Specifically, the extrusion temperature, pressure, nozzle geometry, and material properties have been identified as factors to determine the extrudability of food materials with complex formulations (Ma et

al., 2021). Over-extrusion is specifically related to die-swell of polymeric food materials due to stress relaxation and is influenced by the printing pressure and the length of the printing nozzle (Le-Bail et al., 2020). To compensate for under- and over-extrusion during food printing, the nozzle motion should synchronize with the filament's instant extrusion rate (Wu et al., 2021). Therefore, determining the instant extrusion rate and extruded filament width of food materials may allow the optimization of the nozzle motion parameters to reduce the 3D food printing defects. The determination of instant extrusion rate (i.e. flow rate profile) and filament width could be achieved by either computer simulation or experimental measurement.

Computational fluid dynamic (CFD) modelling has been applied to predict the extrusion rate and optimize the printing processes for plastics (Moretti et al., 2021; Serdeczny et al., 2020b; Xia et al., 2018). The pressure drop and heat transfer models were resolved using rheological and thermal properties of the plastic materials. This approach can predict the extrusion flow and material solidification in a fixed extruder design (Xia et al., 2018). CFD modelling was subsequently applied to optimize the nozzle motion, improve printing accuracies, and design more efficient extruders in thermoplastic printing applications (Comminal et al., 2019; Ertay et al., 2018). However, simulating extrusion flow is computationally resourceful and requires extensive quantification of the material's physical properties. Therefore, the CFD modelling approach is best suited to provide fundamental understanding of the printing process and optimize printer designs for materials that are well understood and characterized (Go et al., 2017). In food printing, CFD modelling has not yet been widely applied due to the variations of the physical properties of foods leading to tedious simulation development and limited predictability because of the changing material properties. One study attempted to simulate the distributions of velocity, shear rate and pressure of food materials inside of a printing syringe using material rheological properties and syringe geometry (Q. Liu et al., 2020). It highlighted the dynamics of the material extrusion process but did not provide an applicable control strategy. A different study simulated the velocity distribution in a food printing nozzle using the continuity equations of volume transfer, assuming a constant extrusion rate and incompressibility of the food materials (Guo et al., 2020). This estimation could therefore only provide indications of the performance at steady state but cannot be used to minimize dynamic under- and over-extrusion.

An alternative to computer simulation is in-situ measurement. To determine the instant extrusion rate of plastic materials, optical methods based on computer vision (CV) have been used. The Lucas-Kanade optical flow algorithm was applied in several studies to determine the extrusion rates of plastic filament (Greeff and Schilling, 2017; Moretti et al., 2021). A close-up camera can film the filament extruding from the nozzle, and the optical flow analysis tracks the pixel intensity changes on the filament, identifies the filament's movement, and calculate its instant velocity. This approach has provided experimental support for numerical simulations and allowed closed-loop controls of 3D plastic printing to prevent filament slippage (Greeff and Schilling, 2017). Using a similar optical method, a different study developed an extruded filament width measurement tool based on computer vision (Tian et al., 2021). It used the instant extruded filament width to correct for printing inconsistencies during extrusion printing of polydimethyl siloxane (PDMS). Currently, the extrusion flow rate and extruded filament width measurements are mostly used for experimental validation and in-situ monitoring purposes. Besides simply monitoring the flow of materials, the quantitative data acquired via CV-based measurements may also be used to optimize printing parameters to achieve more consistent printing quality. In food printing, extensive trial-and-error experiments are often needed to understand the material extrudability, because printing materials are diverse and have complex rheological properties (Ma et al., 2021). To expediate the parameter tuning process of printing complex food materials, a CV-based measurement of instant flow rate can provide a helpful control strategy which leads to proper extrusion consistency and improved printing accuracy.

This study therefore aims to develop and evaluate a feedforward control method based on CV to improve the printing accuracy of complex food materials. Briefly, a CV-based tracking method was developed as a calibration step to measure the extrusion rate and extruded filament width of common food printing materials. The nozzle motion (i.e. nozzle moving velocity) was calibrated based on the measured instant extrusion rate and extruded filament width. The calibrated nozzle motion was then implemented to evaluate its effectiveness from two aspects: 1) extrusion latency compensation and 2) customized extrusion width. The calibrated nozzle motions were compared to the results with constant nozzle motion to demonstrate the improved printing accuracy.

4.2. Materials and methods

4.2.1. Printing materials

White chocolate spread (Albert Heijn, the Netherlands), lemon curd (Chivers, the Netherlands), dry cookie dough mix (Dawn Foods, the United States), and processed cheese (ERU, the Netherlands) were purchased from a local supermarket (Albert Heijn, the Netherlands). The cookie dough was prepared according to the manufacturer's instruction: 100 g of the dry cookie dough mix was combined with 14 g of butter and 9 g of water and mixed for 20 min using a kitchen mixer. The food materials were kept at 4 °C and tempered to 20 °C before use. Ingredient lists of food materials used in this study are included in Table 4.A1.

In the subsequent sections, the white chocolate spread and lemon curd were used to develop and validate the extrusion rate measurement method based on CV. The white chocolate spread and processed cheese were used to develop the extruded filament width measurement technique. After the methods were established, a series of calibrated motion controls were demonstrated using white chocolate spread, cookie dough, and processed cheese. The lemon curd was not used for printing demonstrations due to its large variations in extrusion rate measured from the method development phase. In the end of the study, processed cheese was printed into a complicated shape to demonstrate the performance improvement in a real printing application.

4.2.2. Printing material characterizations

To characterize the rheological properties of the materials, frequency sweeps were performed following the method of Zhang et al. (2020). Briefly, a rheometer equipped with a 20-mm cone and plate geometry (2° angle) was used (Anton Paar Physica MCR502, Anton Paar GmbH, Graz, Austria). The angular frequency was increased from 0.1 to 100 rad s^{-1}, and the corresponding storage and loss moduli were recorded to examine viscoelastic properties at the corresponding printing temperatures (20 or 50 °C).

To characterize the surface roughness of the extruded materials, they were carefully transferred into a syringe (⌀ 22 mm, Optimum Syringe Barrel, Nordson EFD, USA) connected to a dispensing nozzle with internal diameters varying between 0.84 to 1.54 mm (Nordson EFD, USA). The syringe was closed off by a pressure cap, placed onto a syringe

holder, and manually primed to avoid any dead volume. The materials were extruded through the nozzle using a texture analyzer (Instron 5564, Norwood USA) with a load cell of 2000 N. A camera (UI-3160CP-M, Imaging Development System, Germany) with a zoom length lens (6.5X Zoom Lens, Edmund Optics, UK) was placed 5 cm from the nozzle to monitor the material surface just below the nozzle, during extrusion.

4.2.3. Development of CV-based calibration tool

A CV-based method is developed to determine instant extrusion rate and filament width during the extrusion of food materials. During the method development process, a texture analyzer was used to perform compression tests to mimic the actual printing process.

4.2.3.1. Extrusion force and video acquisition

The material (see section 2.1) was extruded from the syringe using a texture analyzer. The stainless-steel probe installed on the texture analyzer performed a uniaxial compression test with a displacement of 5 mm at rates between 5 to 15 mm/min. These rates of compression simulate the linear feed rates commonly used in 3D food printing. A double compression test was conducted to determine the compression force profile during extrusion for each printing material. A 30-s rest time was set in between two compressions to simulate the re-pressurizing step in a 3D printing syringe. Using the feed rate of the piston, the average extrusion rate of the material was estimated based on the continuity equation (Moretti et al., 2021).

$$V_{ex} = V_{feed}\left(\frac{D_2}{D_1}\right)^2 \quad (1)$$

where V_{nozzle} is the average extrusion rate (mm/s), V_{feed} is the displacement rate of the compression piston (mm/s), D_1 is the nozzle diameter (mm), and D_2 is the syringe diameter (mm).

For each double compression test, a camera with a fixed focal length lens (25mm, Edmund Optics, UK) was placed 10 cm from the nozzle to monitor the extrusion process. The camera was controlled by the uEye Cockpit software (Imaging Development System, Germany). In the operating mode, the camera captures 300 x 400 pixel frames at frequencies ranged between 600 to 700 frames per second (FPS). The camera was triggered

simultaneously with the compression to conduct synchronized measurements of extrusion rate and force. The corresponding compressive force and material extrusion video were recorded to characterize the extrusion process.

4.2.3.2. Extrusion rate measurement

Prior to the extrusion rate measurement, a scaling factor (F_s) was calculated to convert the pixel distance to the real distance using the outer diameter of the nozzle as a reference distance. The extrusion rate was measured by estimating the material movement between 2 consecutive frames. A pixel at position (x, y) was selected on the current frame to mark the original position of the printing material. In the next frame, the new position of this pixel, (x', y'), was estimated using the Lucas-Kanade optical flow algorithm (Lucas & Kanade, 1981). The algorithm works with three key assumptions: the pixels have not displaced significantly across consecutive frames, the neighboring pixels have the same displacement, and the pixel intensity changes are smooth across frames. These assumptions are valid for non-transparent printing materials that yield sufficient surface roughness to have resolution between pixels. The extrusion rate (v) between consecutive frames was calculated by dividing the distance travelled by the pixel in these frames by time per frame and scaling the result by F_s (equation 2).

$$v = \frac{\sqrt{(x-x')^2+(y-y')^2}}{t} \times F_s \quad \textit{where } t = \frac{1}{FPS} \qquad (2)$$

The extrusion rate calculation between 2 frames was repeated until the point travelled 1 mm from the original point position. A new point was then selected back to the original position, and the same tracking process was repeated to ensure that the extrusion rate measured was within 1 mm below the nozzle (Figure 4.1A and B). The 1 mm maximal distance minimizes the effect of gravity on the extrusion rate and was selected to represent a real 3D food printing situation in which the printing material is dispensed onto the platform or a previous layer within the distance equal to the nozzle diameter (ranged from 0.84 to 1.54 mm). The raw data was smoothened using the Savitzky–Golay filter with 31 neighboring points, making the final measurement frequency around 0.05 s / measurement. The smoothened extrusion rate was analyzed and compared to the average extrusion rate calculated from the feed rate of the piston using the continuity equation (eq. 1). To evaluate the repeatability of the extrusion rate measurement, four different positions were tracked

from the same video recording. The coefficient of variation (standard deviation divided by mean) of four measurements was calculated to understand the reliability of the CV-based measurement.

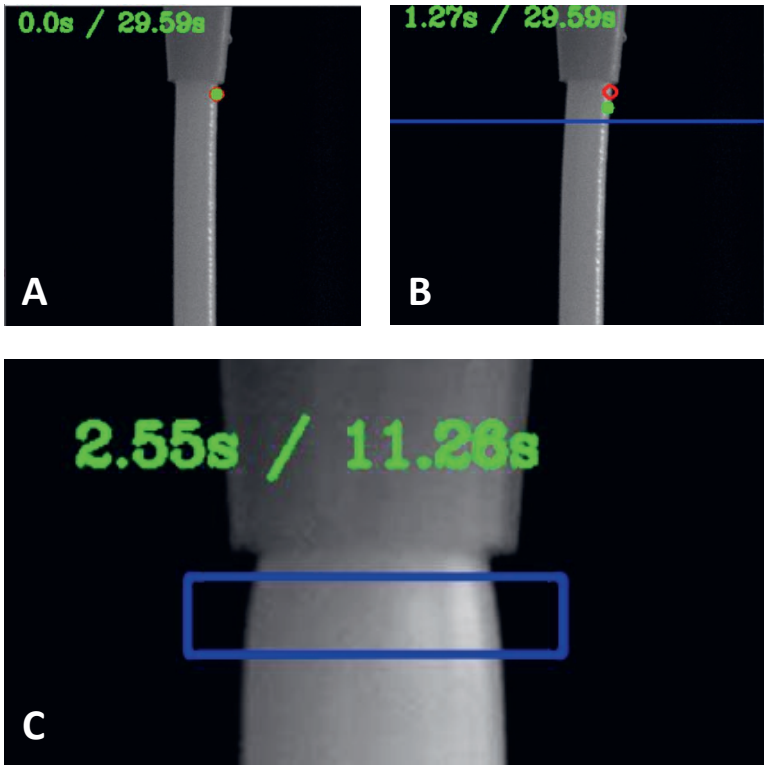

Figure 4.1. A: a snapshot of the initial frame of an extrusion video. B: a snapshot of the tracking during extrusion. The red circle represents the original position of the material green dot represents the current position of the material, the blue line represents the 1-mm mark line. C: Extruded filament width measurement. The width of the extruded filament was measured within the blue bounding box (< 1 mm below the nozzle).

4.2.3.3. Extruded filament width determination

From the same extrusion video, the width of the extruded filament was measured to quantify the "die-swell" of food materials. A bounding box was put within 1 mm of the nozzle position to select the area of interest for the extruded filament width (Figure 4.1C). The Canny edge detector was applied to determine the edge of the extruded filament (Canny, 1986). The row-wise pixel distance of the extruded filament was measured and converted into real distance using the calibration factor obtained from the extrusion velocity

measurement (section 2.4). The extruded filament width was averaged per frame and recorded to characterize the extruded filament width change over time during food printing. The mode of the extruded filament width (D_{ex}, mm) was used for calculating the die swell ratio with the following equation (3):

$$Swell\ Ratio = (D_{ex} - D_n) / D_n \quad (3)$$

where D_n (mm) is the diameter of the extrusion nozzle.

4.2.4. Feedforward control of nozzle motion

The aforementioned CV-based calibration tool was applied in the actual printing of food material. Printing experiments were carried out using an extrusion-based 3D printer modified with a pneumatic 3D printing system equipped with a syringe heater (DR-2203, Nordson EFD, USA) (Schutyser et al., 2018). The motion control of the dispensing system is independent from the air-pressured extruder, allowing motion flexibilities such as acceleration and deceleration without impacting the extrusion flow.

4.2.4.1. Extrusion latency compensation

To compensate for the extrusion latency from the printer and the material elasticity, a nozzle motion acceleration profile was developed based on the measured extrusion rate. The printing materials were carefully loaded into a printing syringe, and the syringe was closed off with a pressure cap and tempered at printing temperatures between 20 and 50 °C for 10 min prior to printing. The same camera (see section 2.2) was placed 10 cm from the printing nozzle to capture a point dispensing of the printing material. The extrusion rate (V_{ex}) of the material was measured using the CV-based method introduced in the section 2.4. The nozzle velocity (V_n) profiles were calculated with the continuity equation (eq. 4).

$$V_n = V_{ex} \left(\frac{D_{ex}}{D_t}\right)^2 \quad (4)$$

where D_{ex} (mm) represents the width of the extruded filament, and D_t (mm) represents the target extrusion width. For extrusion latency compensation experiments, the D_{ex} and D_t were set to be equal to each other, assuming no die swell during extrusion.

Five parallel lines of 80 mm were printed using constant and calibrated nozzle motions. This printing pattern was chosen to showcase the re-pressurizing process of the syringe (i.e. start-stop cycles) before printing a next line when under-extrusion of viscoelastic materials often occurs (Fahmy et al., 2020a; Nijdam et al., 2021). The length accuracy of the lines was expressed as a percentage of the actual length measured using ImageJ software divide by the target length times 100.

4.2.4.2. Customized extrusion line width

By controlling the nozzle velocity, one can minimize the effect of the die swell and customize the extrusion line width. Based on eq. 4, the target extrusion width (D_t) is usually set to be the width of the nozzle (although one can alter the extrusion line width based on different nozzle motion profiles (Moetazedian et al., 2020)). To demonstrate the extrusion line width customizations, squares with 3 different target widths were printed for white chocolate spread, cookie dough, and processed cheese. Using the ImageJ software, the actual printed width was measured from duplicated printings. The accuracy of the extrusion width customization was expressed as a percentage of the measured width divide by the target width times 100.

4.2.5. Software development and availability

The CV software was developed in-house using the OpenCV, NumPy, Pandas, and PIMS libraries in the Python programming language. The software, including a graphical user interface, raw scripts, and demonstrations can be accessed through https://git.wur.nl/yizhou.ma/extrusion-flow-tracker.

4.3. Results and discussions

4.3.1. Printing material characterizations

Four representative food materials used for printing were selected, differing in their rheological behavior, printing temperatures (20 °C or 50 °C) and surface roughness. The rheological behavior influences the extrusion and the appearance influences the optical measurement of extrusion rates (Greeff and Schilling, 2017; Z. Liu et al., 2019). Figure 4.2 shows the frequency sweeps of the printing materials. The storage and elastic moduli of all four materials showed power-law dependencies on the shear frequency, indicating that the materials are viscoelastic soft solids that are suitable for 3D food printing applications

(Sridharan et al., 2021). The storage moduli of cookie dough, lemon curd, and white chocolate spread are greater than the loss moduli at all frequencies measured, indicating a solid-like rheological behavior for these three materials, which allows extrusion at room temperature. White chocolate spread has the highest storage modulus, showing more elasticity than cookie dough and lemon curd. Although the printing materials differ in terms of storage and loss moduli, the solid-like materials fall into the typical range of storage moduli as reported by other 3D food printing studies (Z. Liu et al., 2020; Zhu et al., 2019). Processed cheese has a melting transition at the measuring temperature of 50 °C, and therefore at frequencies below 15 rad/s, behaves liquid-like. This liquid-like behavior is required for extrusion and fusion of the printed cheese (Le Tohic et al., 2018). This melting transition gave the processed cheese more frequency-dependency compared to the other food materials and stronger shear-thinning behavior. The rheological properties of the four printing materials are consistent with those reported in previous literature, which illustrates their suitability to use as representative materials for examining the feedforward control method developed in this study.

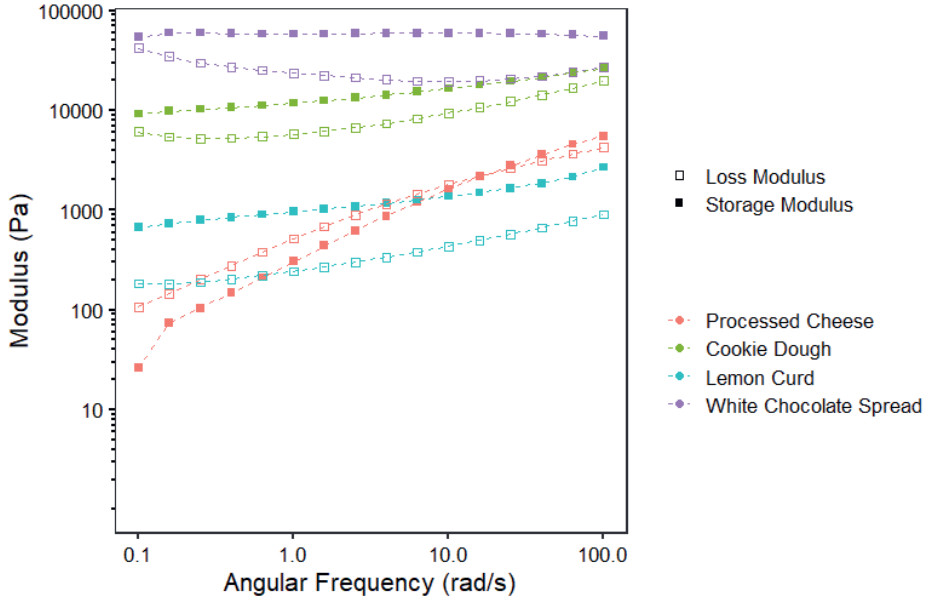

Figure 4.2. Frequency sweeps of white chocolate spread, lemon curd, cookie dough, and processed cheese. White chocolate spread, lemon curd, and cookie dough were measured at 20 °C, and processed cheese was measured at 50 °C. The closed symbols represent the storage modulus, and the open symbols represent the loss modulus obtained under a constant shear strain of 0.5%.

In addition to rheological properties, surface opacity and surface roughness of the food materials are important as they may influence the performance of the optical flow tracking algorithm (Greeff and Schilling, 2017). Optical methods are in general limited to opaque materials with rough surfaces because the optical flow algorithm tracks changes in pixel intensity during extrusion (Nuchitprasitchai et al., 2017). Figure 4.3 shows the surface roughness of the 4 printing materials as they were extruded out of the nozzle. Inhomogeneity in the materials caused somewhat irregular extrusion rates which then resulted in grains and cavities on the surface of all 4 materials, providing sufficient surface roughness for optical motion tracking. Preliminary experiments with smooth-surface hydrogels made from sodium alginate (i.e. a common bioprinting material) showed these to be unsuitable for optical tracking methods. Therefore, the method proposed in this study is aimed at opaque materials with some degree of surface roughness, as food materials commonly are.

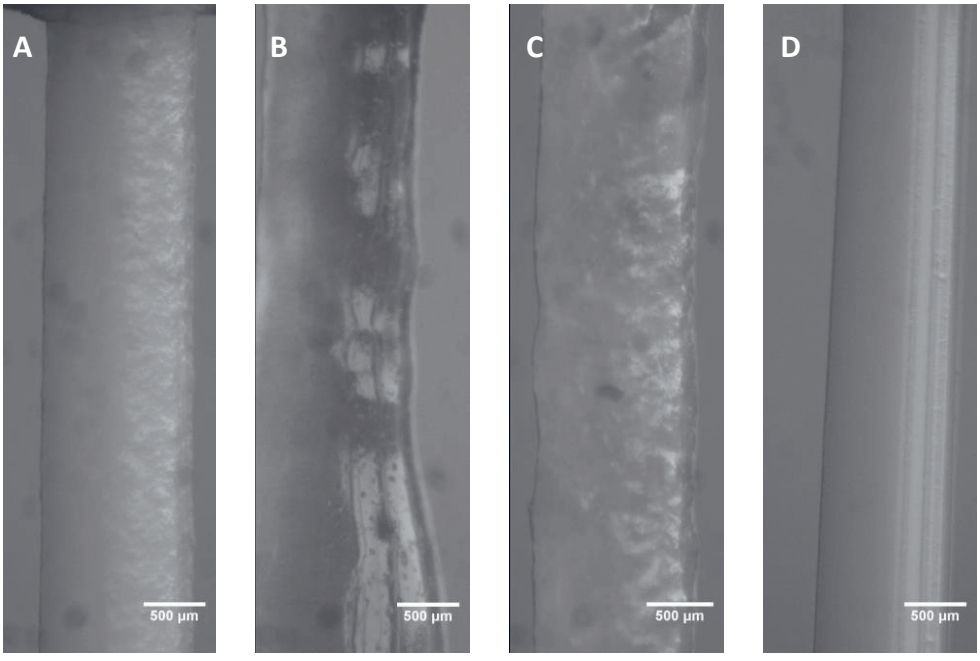

Figure 4.3. Surface roughness of the printing materials. A: white chocolate spread, B: lemon curd, C: cookie dough, and D: processed cheese. Samples were imaged as they were extruded from the printer using a 6.5 X zoom length lens.

4.3.2. Extrusion rate measurement

The precision of the CV-based method for extrusion rate measurement was first evaluated. White chocolate spread was extruded using a double compression that was described in section 2.4 at 20 mm/s feed rate, and the corresponding material extrusion was recorded and analyzed. Using the same video recording, the extruded filament tracking was repeated 4 times and the corresponding extrusion rate was calculated. From the 4 repeated extrusion rate measurements shown in Figure 4.4A, a coefficient of variation of 1.19% was derived. This small variation showed that the CV-based measurement is repeatable, indicating its reliability as a calibration tool for 3D food printing.

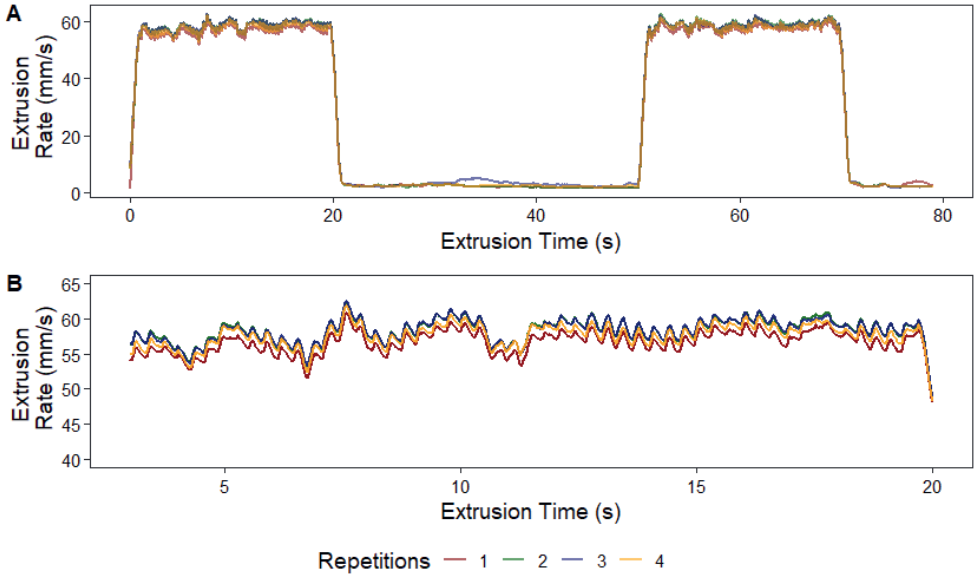

Figure 4.4. A: Four repeated analysis of the same video recording of white chocolate spread during extrusion, using the developed CV-based method. B: zoomed in stable range of the extrusion rate; the coefficient of variation in the stable extrusion range is 1.19%.

The measurement accuracy was also examined by combining the extrusion force measurement and the average extrusion rates calculated from the continuity equation (eq. 1). Figure 4.5A shows the extrusion force profiles of printing the white chocolate spread. At the initiation stage of the extrusion, a latency period was observed as the force gradually increased while the piston displacement moved at a constant rate. The latency was caused

by compressibility of the syringe holder and food materials. Even though pure food materials are often incompressible, in complex food systems, small air bubbles can often be suspended in food materials, contributing to the apparent compressibility from the printed foods. As a result, in real printing applications, the latency is often linked to the under-extrusion at the beginning of printing a structure. As the compression continued, the measured force plateaued until the end of the pressing cycle. When the piston movement stopped, the extrusion force gradually decreased until the second compression started, while the remaining pressure in the syringe continues to push materials out of the nozzle. The gradual release of syringe backpressure often corresponds to the over-extrusion (i.e. oozing) of material during printing.

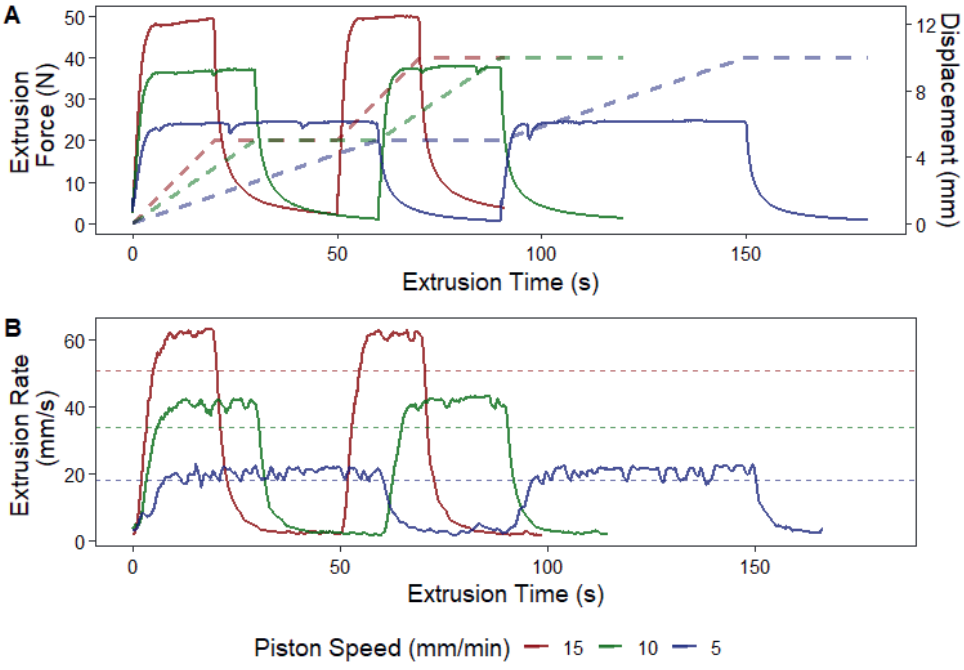

Figure 4.5. Results obtained from the double compression test of white chocolate spread at different piston displacement speed of 5, 10, and 15 mm/min. A: extrusion force (solid lines, primary y-axis) and accumulated displacement distance of the piston (dashed lines, secondary y-axis) over time. B: extrusion rate over time; the dotted line in B represents the average extrusion rate calculated from the continuity equation (eq.1). The red arrows point at drops of extrusion force and rate, which was likely caused by the inhomogeneity of the sample.

A similar force increase and a plateau were observed for the second compression period. The extrusion force profiles were consistent across different piston feed rates, and a faster

feed rate always resulted in shorter time taken to reach the force equilibrium. Such changes in force were also observed from the extrusion rate measurements as shown in Figure 4.5B. Due to the changes in the extrusion force, the extrusion rate also accelerated and decelerated again during the extrusion (i.e. in each start-stop cycle). The acceleration of the extrusion rate lasts between 2 to 5 s depending on the different feed rates. Prior to the plateau phase, the extrusion latency leads to under-extrusion issues if the nozzle motion is set constant. Therefore, incorporating of an acceleration phase in nozzle motion (i.e. a calibration) can compensate for the extrusion latency caused by syringe pressurization and food compressibility.

The extrusion force and rate profile of plastics were measured and reported in several other studies. Similar acceleration phases were reported before reaching the extrusion force equilibrium (Moretti et al., 2021; Serdeczny et al., 2020a). For plastic printing reported in literature, the extrusion force and rate changes are smoother than that were observed from food extrusions. This is likely due to the more homogeneity of these plastics, while the heterogeneity and air bubbles trapped in the food materials lead to some irregularity in the extrusion. However, as shown in Figure 4.5, a sudden decrease in force is often matched with a sudden decrease in extrusion rate, showing that the extrusion rate measurement is fully consistent with the force measurement. The dashed lines in Figure 4.5B show the average extrusion rate calculated from the continuity equation (eq. 1). These average rates underestimate the actual extrusion rate because the continuity equation ignores the extrusion acceleration at the beginning of each push. This underestimation is proportional to the extrusion rate: a larger underestimation was observed for the faster extrusion rate. When the nozzle motion was referenced to this average extrusion rate (i.e. a constant nozzle movement speed is chosen throughout printing), it is likely that the extrusion will suffer from inconsistency due to acceleration and deceleration during actual extrusions.

Figure 4.6 shows the results obtained from the double compression experiments conducted for lemon curd. The extrusion force and rate matched, similar to the white chocolate experiment. The jelly-type material required much less force to extrude because of its lower storage modulus compared to the white chocolate spread (Figure 4.2). The lemon curd also showed more variation in the extrusion rate and force measurements, which is likely because of the air bubble trapped in the material. The inhomogeneity of the lemon curd was

reported earlier by Vancauwenberghe et al. (2017) when printing pectin-based snack foods (Vancauwenberghe et al., 2017). The porosity and rough surface of the extruded filament confirmed that air bubbles can impact the final printing outcome of pectin-based foods (Figure 4.3B). Such inhomogeneities in food materials are randomly distributed, which leads to challenges to establish predictive models to counter such effects. A feedforward approach can adapt to the general acceleration and deceleration phases appearing in the extrusion rate profile, but it is still incapable of reacting to the small, fast variations in extrusion rate caused by the inhomogeneity. As an alternative solution, pre-treatments such as centrifugation/degassing has been used by others to achieve consistent food texture before printing (Zhu et al., 2019). Overall, the CV-based extrusion rate measurement agrees well with the extrusion force measurement. The measured instant extrusion rates appeared to be dynamic and greater than the averaged extrusion rate, which provides the necessary information for the subsequent nozzle motion planning step in this study.

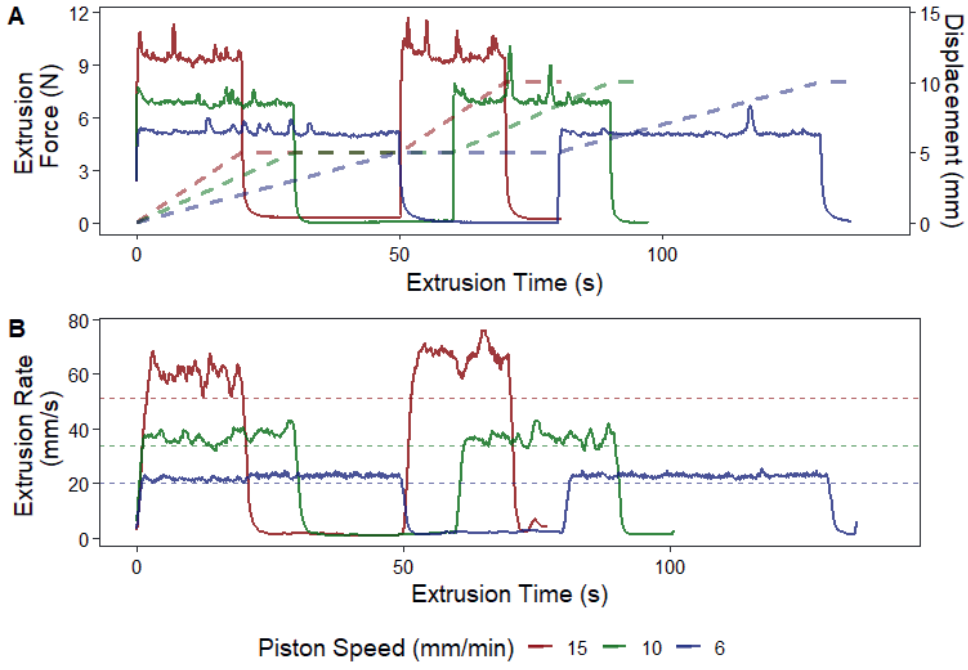

Figure 4.6. Results obtained from the double compression test of lemon curd at different piston displacement speed of 6, 10, and 15 mm/min. A: extrusion force (solid lines, primary y-axis) and accumulated displacement distance of the piston (dashed lines, secondary y-axis) over time. B: extrusion rate over time; the dotted line in B represents the average extrusion rate calculated from the continuity equation (eq.1).

4.3.3. Extruded filament width measurement

While measuring the extrusion rate, the width of the extruded filaments was also measured to characterize the die swell during extrusion. Figure 4.7 shows the change of the extruded filament width over time for processed cheese and white chocolate spread. The two materials vary largely in compositions, which is also reflected in their differences in die swell during extrusion. For white chocolate spread, a swelling ratio of ~ 0.15 is observed for extruded filaments printed at 1, 1.5, and 2 bars. The initial extruded filament width (ranged between 0.2 to 0.6 mm) expanded to a stable width of 0.95 mm in less than 0.5 s (Figure 4.7A). The initial width expansion is likely to be caused by the velocity distribution during pipe flow as materials closer to the center of the pipe travel faster than closer to the wall (Haavisto et al., 2017). The swell of the extruded filament is relatively independent from the extrusion pressure range, suggesting that the increase of the extrusion pressure, therefore the wall shear stress, has negligible influence on the die swell. Sombatsompop and Dangtangee reported a logarithmic relation between the wall shear stress and the die swell of viscoelastic fluids (Sombatsompop and Dangtangee, 2002). They showed that above a certain threshold of wall shear stress, the die swell ratio becomes relatively independent of the wall shear stress. The white chocolate spread used in this study behaves similarly, with a consistent die swell ratio of 0.15 across different extrusion pressures.

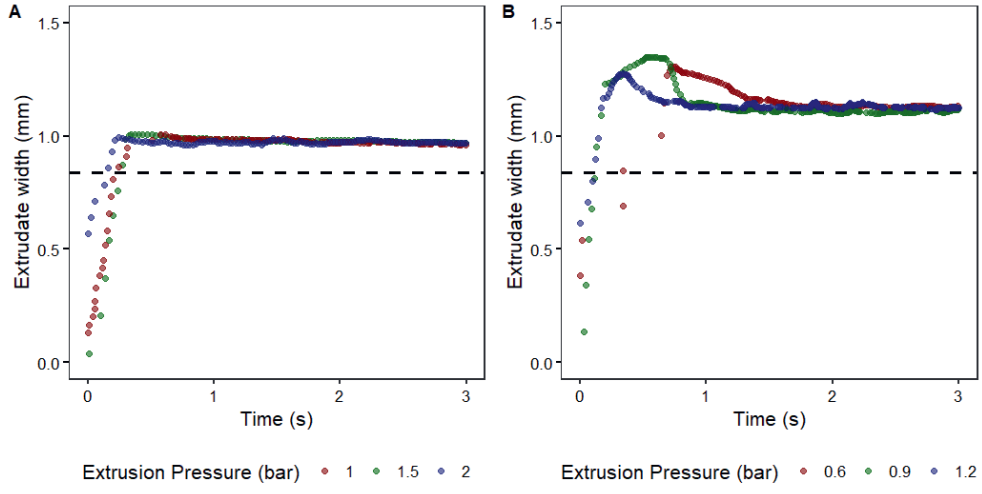

Figure 4.7. Extruded filament width measurement over time. A: white chocolate spread. B: processed cheese. The black dashed line represents the inner diameter of the printing nozzle (0.84 mm).

For the extruded processed cheese filaments, more die swell (die swell ratio = 0.3) was observed compared to the white chocolate spread (Figure 4.7). Processed cheese contains casein micelles which deform during flow and relax back towards their original shape upon pressure release. The processed cheese also showed an initial width expansion, most probably attributed to its unique rheological properties related to the deforming casein micelles. Note that the initial width of the processed cheese filament was higher than that of the white chocolate spread, likely because processed cheese is more shear-thinning as shown in Figure 4.2 (i.e. the moduli of processed cheese is more impacted by the increase of shear frequency). The higher degree of shear-thinning leads to a 'flatter' velocity profile in the pipe resulting in flow closer to plug flow, which ultimately leads to the wider initial extruded filament width observed here (Haavisto et al., 2017). Uniquely observed for processed cheese, the die swell was initially very fast, which then slowed down and attained a stable width. The large initial width expansion can be attributed to the cooling of the material at the nozzle: preliminary experiments suggested a 10 °C temperature drop between the set extrusion temperature and the actual nozzle temperature. This temperature drop lead to increased elasticity during flow, which created more backpressure during extrusion and a higher initial swell of the material. After the initial swell, the melted cheese was continuously extruded to reach a steady state of a consistent width expansion. During the steady state, a minimal impact of extrusion pressure was found on extruded filament width, suggesting that the applied extrusion pressure range (0.6 to 1.2 bar) had small impact on die swell. Overall, both processed cheese and white chocolate spread swell upon extrusion, indicating that the extruded filament width is greater than the nozzle size (Ma et al., 2021; Ross et al., 2021). The measured extruded filament width can be used as inputs to dynamically control the printed filament width by customizing the printing speeds.

4.3.4. Feedforward control of nozzle motion

4.3.4.1. Extrusion latency compensation

Several food materials were printed using a pneumatic 3D printer to implement the feedforward control of nozzle acceleration. For all materials, the printing pressure was adjusted to achieve extrusion rates of ~ 40 mm/s to simulate regular food printing. The CV-based method was used to determine the onset of extrusion, and the measured extrusion rates were used to find the required nozzle acceleration for feed forward control. Figure 4.8 shows the nozzle acceleration and the corresponding lines printed using white chocolate

spread, cookie dough, and processed cheese. The nozzle velocity (~40 mm/s) was set to match the plateau velocity that would lead to the required steady-state line width based on the extrusion rate measurement. The printed lines with a constant nozzle motion suffered from under-extrusion as they appeared to be shorter than those printed with a calibrated nozzle motion (Figure 4.8). The accuracies of the printed lines are summarized in Table 4.1. For the three printing materials, the calibrated printing achieved accuracies ranged from 97.9 to 100%. Compared to the constant printing, the calibrated printing improved the length accuracies ranging from 4.7 to 10.6%. The under-extrusion was consistently found to be at the beginning of the line extrusion, which corresponds to the start-stop point of 3D printing. As the printing syringe is pressurizing, the under-extrusion is likely caused by the high elasticity and yield stress of the food materials (Fahmy et al., 2020b). Under air pressure, the food materials, which may contain some air bubbles, can be compressed somewhat before extrusion, leading to latency and a slower acceleration in extrusion. Figure 4.8 also shows that each material has a unique acceleration profile, which is related to their rheological properties – other studies showed that shear thinning influences the extrudability of food materials (Z. Liu et al., 2019; Ma et al., 2021). Preliminary measurements suggested that the white chocolate spread was the most shear-thinning sample compared to the cookie dough and processed cheese. The white chocolate spread also required the least amount of distance to reach the 40 mm/s steady speed. The flow rate of shear-thinning materials follows a power-law relation as a function of pressure, suggesting that white chocolate spread is more sensitive to pressure change, which resulted in a faster acceleration than the other less-shear-thinning materials.

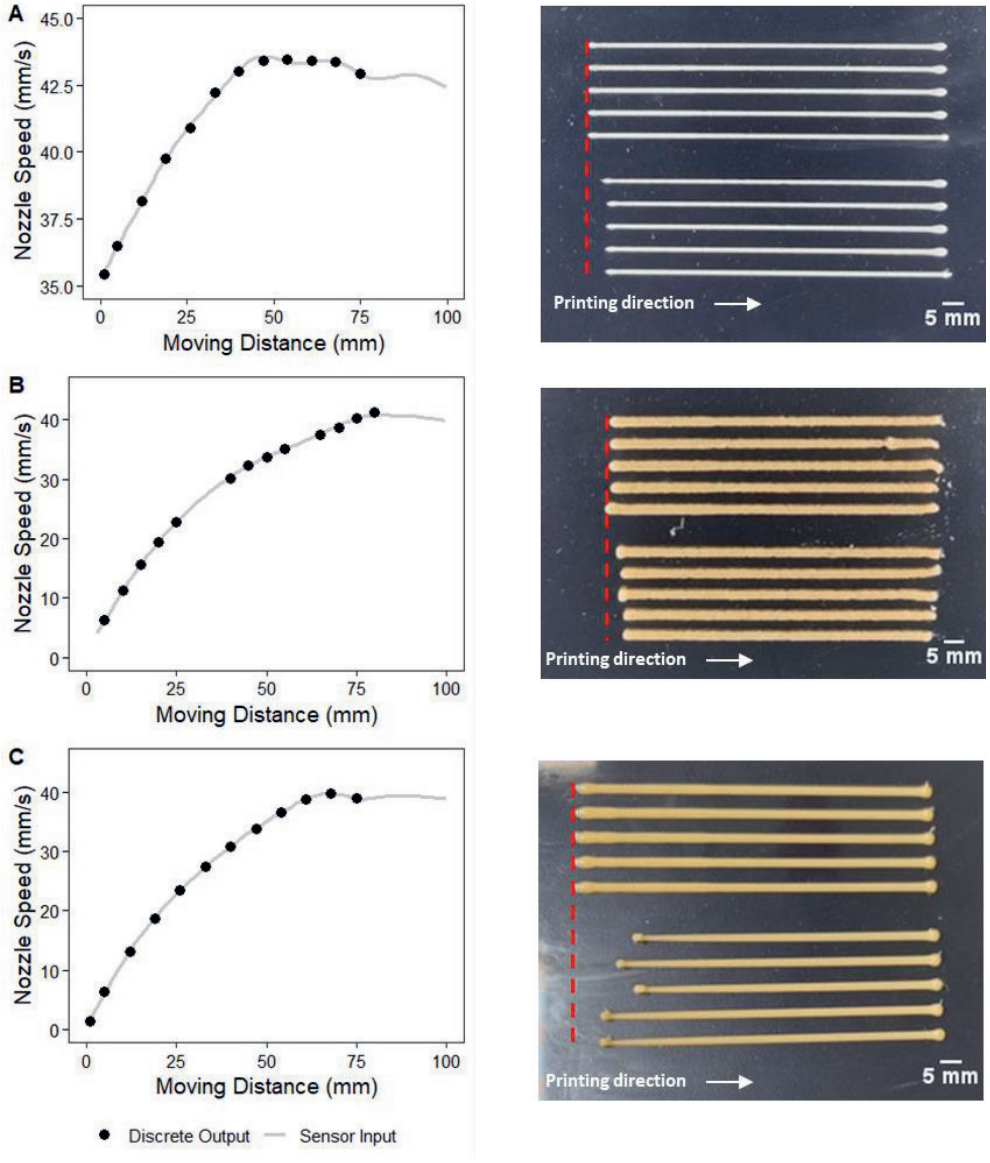

Figure 4.8. Calibrated nozzle motion profiles and printing results. A: white chocolate spread, B: cookie dough, C: processed cheese. The top 4 stripes were printed with calibrated nozzle motion and the bottom 4 stripes were printed with constant nozzle motion. The round dots represent the discrete outputs sent to the printer to achieve the calibrated printing. The red dashed lines represent the start position of the line extrusions.

Table 4.1. Printing length accuracy comparison between calibrated and constant printing of white chocolate spread, cookie dough, and processed cheese. (Target line length = 80 mm).

Printing Profile	Sample	Length accuracy ± standard deviations (%)
Calibrated	White Chocolate Spread	99.0 ± 0.6
	Cookie Dough	97.9 ± 1.1
	Processed cheese	100.0 ± 1.2
Constant	White Chocolate Spread	93.7 ± 0.7
	Cookie Dough	93.2 ± 1.7
	Processed cheese	89.4 ± 5.2

In Figure 4.8C and Table 4.1, processed cheese shows the most severe under-extrusion and the least accurate length under constant printing. From the rheological measurements (Figure 4.2), melted processed cheese (50 °C) has moderate elasticity and is liquid-like at low frequency (below 15 rad/s). The under-extrusion of processed cheese was likely caused by the change in nozzle temperature during printing. The temperature drop caused a solidification of the cheese, which lead to delayed extrusion and subsequent larger 'blob' of deposited cheese, as shown in Figure 4.8C. Extrusion accuracy improved for the last 2 lines printed in Figure 4.8C, suggesting that the previously printed lines may have warmed the nozzle such that subsequent lines were more accurately printed. The improved printing length may also contributed to the larger length accuracy standard variation found for the processed cheese (Table 4.1). This nozzle temperature effect of cheese was also observed from the extruded filament width measurement (Figure 4.7B), as an initial swell was observed, which corresponds to the "rounded tip" on the constantly printed lines. The delayed extrusion was also captured by the CV-based method, and the feedforward nozzle acceleration prevented under-extrusion. Such an extrusion latency can be alleviated by a nozzle heater to better control the extrusion temperature at the nozzle. Despite different reasons that can cause under-extrusion, the CV-based method was able to measure the extrusion rate, implement the feedforward control, and improve the printing accuracy.

4.3.4.2. Customized extrusion line width

After compensating for the extrusion latency, extrusion line width customization was further implemented. Based on the extruded filament width measurement, nozzle velocity was adjusted based on the intended filament width (eq. 4). Figure 4.9 shows the nozzle velocity profiles needed to achieve the target printing width for the printing materials. The

nozzle velocity profiles in Figure 4.9A, C, and E are similar to those shown in Figure 4.8. The initial accelerations compensated the extrusion latency, and the slope and peak nozzle velocity determined the width of the extrusion lines. As reported in other studies, altering the nozzle motion can result in differences in extrusion line width (Comminal et al., 2019; He et al., 2016; Ma et al., 2021). The examples shown in this study suggest that one can better achieve the target extrusion width by controlling the nozzle velocity based on the continuity of volume transfer, when the extrusion force/pressure was kept constant. To assess the width customization accuracies, Table 4.2 provides the width printing accuracies compared to the target widths. The measured line widths validate the control strategy because the width accuracy ranged between 95 to 107% (above 100 % means over-extrusion).Width variations were represented by the standard deviation of the width accuracy. By visual inspections in Figure 4.9B, D, and F, the targeted line width was achieved on most positions of the square, except at corners. Over-extrusion was found on the corners due to the deacceleration of the nozzle when making turns. The degree of over-extrusion increases with faster printing velocity, and this is due to the stronger deceleration needed for faster printing. This mechanical limitation of the printing platform can lead to printing inaccuracies, as also reported by Comminal et al. (2019). The width customization developed in this study can be potentially implemented to better printing complex structures when different printing resolutions are needed, by dynamically controlling the printing motion.

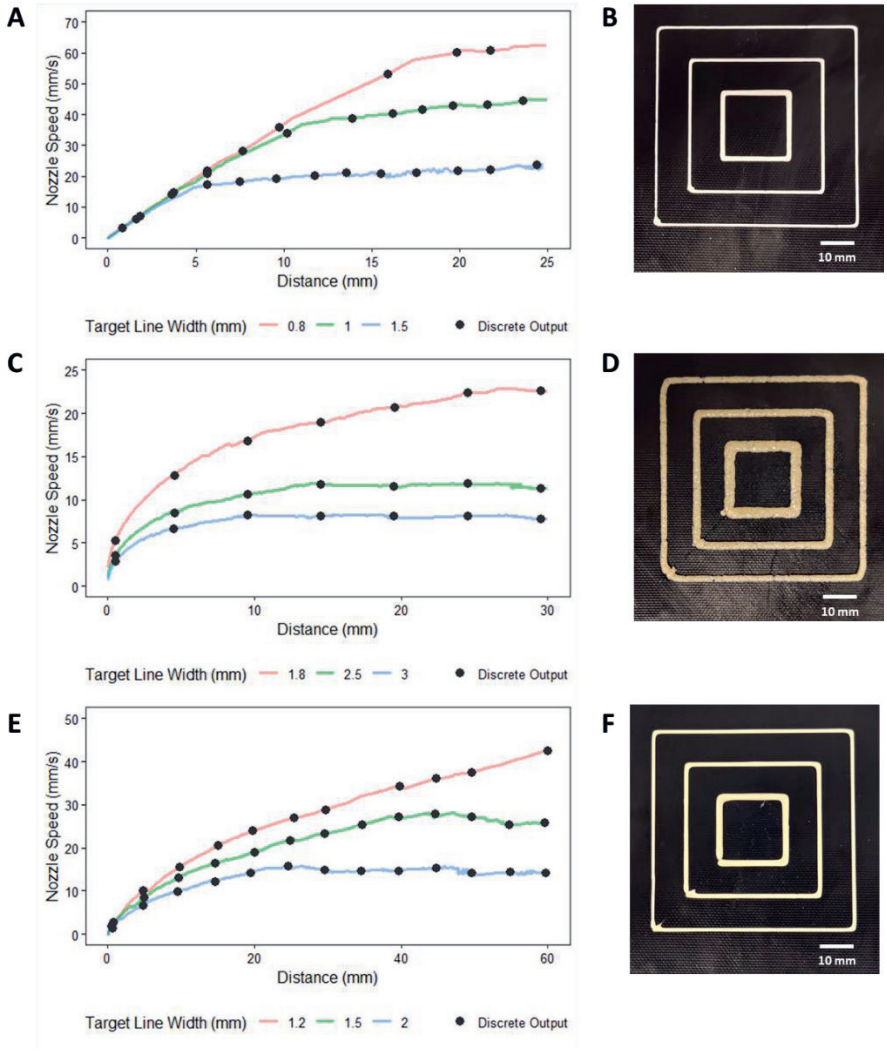

Figure 4.9. Customized extrusion line width showcase. A: nozzle (⌀ 0.8 mm) velocity profiles for white chocolate spread of different target line widths. B: Printed squares based on customized extrusion line width. Outer square (0.8 mm), middle square (1.2 mm), and inner square (1.5 mm). C: nozzle (⌀ 1.8 mm) velocity profiles for cookie dough of different target line widths. D: Printed squares based on customized extrusion line width. Outer square (1.8 mm), middle square (2.5 mm), and inner square (3 mm). E: nozzle (⌀ 1.2 mm) velocity profiles for processed cheese of different target line widths. F: Printed squares based on customized extrusion line width. Outer square (1.2 mm), middle square (1.5 mm), and inner square (2 mm).

Table 4.2. Accuracy evaluation of the customized extrusion width of white chocolate spread, processed cheese, and cookie dough.

Sample	Target width (mm)	Width accuracy ± standard deviations (%)
White Chocolate Spread	0.8	104.9 ± 5.0
	1.0	107.0 ± 5.4
	1.5	101.7 ± 2.7
Processed cheese	1.2	100.4 ± 2.9
	1.5	95.0 ± 7.4
	2.0	100.8 ± 4.9
Cookie Dough	1.8	105.0 ± 3.8
	2.5	95.8 ± 2.0
	3.0	101.0 ± 4.3

4.3.4.3. Printing improvement demonstration

To further illustrate the improvement in printing that can be achieved with the CV-based method, Figure 4.10 shows a top-view comparison of a single layer and a sideview comparison of layer stackings. The graphic design in Figure 4.10A was printed by four continuous lines. The red arrows point at the pressuring/starting position of a new extruded line. Similar to the observations in Figure 4.8, with a constant nozzle motion, under-extrusion was observed at the start of each extrusion, resulting in gaps in the single layer extrusion. With the nozzle acceleration implemented, the under-extrusion was much reduced to improve the layer completion (Figure 4.10B). The under-extrusion of each layer can also harm layer stacking and cause slippage (Figure 4.10C). With the calibrated nozzle motion, each layer was better extruded and stacked to achieve accurate printed structures (Figure 4.10D).

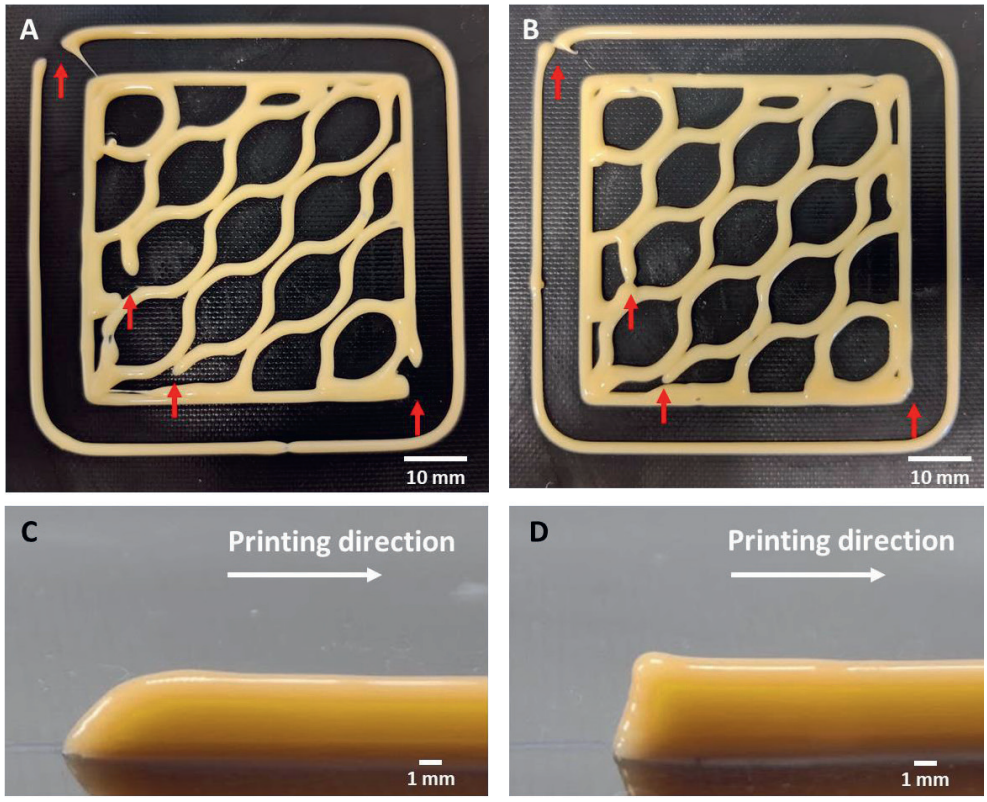

Figure 4.10. Printing accuracy improvement showcase. A: a processed cheese honeycomb layer printed with constant nozzle motion. B: a processed cheese honeycomb layer printed with calibrated nozzle motion. C: Sideview of layered processed cheese printed with constant nozzle motion. D: Sideview of layered processed cheese printed with calibrated nozzle motion. The red arrows in A and B indicate the pressurizing positions of the printing path.

4.3.5. General discussion

While the CV-based feedforward control method can give practical and good printing accuracy improvement, it still carries a few limitations. First, the printing materials should be sufficiently opaque and have sufficient surface roughness to create pixel intensity differences that can be picked up by the algorithm. Without pixel intensity changes among the frames, it is impossible to track the extruded filament movement and measure the extrusion rate based on an optical method. Second, the feedforward control of the nozzle motion assumes that the robotic platform can achieve sufficient acceleration to ensure an almost-constant instant nozzle velocity. Too large variation of the nozzle velocity during printing will result in over-extrusion, due to insufficient acceleration and deceleration (as

observed in Figure 4.9), and one should reduce the nozzle plateau velocity to better match the printer's capacity (Ertay et al., 2018). In this study, a pneumatic dispensing system was used to independently control nozzle motion and extrusion, which realized the printing accuracy improvement. However, the traditional G-code-based control treats the extrusion axis as a secondary axis to the motion, which limits the motion control independency demonstrated in this study. Lastly, since the calibration step relies on data obtained from a static extrusion, gravity effects were ignored when calculating extrusion rate and extruded filament width. When applying this method in practice, extrusion rate tracking and extruded filament width measurement should focus only on 1 mm below the nozzle, to minimize gravitational impacts.

With the assumptions in mind, the feedforward control method uses a CV-based calibration step to determine the nozzle motion for printing food materials. Compared to other flow rate measurements such as ultrasound and conductivity, the CV-based method is simple and modular, and easy to re-implement on existing 3D food printers. The open-source video analysis software, that is made publicly available with this study, includes a user-friendly graphical interface to conduct the required measurements. The feedforward control that is discussed in this study does not provide feedback for in-process control (although it could be combined with this in principle, and is a potential future application). However, because of the varying material properties of food, the simplicity and flexibility of this CV-based method makes its implementation for 3D food printing applications straightforward, avoiding time and resources expenditure in trial-and-error experiments, as is usually required. With this method, 3D food printing will further advance as an on-demand tool that can rapidly and accurately manufacture foods based on consumer needs, without requiring much more complicated equipment and increasing food production efficiency.

4.4. Conclusions

This study developed and evaluated feedforward control of the nozzle motion to optimize the extrusion line width and improve the printing accuracy. A sideview camera filmed the extrusion of food materials at the nozzle to in-situ measure the extrusion rate and extruded filament width using an optical flow algorithm. This CV-based method is repeatable and reliable and works with opaque materials with surface inhomogeneity (as is the case for most food printing materials). The initial extrusion latency caused by the elasticity of the

food materials, was compensated in the nozzle motion which led to much better initial extrusion line consistency. The extruded filament width measurement was used to customize filament width to achieve a higher degree of flexibility in 3D food printing. Three food printing materials were tested using the feedforward control to characterize material variations, and the method prevented under-extrusion of the food materials and improved printing accuracy in terms of 2D layer formation and 3D filament stacking. This CV-based method is simple to be implemented on most extrusion-based food printers as a material calibration tool to improve printing accuracy and avoid extensive trial-and-error experiments in 3D food printing. Future research can focus on implementing the CV-based method in closed-loop controls of 3D food printing to automate the parameter optimization process.

4.5. Appendix

Table 4.A1 Ingredient lists and purchase dates of commercial food products used in this study

Product	Purchase Date	Ingredients
ERU Slices Cheddar	March, 2021	55% cheese (of which 50% cheddar), water, milk proteins, whey powder, butter, melting salts (e452), salt, coloring (paprika extract).
AH Chocoladepasta wit	March, 2021	Sugar, vegetable oil (rapeseed, palm), dried skimmed milk powder, vegetarian whey powder, cocoa butter, whole milk, milk fat powder, emulsifier (lecithin [E322]), vanilla aroma, antioxidant (tocopherol-rich extract [E306]).
Chivers Lemon curd	March, 2021	Sugar, water, palm oil, lemon juice from concentrate (3%) maize flour, egg powder, food acids (citric acid, acetic acid), gelling agent (pectin), acidity regulator (sodium citrate), lemon oil (0.16%), color (carotenes), antioxidant (ascorbic acid).
Dawn Cookie Mix Plain	May, 2021	Wheat flour, sugar, vegetable oil, demerara sugar, whole egg powder, whey solids, dextrose, raising agent (sodium bicarbonate), glucose syrup, salt, natural flavoring.

Chapter 5 Thermographic and rheological characterization of viscoelastic materials for hot-extrusion 3D food printing

This chapter has been published as: Ma, Y., Schutyser, M. A. I., Boom, R. M., & Zhang, L. (2022). Thermographic and rheological characterization of viscoelastic materials for hot-extrusion 3D food printing. Innovative Food Science & Emerging Technologies, 81, 103135.

Chapter 5

Abstract

Thermoreversible food materials are suitable for hot-extrusion 3D food printing (HE-3DFP) to customize food designs and enable on-demand food production. A challenge of HE-3DFP is to control the material phase transition such that it melts to allow flow and extrusion and rapidly solidifies afterwards to obtain stable printed structures. We here report on the use of thermal imaging to simultaneously monitor material cooling and deformation of common thermoreversible food materials during HE-3DFP. Thermographic and rheological measurements show that the structural deformation is driven by slow material cooling and prolonged printing time. The surface temperature of printed objects is a good indicator for structural stability. Solidification mechanisms such as cross-linking or strong particle jamming are required to prevent deformation in time (i.e. creep) during printing. Thus we recommend to set the printing temperature just above material's gelation temperature to ensure proper extrudability and structural stability of the printed foods.

5.1. Introduction

3D printing of foods offers the ability to customize food design and enables on-demand production to create food products that tailor towards specific consumer preferences and dietary needs (Ma and Zhang, 2022). Extrusion-based 3D food printing is the most popular printing technique thanks to its simplicity and suitability to print viscoelastic food materials. The food materials are extruded through a nozzle, and the 3D structures are subsequently built layer-by-layer onto a robotic platform. Various food materials have been formulated with the aim to realize personalized food production by altering the texture and spatially delivering flavors in printed foods (Ma and Zhang, 2022). Among the available food materials for 3D printing, a subset exhibits thermoreversible behavior. Thermoreversible materials are easy to store and transport because they are solids at room temperature. This behavior is desirable for extrusion-based 3D food printing applications, in which food materials can be liquified to assist pressure driven flow and thus extrusion and solidified on the printing platform to obtain stable 3D structures. This printing technique is also referred to as hot-extrusion 3D food printing (HE-3DFP). Typical food materials that are suitable for HE-3DFP include chocolate, processed cheese, and various food hydrocolloids composed of milk proteins, carrageenan, agar, and gelatin (Liu et al., 2022; Rando and Ramaioli, 2021; Ross et al., 2021).

During HE-3DFP, heating is applied to a non-Newtonian food material to liquify the material and enhance its extrudability after which it cools down, fuses with the previously deposited material, and solidifies into a stable structure. These phenomena are influenced by several printing parameters such as the printing temperature, the printing speed, the ambient temperature, and the extrusion pressure. The printing temperature and speed are the key parameters reported by previous studies to determine the printability of chocolate and thermoreversible hydrogels (Lanaro et al., 2017; Rando and Ramaioli, 2021; Vadodaria et al., 2021). Improper control of the printing parameters may lead to printing failures such as material spreading, structural collapses, and insufficient fusion between layers. Specifically, overheating the printing material may lead to poor extrudability which leads to spreading and spraying of the melted materials. Insufficient cooling time due to high printing speeds may also result in slow solidification and thus cause deformation and/or collapse of printed structures. Prolonged cooling and low printing temperatures can cause poor fusion of the

subsequent layers and severe surface roughness of the printed foods. In practice, a temperature sweep using oscillatory rheometry and/or a heat flow scan based on differential scanning calorimetry are often performed to identify the gelation/crystallization temperature of food materials. This can serve as a reference when determining the printing temperature of a given food material. For example, Schutyser et al. (2018) suggested that the printing temperature be 5 to 15 °C above the printing material's gelation temperature. However, HE-3DFP is a dynamic process: the extruded food materials are cooled much faster than in standard analytical tests (typically less than 2°C/min) can achieve, which may influence the rheological response of the material. Rheological and thermal measurements can therefore only provide an indication of the material behavior during printing, which can help to narrow down the trial-and-error experimental window rather than describe the true physical changes during printing (Liu et al., 2019). In addition, because most of the hot-extrusion food printers are equipped with a barrel heater but not with a nozzle heater, there is often no consistent temperature control during the printing process, which further contributes to the dynamic nature of the HE-3DFP.

To study the dynamics of 3D printing, for thermoplastic printing applications, numerical simulations have been done to characterize the heat transfer and material properties during 3D printing. The dynamic solidification process was fully described based on heat transfer models and the properties of one thermoplastic material (Xia et al., 2018). However, the complexity of food materials with its multiphase and multi-ingredient nature makes it challenging to follow a similar numerical modelling approach. Alternative to full simulation, infrared (IR) thermography has been used to monitor the temperature changes during the dynamic cooling process of HE-3DFP. Rando & Ramaioli (2021) recorded thermal videos to characterize the HE-3DFP of chocolate. The authors measured the material temperature just before collapsing as influenced by the printing temperatures, ambient temperatures, and printing speeds. The study concluded that thermographic analysis can provide detailed insights of the dynamic cooling process and guide the optimization of parameters for 3D printing of chocolate.

Other than chocolate, many other thermoreversible food materials can be printed using HE-3DFP. Most of these foods behave as viscoelastic solids at room temperature, and can be roughly categorized as cross-linked hydrogels or jammed dispersions based on their

solidification mechanisms. While solidified chocolate exhibits crystallinity with minimal viscoelasticity, the deformation of viscoelastic solid foods are subjective to both temperature (liquification) and time (creep), especially after the HE-3DFP process. The dynamic cooling process of thermoreversible food materials is not yet fully elucidated during HE-3DFP. This study aims to conduct thermographic analysis to simultaneously characterize the material cooling and deformation of thermoreversible food materials. We printed cross-linked hydrogels and jammed dispersions to explore the structural deformation that is driven by the combination of material properties, temperature, and printing time. The thermographic observations were combined with rheological measurements to understand material behaviors and provide optimization guidance for adjusting food formulations and printing parameters.

5.2. Materials and methods

5.2.1. Printing materials

Three thermoreversible food materials were selected for the HE-3DFP experiments.

(1) A κ-carrageenan-gelatin blend was prepared by first dissolving 2 % (w/w) κ-carrageenan (Sigma Aldrich, Darmstadt, Germany) in deionized water at 80 °C for 30 min. The solution was then cooled to 60 °C and mixed with 5% (w/w) gelatin (bovine skin, type B, Sigma Aldrich, Darmstadt, Germany) for 30 min. The κ-carrageenan-gelatin blend was cooled to 20 °C and stored at 4 °C for further use.

(2) A concentrated sodium caseinate dispersion (48%, w/w, FrieslandCampina, Wageningen, the Netherlands) was heated to 80 °C for 10 min in a water bath and diluted with deionized water to obtain a final concentration of 30% (w/w).

(3) Commercial processed cheese (ERU, the Netherlands) was purchased from a local supermarket (Albert Heijn, the Netherlands) and used as the third printing material for the subsequent experiments.

5.2.2. Rheological measurements

5.2.2.1. Small amplitude temperature sweep

To characterize the gelation temperature of the materials, temperature sweeps were conducted using a rheometer with a cone-plate geometry (⌀ = 20 mm; θ = 2˚, Anton Paar Physica MCR502, Graz, Austria). A cooling ramp was employed to characterize the gelation process of the printing materials. Materials were first melted at 70 °C for 5 min and then transferred onto the preheated plate at 60 °C. The cone probe was lowered, excessive materials was carefully removed, and the rim of the cone was coated with high viscosity paraffin oil to prevent water evaporation. Based on preliminary strain-sweep experiments, the shear strain and frequency were set to 1% and 1 Hz, respectively, to ensure that measurements were collected within the linear-viscoelastic regime. The cooling ramp was set to decrease from 60 °C to 25 °C at a rate of 2 °C/min. The corresponding storage modulus (G′) and loss modulus (G″) were recorded during the cooling ramp, and the gelation temperature was taken at the temperature when the G′ exceeded the G". The complex viscosity (η^*) was calculated based on Eq. 1 to evaluate the consistency of the material during the cooling ramp.

$$\eta^* = \sqrt{\left(\frac{G'}{\omega}\right)^2 + \left(\frac{G''}{\omega}\right)^2} \qquad \text{Eq. 1}$$

Where ω is the angular frequency in rad/s.

5.2.2.2. Creep tests and Time-Temperature Superposition (TTS)

Creep tests were conducted using the same rheometer set up introduced in section 2.2.1. A shear stress of 5 Pa was applied to each material for 5 min at a temperature range from 20 to 50 °C with 5 °C intervals. At the selected measuring temperature, the material was tempered for at least 10 min before the creep test started. The corresponding creep compliance (J) was recorded over time (t) and fitted to a 4-element Burgers model (Eq. 2).

$$J_{(t)} = J_0 + J_1\left(1 - e^{\left(\frac{-t}{\lambda_{ret}}\right)}\right) + \frac{t}{\mu_0} \qquad \text{Eq. 2}$$

where J_0 is the instantaneous elastic compliance; μ_0 is the zero-shear viscosity; J_1 is the compliance associated with the Kelvin–Voigt element; λ_{ret} is the retardation time associated with the Kelvin–Voigt element.

To combine the time and temperature impacts of material creep, the TTS principle was used to describe printing material creep at short and long observation times (Udyarajan et al., 2007). Though originally designed to study amorphous polymers, the TTS principle has been extended to characterize crystalline and cross-linked food materials, which are similar to the printing materials featured in this study (Ahmed, 2017). Specifically, for each printing material, the creep data obtained at different temperatures were shifted horizontally using the Williams-Landel-Ferry (WLF) model (Eq. 3) to construct the TTS master curve:

$$\log(a_T) = \frac{-C_1(T - T_r)}{C_2 + (T - T_r)} \quad \text{Eq. 3}$$

Where a_T is the shift factor, T_r is the reference temperature, C_1 and C_2 are the shifting constants. In this study, a reference temperature of 25 °C was selected to apply a typical ambient temperature used during 3D food printing. C_1 and C_2 were iteratively fitted by minimizing the sum of square error between the Burgers model fit at reference temperature to the shifted observations.

5.2.3. Hot-extrusion 3D food printing

Hot-extrusion 3D food printing was conducted using an in-house modified pneumatic 3d printing system (DR-2203, Nordson EFD, USA) (Schutyser et al., 2018). About 20 g of printing material were liquified by heating at 70 °C for 5 min, carefully loaded into a printing syringe, and connected to a fixed nozzle size of 0.84 mm. The syringe was tempered at printing temperatures between 55 and 60 °C for 10 min prior to printing. The syringe temperature of each printing material was determined based on its gelation temperature obtained from the temperature sweep measurement. A printing pressure was empirically adjusted for each material to ensure proper extrudability (minimal over and under extrusion) and used throughout all printing experiments to ensure consistent extrusion rates. A 10-layer and 80-mm long wall structure was printed onto a room-temperature (~20 °C) platform to examine the printing stability. For all printed structures, the cooling time between two layers was set to 5, 10, and 15 s, respectively by varying the printing speed. A

layer height of 0.8 mm was used throughout all printing experiments. Duplicate printing experiments were conducted for each material, and averaged measurements were reported in the results section.

5.2.4. IR thermography

During the 3D printing experiments, variations of printing parameters led to differences in terms of structural stabilities (Figure 5.1A and B). To understand structure deformation, a thermal camera equipped with a zoom lens (Optris PI 640, Berlin, Germany) was placed on the side-view position to capture the temperature change of the extrusion nozzle and the top-layer temperature of the printed structure (Figure 5.1C). Thermal videos were recorded at 640 x 480 pixel resolution with a frame rate of 10 Hz. For each layer of printing, the temperature of the material just after extrusion (i.e. the material temperature at the printing nozzle) and the top-layer temperature of the printed structure were recorded at a constant position per printing layer to characterize the heat transfer during printing. The thermal video frames were scaled using the outer diameter of the printing nozzle as a reference distance. The cumulative deformation of the printed structure was determined by measuring the distance between the extrusion nozzle to the top layer ($D_{N\text{-}L}$) at the center of each layer. With no deformation, the $D_{N\text{-}L}$ should be equal to the layer height (H) that was set in the printing path (Figure 5.1D). However, deformation occurs when the $D_{N\text{-}L}$ exceeds the H, indicating that the printed layers have deformed from the intended height based on the digital design (Figure 5.1E). The cumulative deformation of each layer ($\varepsilon_{(n)}$) was calculated using Eq. 3 to understand the material deformation during HE-3DFP. The temperature and deformation measurements were collected using the PIX connect software made by Optris (Berlin, Germany).

$$\varepsilon_{(n)} = \frac{(D_{N-L}-H)}{(H\times n)} \cdot 100\% \qquad \text{Eq. 3}$$

where n is the layer number. Based on Eq. 3, it is possible for $\varepsilon_{(n)}$ to be negative, indicating that the observed distance is less than the layer height (this may occur due to over-extrusion).

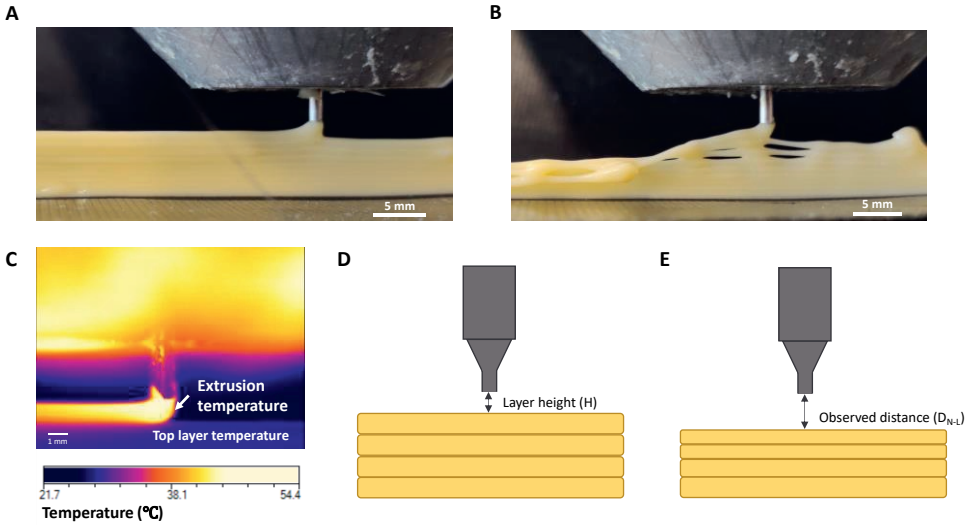

Figure 5.1. A: Example printing of a processed cheese structure with no deformation. B: Example printing of a deformed process cheese structure. C: screenshot of an example thermal video highlighting the extrusion temperature at printing nozzle and the top layer temperature right below the printing layer. D: Schematic drawing of a printed structure with no deformation. E: Schematic drawing of a deformed structure.

5.3. Results & Discussion

5.3.1. Material gelation process

Although all 3 materials exhibit thermoreversibility and have been used for 3D food printing applications in previous studies, their sol-gel transition mechanisms vary largely due to compositional and microstructural differences. Figure 5.2 highlights the material phase transition from the liquid-like to the solid-like state obtained from the temperature sweep measurement. At 60 ℃, the complex viscosity of the κ-carrageenan-gelatin blend was ~ 2 Pa·s, suggesting it behaved as a very thin liquid (Figure 5.2A). The gelation temperature of the κ-carrageenan-gelatin blend was measured to be 52 ℃, as indicated by a rapid increase of complex viscosity and the G′ exceeding the G″ (Figure 5.2D). Upon further cooling, from 52 to 40 ℃, the complex viscosity sharply increased from ~ 5 Pa·s to ~ 2000 Pa·s, and the G′ and G″ sharply increased from ~ 30 Pa to ~ 20000 Pa and ~ 3000 Pa, respectively. During this cooling period, the random coiled gelatin transforms into triple-helical structures to create crosslinks. In the meantime, the linearly aligned κ-carrageenan start to form helices that reduce the mobility of the liquid solution (Burey et al., 2008). Considering the κ-

carrageenan-gelatin interactions, several studies reported that the addition of κ-carrageenan led to an increase of the gelation temperature and gel strength compared to pure gelatin systems (Derkach et al., 2015; Pranoto et al., 2007). The increased gelation temperature can be explained by the polyelectrolytic complexes formed between the cationic domain of gelatin and the anionic domain of κ-carrageenan (Derkach et al., 2015). The sharp sol-gel transition allows quick liquifying and solidification of the κ-carrageenan-gelatin blend, making it suitable for printing stable food structures using the hot-extrusion printing mechanism.

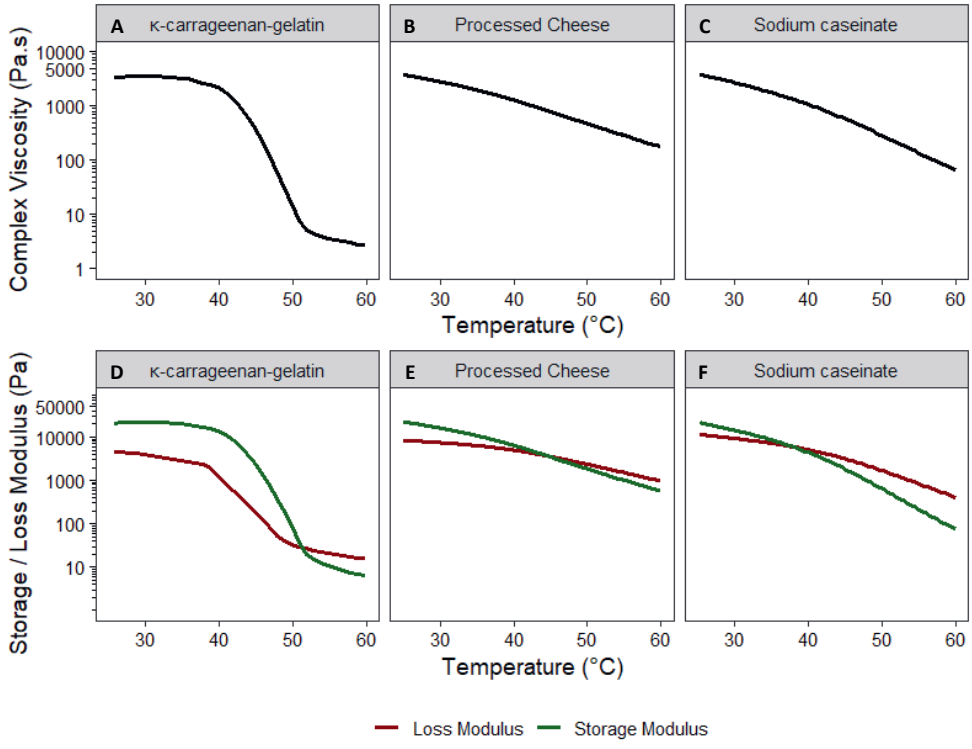

Figure 5.2. Complex viscosity change from 60 to 25 ℃: κ-carrageenan-gelatin blend (A), processed cheese (B), and sodium caseinate (C). Temperature sweeps of κ-carrageenan-gelatin blend (D), processed cheese (E), and sodium caseinate (F). Cooling ramp = 2 ℃/min; angular frequency = 1 Hz.

In the same cooling range, the processed cheese exhibits a different rheological profile (Figure 5.2B and E). At 60 ℃, the melted processed cheese was a viscous liquid with a complex viscosity of ~ 100 Pa·s. The sol-gel transition occurred much more gradually compared to the κ-carrageenan-gelatin blend as the G′ at gelation temperature (45 ℃) was already ~ 5000 Pa. This gradual sol-gel transition of the processed cheese can be explained

by its solidification mechanism. At elevated temperatures, processed cheese melts to a liquid-like state due to the weakening of the casein-casein interactions. The melting of fat crystals in processed cheese also contributes to the liquid nature above 40 ℃ (Kapoor and Metzger, 2008; Lucey et al., 2003). Emulsifying salts remove physical crosslinks due to calcium phosphate crystals and the processed cheese appears as a stabilized liquid-in-liquid emulsion (Le Tohic et al., 2018). Upon cooling, the melted fats slowly crystalize and the casein-casein interaction strengthens to form solid cheese again. The fat crystallization and casein rearrangement may take more time compared to the cross-linked gelatin and κ-carrageenan, which can also explain the more gradual increase of G′ observed in Figure 5.2E. At 25 ℃, the processed cheese solidifies to a strong gel with a G′ greater than 10000 Pa, making it suitable for HE-3DFP (Ross et al., 2021).

Figure 5.2C and F show the complex viscosity and moduli changes during the temperature sweep of the concentrated sodium caseinate dispersion (30%, w/w). Just like the processed cheese, a gradual increase of the complex viscosity and moduli was observed as the dispersion was cooled from 60 to 25 ℃. The G′ at the gelation temperature (37 ℃) was ~ 7000 Pa, much higher than with the κ-carrageenan-gelatin blend. During cooling, the sodium caseinate dispersion gradually gains elasticity due to the increase of interchain interactions of the casein molecules at lower temperature, which leads to a larger effective volume fraction of the casein particles and enhances the jamming of the casein micelles (Loveday et al., 2010). However, even though the sodium caseinate dispersion showed was solid-like in a standard temperature sweep (as observed in our study), several studies did suggest that the classification as a "gel-like structure" was mistaken due to its high viscosity and rheological measurements with a short relaxation time (Raak et al., 2020; Thomar et al., 2013). The authors suggested that concentrated sodium caseinate dispersions still behaved as viscous liquids given enough relaxation time. Therefore, the long-term stability of sodium caseinate-based printed foods may be impacted due to its viscous liquid properties. In 3D food printing applications, both highly viscous liquids and elastic gels were successfully printed, so this study focuses on evaluating the stability of the sodium caseinate immediately after hot-extrusion. Despite the similar cold-solidifying properties, the 3 materials showed different solidification mechanisms, which can impact the printing stability of final structures.

With these mechanisms in mind, we subsequently conducted thermographic characterizations of the material cooling and structural deformation during HE-3DFP.

5.3.2. Thermographic analysis during 3D food printing

IR thermography was used to characterize the extrusion temperature during printing (i.e. the temperature of the material as it is being extruded from the printing nozzle) to better understand the behavior and state of the printing materials. The temperature monitoring at the nozzle can elucidate the proper material extrudability, which is the first necessary step towards a successfully printed structure (Liu et al., 2019). In Figure 5.3, the extrusion temperature at nozzle was measured per printing layer for the three printing materials at cooling times of 5, 10, and 15 s, respectively. The syringe temperature was set at 55 °C for the κ-carrageenan-gelatin blend (Figure 5.3A). Based on the thermographic measurement, the extrusion temperature per layer ranged from 38 to 43 °C. All observed extrusion temperatures at the nozzle were lower than the borrel heater temperature that was set for the syringe. Because the nozzle was in contact with the ambient environment, the printing material cooled in the nozzle before extrusion. The material temperature initially decreased in the nozzle during extrusion as compared to the set syringe temperature, but this decrease became less as the printing progressed. This is mostly likely because the nozzle got heated by the previously extruded hot material (Figure 5.3A). Because the later-printed layers were hotter than the earlier printed layers, ideally, the cooling time should be increased as the printing progresses to allow sufficient solidification for each printed layer.

Because the same 3D printer was used in all printing experiments, this transient heat effect in the nozzle was also observed for the other two materials (Figure 5.3B and C). Rando & Ramaioli (2021) also captured this effect in a study where thermographic analysis was applied to monitor chocolate printing. Without a dedicated nozzle heater, cooling in the nozzle is likely to occur and affect the HE-3DFP process. Therefore, we suggest to monitor the extrusion temperature close to the nozzle (Figure 5.1A) to best determine the state of the printing materials and their structural stability rather than simply referring to the syringe barrel temperature.

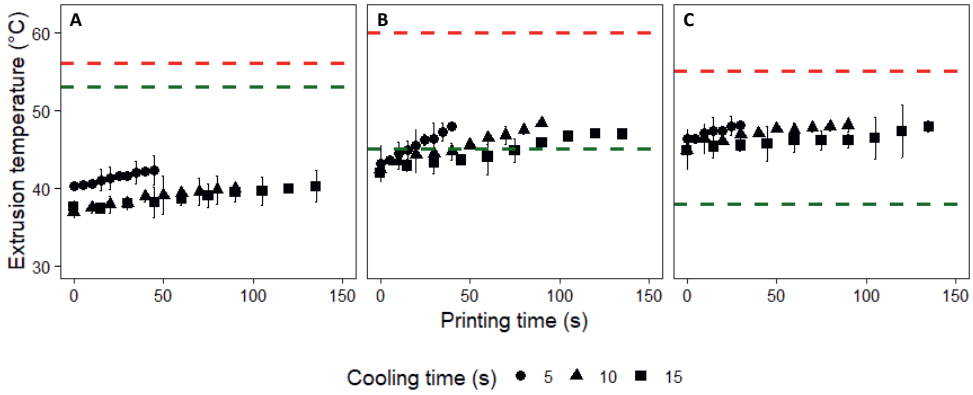

Figure 5.3. Extrusion temperature at nozzle change over printing time (one measurement was taken per printing layer). A: κ-carrageenan-gelatin blend. B: processed cheese. C: sodium caseinate. The red dashed line represents the syringe barrel temperature. The green dashed line represents the gelation temperature obtained from the temperature sweep measurements.

For all three materials, the syringe temperature was set higher than the measured gelation temperature, to ensure a proper liquification of the material inside the syringe. However, when comparing the extrusion temperatures to the gelation temperatures, the three materials were extruded at different physical states. The κ-carrageenan-gelatin blend was extruded between 38 and 43 °C, which was below its gelation temperature (52 °C) based on the rheological measurement (Figure 5.2). The extruded filament should already have been in the solid-like state due to the cooling of the material through the cold printing nozzle. However, the shear in the nozzle prevented further gelation and temporarily reduced its storage modulus. At the same time, the cooling of the material results in an increase of the viscosity to reach a minimum of 1000 Pa·s. This higher viscosity improved the overall extrudability of the material, which may be necessary with cross-linked hydrogels with such an abrupt change in states. During preliminary experiments, we failed to print the κ-carrageenan-gelatin blend at higher syringe temperatures due to the spreading and spraying of the liquid material on the platform. A similar observation was made by Vadodaria et al. (2021) as the authors stated that high printing temperatures (syringe temperatures) led to fast spreading of hydrogel-based printing materials. Due to the sharp sol-gel transition of the κ-carrageenan-gelatin blend (Figure 5.2A), a slight overheating leads to rapid decrease in viscosity. Since the hydrogel material is shear-thinning, extruding a thin liquid under pressure then results in spraying and rapid spreading of the printing material.

In Figure 5.3B, the processed cheese was extruded between 40 and 47 °C across the 3 cooling times. The gelation temperature of the processed cheese was 45 °C, indicating that the material was extruded close to the sol-gel transition temperature zone (Figure 5.2B). The complex viscosity of the processed cheese between 40 and 47 °C ranged from 600 to 1000 Pa·s. Since the transition is quite gradual, the processed cheese retained high complex viscosity which ensured the consistency of the extruded filament. Based on our previous study (Ma et al., 2021), the processed cheese has a flow index around 0.5, which makes it less shear-thinning than the κ-carrageenan-gelatin blend. The high viscosity and the good consistency upon extrusion made it possible to print processed cheese at a wide range of printing temperatures between 40 to 75 °C (Le Tohic et al., 2018; Ross et al., 2021). This large operation window makes it robust for printing and reduces the number of the trial-and-error experiments in the preparation phase of printing processed cheese. In Figure 5.3C, the sodium caseinate dispersion was extruded between 45 to 48 °C, which was above its gelation temperature as a viscous liquid. However, due to a similar gradual sol-gel transition as the processed cheese, the extruded material retained a complex viscosity of 500 Pa·s or above, again offering the necessary material consistency to properly form extruded filaments (Figure 5.2C). In another study, Schutyser et al. (2018) reported the optimal syringe temperature to be 5- 15 °C above its gelation temperature when printing concentrated sodium caseinate dispersion. The authors suggested that liquid-like characteristics of sodium caseinate were necessary for its proper extrudability, which was in agreement with results presented in this study.

Based on our observations, even though materials were heated above the gelation temperatures in the syringe, the actual extrusion temperature of the material was lower due to the lack of nozzle heating, which altered the properties of the material just before extrusion. Whether the materials were still liquid or already started to solidify, all of them had high enough complex viscosity around 600 Pa·s to achieve the proper consistency just before extrusion (Figure 5.2). In previous studies, the extrudability of the printing materials were explained in terms of viscosity and shear-thinning properties (Liu et al.,2019; Ma et al., 2021). Specifically for HE-3DFP, the extrusion temperature directly impacts the material's viscosity and shear-thinning properties. In this study, for cross-linked hydrogel materials such as the κ-carrageenan-gelatin blend, some supercooling (i.e. the material remains

liquified below the gelation temperature) ensures an increase of complex viscosity. Therefore, to successfully print hydrogel materials, the syringe temperature should be set just above the gelation temperature. By nozzle cooling, the hydrogels can gain viscosity upon cooling at the nozzle, which eventually contributes to the proper extrudability during printing. The sol-gel transition of jammed dispersions (processed cheese and sodium caseinate) is more gradual compared to hydrogel based materials. Therefore, a wider range of syringe temperatures can be applied to print such materials, reducing the sensitivity of optimizing the syringe temperatures in the pre-printing phase. However, in all systems, low syringe temperatures (i.e. below the gelation temperature) result in rapid material solidification. The rapidly solidified materials can lead to insufficient layer fusions and surface roughness of the filaments, which are undesirable for the final printing quality (Rando and Ramaioli, 2021; Vadodaria et al., 2021). From our thermographic observations, for 3D food printers without a nozzle heater and without active cooling of the printing platform, we suggest to set the syringe heater temperature just above a material's gelation temperature to ensure proper fusion and consistency of the extruded filaments.

5.3.3. Deformation of hot-extrusion printed structures

From the sideview of the thermal videos, we can sometimes observe deformation of the printed structures during printing. This section therefore discusses changes of the top-layer temperatures and the per-layer deformation of the printed structure during HE-3DFP. The temperature and deformation observations were evaluated and linked to the temperature-driven and time-driven deformations based on the material properties (cross-linked hydrogel vs. jammed dispersions).

5.3.3.1. Deformation of 3D-printed κ-carrageenan-gelatin blend

Figure 5.4A highlights the cumulative deformation observed during printing the κ-carrageenan-gelatin blend with 5, 10, and 15 s of cooling intervals between printing different layers. With 5 s cooling per layer, the top layer temperature of the κ-carrageenan-gelatin blend ranged between 34 to 36 °C. The 5-s cooled structure started to deform from the 3rd layer (after 15 s of printing), and layer deformation then proceeded throughout the entire subsequent printing process, with the final cumulative deformation reaching 37%. For the printed structures with 10 and 15 s cooling per layer, the top-layer temperatures were between 30 and 33 °C. With longer cooling times and lower top-layer temperatures, less

than 5% of final cumulative deformation was observed. The small deformation indicated the gelation of κ-carrageenan-gelatin to form stable structures. An increase of cooling time from 10 to 15 s per layer did not further impact the structural deformation, suggesting that the layers could achieve sufficient solidification during the intervals, and time-driven deformation (i.e. creep) during printing was mostly inhibited. A temperature difference of 3 to 4 °C was observed between the deformed (5-s cooled) and the stable (10-s & 15-s cooled) structures. Due to the sharp sol-gel transition of the κ-carrageenan-gelatin blend, a small top-layer temperature difference results in large rheological changes. The difference in the top-layer temperature and the printing stability suggests that a critical top-layer temperature of ~33 °C can be used as an indicator for ensuring printing stability of the κ-carrageenan-gelatin blend. The higher top-layer temperature of the 5-s cooled structure indicated insufficient cooling of the printed layers. Our observations show that the deformation of κ-carrageenan-gelatin blend was caused by the higher material temperature and insufficient gelling. No deformation was observed if the material is cooled below a critical temperature (~ 33 °C) by increasing the cooling time, suggesting that no creep occurred during the printing process.

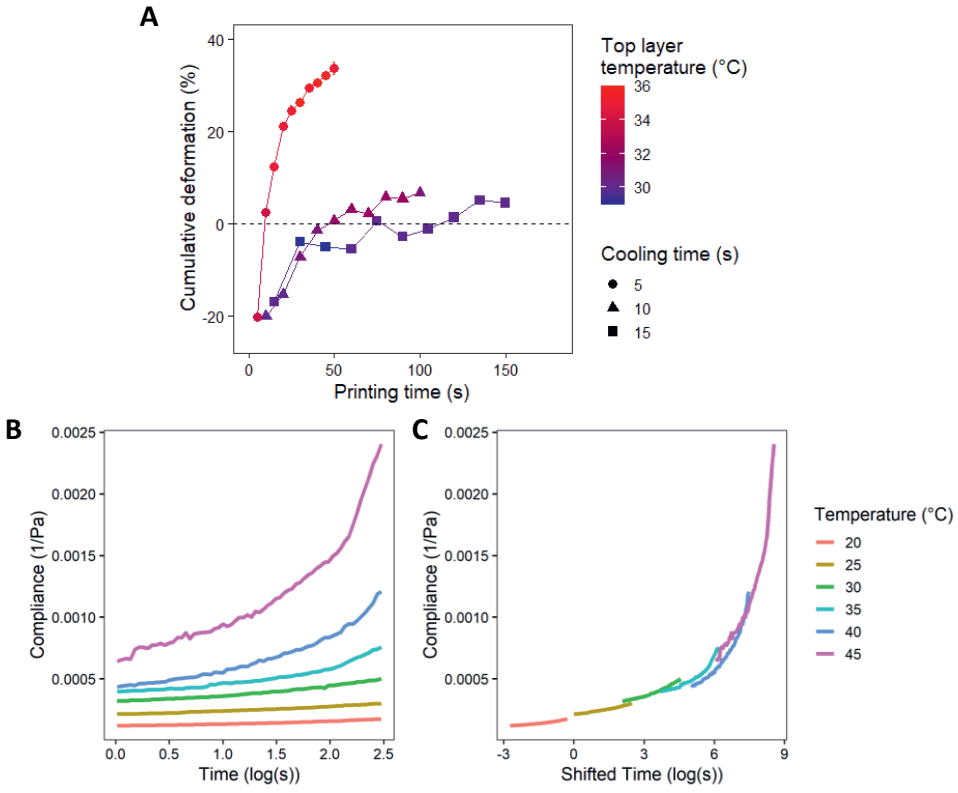

Figure 5.4. Deformation characterization of κ-carrageenan-gelatin blend. A: Per-layer cumulative deformation change over printing time. A negative cumulative deformation indicates over-extrusion of the layer. B: Creep compliance measurement between 20 to 45 ℃. C: time-temperature superposition master curve of creep compliance.

To support the observations from thermal videos, creep measurements of the κ-carrageenan-gelatin blend were performed at different temperatures. In Figure 5.4B, we observed a typical viscoelastic creep behavior which can be described by the 4-element Burgers model (Eq. 2). At the beginning of the creep test, an instantaneous elastic compliance appears, followed by the viscoelastic creep behavior as described by the Kelvin–Voigt element. The detailed Burgers model fits of the creep compliance can be found in Table 5.1. As the temperature increases from 20 to 45 ℃, the zero-shear viscosity decreased and the material crept more during the 300 s measurement. To further evaluate the combined time and temperature effects, Figure 5.4C shows the time-temperature superposition of the creep master curve of the κ-carrageenan-gelatin blend. With a

reference temperature of 25 °C, the creep compliance master curve follows the same behavior as observed from the single-temperature measurements. The range of the shifted times in Figure 5.4C suggests a very slow creep behavior of the κ-carrageenan-gelatin blend. At 25 °C, it requires 1 x 10^9 s to obtain a neglectable amount of creep, making time-driven deformation irrelevant in the context of assessing the 3D printing stability of κ-carrageenan-gelatin blend.

Primarily, the cause of deformation for the κ-carrageenan-gelatin blend was insufficient gelling caused by high material temperature, as observed from Figure 5.4A. Similar cross-linked hydrogels were frequently studied in other 3D food and bio- printing studies. For example, Liu et al. (2019) suggested that a temperature sweep can serve as an indicator to determine the self-supporting ability of a carrageenan-xanthan-starch complex. With the printing material sufficiently cooled, the increase of G′ will lead to a stable printed structure. Other than temperature sweeps, the development of a yield stress is also frequently indicated as a structural stability indicator in other studies (Wilms et al., 2021; Zeng et al., 2021). Our rheological measurements were conducted under steady state, which ignores the fact that the cooling of extruded materials is quite sudden. From thermal imaging, we observe that the initial cooling rates as materials were extruded range from 1 to 3 °C/s, which allows a very rapid intermolecular association of the helical gelatin and κ-carrageenan (Berghmans et al., 1994). The dynamic cooling process leads to a fast gelation driven by the temperature equilibrium. In our study, observing the top-layer temperature provides snapshots of the dynamic cooling process. We can then derive the critical temperature as an indicator to determine the structural stability of the κ-carrageenan-gelatin blend. The direct temperature monitoring using IR camera can be a complementary method to the steady-state rheological measurements to guide HE-3DFP of hydrogels.

5.3.3.2. Deformation of 3D-printed processed cheese

While the material temperature primarily determines the structural stability of hydrogels, there are also other types of food systems (e.g. jammed dispersions) that may have different dependence on the dynamics. Figure 5.5A shows the printing time vs the cumulative deformation of processed cheese printed with 5, 10, and 15 s cooling time per layer. The least-cooled structure (5 s) had the highest top-layer temperature between 33 and 34 °C, compared to the longer-cooled structures (10 and 15 s). With a higher top-layer

temperature, the printed processed cheese started to deform after 6 layers of extrusion. The deformation continued until the end of the printing process with a final 19% cumulative deformation relative to the designed height. For the longer-cooled structures, less than 3% of deformation was observed, Again, the cumulative deformation remained similar at longer cooling intervals, even though increasing the cooling time from 10 to 15 s did further decrease the top-layer temperature. The similar deformation patterns for the 10 and 15 s cooled structure again suggest that the deformation during printing is driven by insufficient cooling, rather than the prolonged printing time. A critical top-layer temperature of 33°C was found from the thermographic observations, providing an indicator that can determine the structural stability of printed processed cheese.

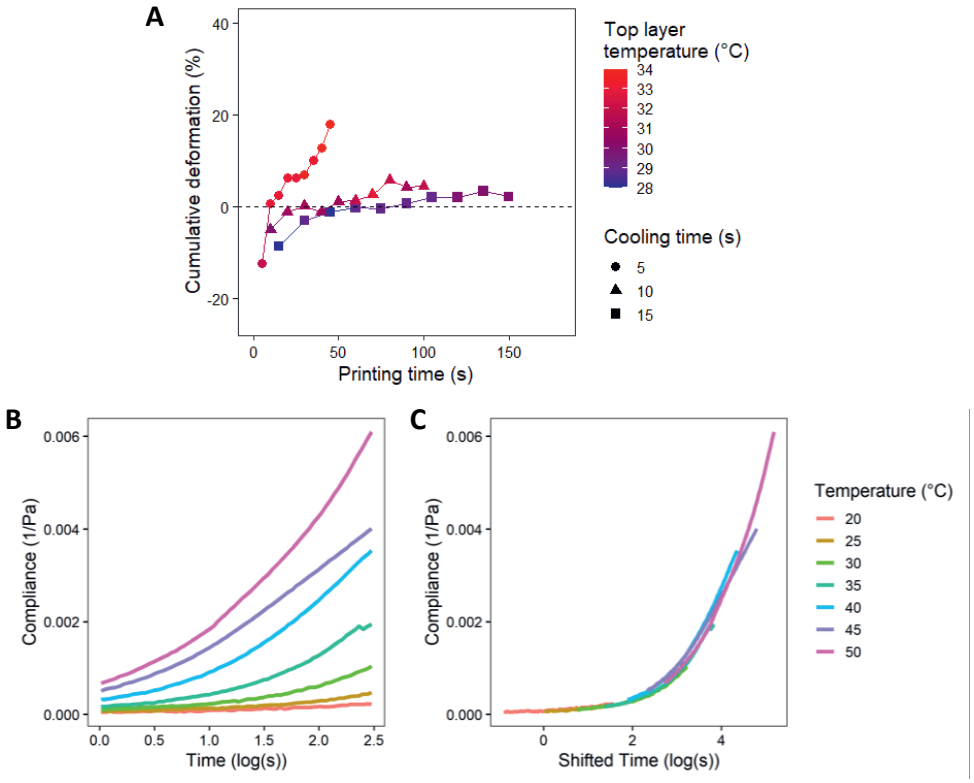

Figure 5.5. Deformation characterizations of processed cheese. A: Per-layer cumulative deformation change over printing time. A negative cumulative deformation indicates over-extrusion of the layer. B: Creep compliance measurement between 20 to 50 ℃. C: time-temperature superposition master curve of creep compliance.

The creep measurements from 20 to 50 °C are shown in Figure 5.5B. The creep behavior of processed cheese fits well with the Burgers model (Table 5.1). The increase of the temperature reduces the zero-shear viscosity of processed cheese, which is in agreement with previous studies (Kuo et al., 2000; Sharma et al., 2017). The creep master curve yields the time and temperature dependance of processed cheese's deformation behavior (Figure 5.5C). Compared to the κ-carrageenan-gelatin blend, the creep master curve shows that, at 25 °C, the processed cheese may exhibit some deformation (up to 0.006 1/Pa) in the time frame of 1 x 10^4 s. The jamming of casein particles and fat crystallizations may take longer to occur, which make the material prone to gravitation-driven flow over time. This creep time frame is still longer than the required printing time for a typical food structure. However, the creep time range is already relevant to sample storage and producing complex food structures with long printing times. Therefore, even though the time-driven deformation was not impacting the immediate printing stability (which was driven by material temperature), storage time and consumption time should be considered for the entire product lifecycle of printed processed cheese.

Table 5.1. Fitted parameters obtained from the 4-element Burgers model. J_0 is the instantaneous elastic compliance. μ_0 is the zero-shear viscosity. J_1 is the compliance associated with the Kelvin–Voigt element. λ_{ret} is the retardation time associated with the Kelvin–Voigt element. R^2 is the coefficient of determination between the fitted and measured values.

Materials	Temperature (°C)	$J_0 \cdot 10^{-4}$ (Pa^{-1})	$\mu_0 \cdot 10^5$ (Pa s)	$J_1 \cdot 10^{-4}$ (Pa^{-1})	λ_{ret} (s)	R^2
Processed Cheese	20	0.36	24	0.8	12.6	0.965
	25	0.46	9.5	1.3	10.5	0.989
	30	0.70	4.2	2.9	18.2	0.993
	35	1.2	2.6	8.0	28.4	0.992
	40	1.8	1.7	15	21.8	0.995
	45	2.9	1.6	21	14.0	0.992
	50	3.6	0.87	26	13.1	0.993
Sodium Caseinate (30%)	20	0.32	2.5	1.8	13.9	0.999
	25	0.59	0.82	3.2	17.0	0.999
	30	0.97	0.21	5.9	19.4	1.000
	35	1.9	0.055	11	29.0	1.000
κ-carrageenan-Gelatin	20	1.2	88	0.27	13.5	0.970
	25	2.1	58	0.46	10.0	0.985
	30	3.1	28	0.88	16.0	0.988
	35	3.9	10	0.96	10.3	0.996
	40	4.8	5.3	2.1	11.8	0.992
	45	6.1	2.1	3.8	7.03	0.995

5.3.3.3. Deformation of 3D-printed sodium caseinate dispersion

While the deformation of κ-carrageenan-gelatin blend and processed cheese was driven by high material temperatures during printing, the observations made with the sodium caseinate dispersion appeared to show a different trend. Figure 5.6A shows the cumulative deformation over printing time for the structures cooled with 5, 10, and 15 s per layer. All 3 structures started to deform from the first layer, and regardless the cooling times, more than 20% of cumulative deformation were observed for the finished structures. Even with lower top-layer temperatures, the structures with longer cooling time (10 and 15 s per layer) still deformed to a similar degree (~ 20%), suggesting that the deformation of printed sodium caseinate dispersion was driven by both time and temperature, instead of only temperature.

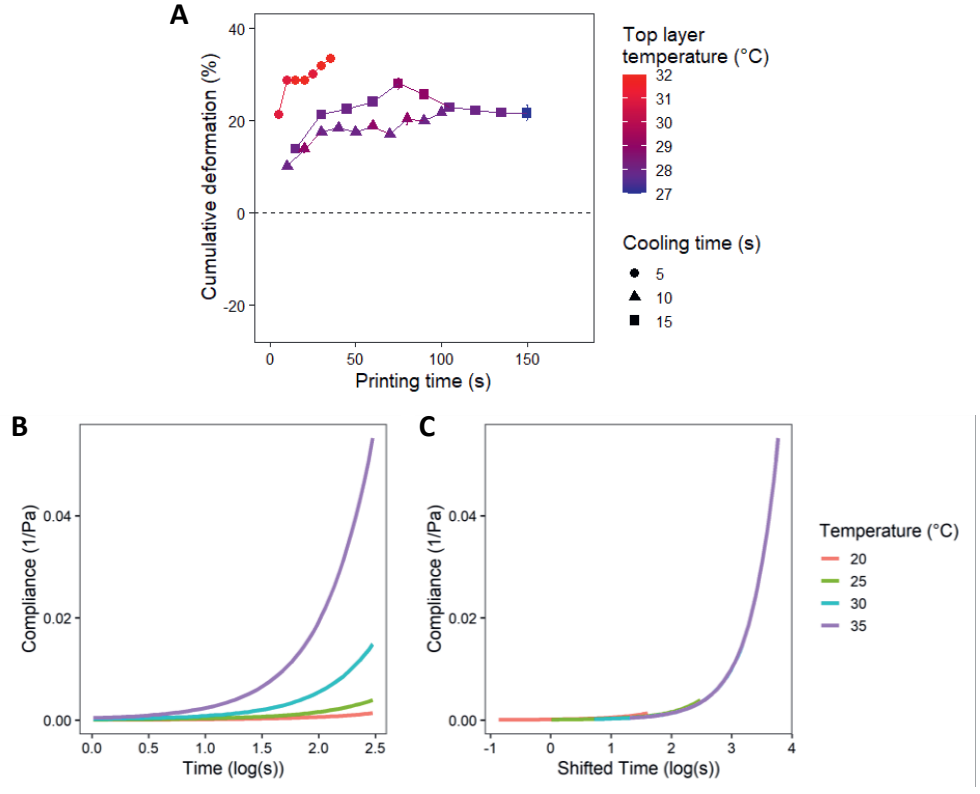

Figure 5.6. Deformation characterizations of sodium caseinate (30% w/w). A: Per-layer cumulative deformation change over printing time. A negative cumulative deformation indicates over-extrusion of the layer. B: Creep compliance measurement between 20 to 35 ℃. C: time-temperature superposition master curve of creep compliance.

The thermographic observations shown in Figure 5.6A were supported by the creep results in Figure 5.6B and C. As shown in Figure 5.6B, the creep compliance was much greater than with the κ-carrageenan-gelatin blend and the processed cheese (Figures 5.4B and 5.5B). At 35 °C, the creep compliance after 300 s already exceeds 0.05 1/Pa, indicating probable deformation during printing. The deformations at higher temperature were further connected with time effects by creating the creep master curve (Figure 5.6C). Even with just 1000 s, at 25 °C, the creep of the sodium caseinate dispersion can get up to 0.01 1/Pa. The creep master curve suggests that shortly after printing, even when the printed material is cooled close to room temperature, there can still be some material deformation of the final printed structure. Meanwhile, the good agreement between the experimental data and the Burgers model (as indicated by the high R^2) indicates a classical viscoelastic creep behavior of sodium caseinate dispersion (Table 5.1). Our results are in agreement with the conclusion by Loveday et al. (2010), suggesting that sodium caseinate dispersions behave as a viscoelastic liquid, without crosslinked gel structure. This is in contrast to the behavior of processed cheese which may draw solidity from jammed fat crystals and perhaps the micellar structure of the caseins. Therefore, printing of pure sodium caseinate (or another similar jammed dispersion) has intrinsic material limitations, resulting in collapsed and spreading of the printed structure over time. The time-driven deformation of sodium caseinate is more difficult to control than the cause of high material temperatures observed from Figures 5.4 and 5.5. Some elasticity is needed in printing materials to ensure the material is free from time-dependent deformation during and after printing. Therefore, pure sodium caseinate dispersions are an extreme example demonstrating the undesirable results of printing viscoelastic materials using HE-3DFP. Improved printability was developed by Schutyser et al. (2018) by incorporating pectin into the sodium caseinate dispersions, which increases the overall elasticity of the printing material.

5.3.4. General discussions and recommendations

Thermographic analysis provides real-time observation of material cooling and deformation during HE-3DFP. This study provides direct experimental support to quantitatively evaluate materials' printing behaviors that could not be easily derived from rheological measurements alone. While the thermographic and rheological measurements complement each other, they have different purposes in relation to 3D food printing. Rheological measurements are crucial for understanding the material's properties and connecting food ingredient

functionality to food ink formulations (Liu et al., 2019; Ma and Zhang, 2022). However, standard rheological measurements are limited to off-line instrumentations and can only provide information about the material at steady state, which cannot fully represent the dynamic material behavior during HE-3DFP, where several simultaneous changes occur. An implementation of a nozzle heater can offer a better control of heat transfer during extrusion, which may lead to an more accurate estimation of material properties based on off-line rheological measurements.

Thermographic imaging is an non-destructive and in-situ measurement, which provides direct monitoring during HE-3DFP. Real-time temperature and deformation measurements may be integrated as a part of the printer control system to guide printing parameters for more accurate printing results. For example, if the thermal imaging indicates that the deformation exceeds a threshold, a feedback loop control could slow or pause the printing to reduce the material temperature before printing the subsequent layers. Alternatively, active cooling such as convection air from a fan of the printed structure can also be added to the printer set up. The convection cooling can reduce the temperature of the printed structure without compensating the printing speed, which can subsequently improve the printing efficiency, although the active cooling will need to be carefully controlled to avoid poor fusion between printed layers. These feedback loop controls and hardware additions can be very effective in ensuring more successful and robust printing, but it is also costly and difficult to implement due to the thermal camera set up and the limitation of 3D printer control systems. Also, here we printed a simple thin wall structure, and we assumed the surface temperature captured by IR camera was sufficient in describing the temperature of the material. However, when printing more complicated structures, monitoring only the surface temperature by IR camera may underestimate the actual temperature of the printed material. In that case, adding a top-view IR camera might be handy to monitor the overall temperature distribution over the printed objects. Nevertheless, while thermal imaging may be further optimized and integrated as an in-situ monitoring tool, it cannot reveal the detailed material properties that rheological measurements can achieve.

Both rheological and thermographic measurements can only give parts of the relevant dynamic properties during HE-3DFP, but we can still combine and use their data to guide future applications via HE-3DFP. We therefore have several recommendations based on the

current work: (1) A key parameter for all thermoreversible materials is the gelation temperature, which should be measured prior to printing. (2) Our observations show that a printing material should have a G′ greater than 5000 Pa at room temperature to retain structural stability. (3) Further, conduct creep tests below the gelation temperature can characterize the material deformation over time. If the material is missing essential elasticity (i.e. creeps within the required printing time), one may consider modifying the formulation to improve the material elasticity before printing. For printing cross-linked hydrogels, we suggest to set the syringe temperature just above the gelation temperature to avoid severe material spreading. For jammed dispersions, the syringe temperatures also should be above the gelation temperature, but they can be further increased to soften the materials for smoother extrusion. Meanwhile, the material cooling time is co-determined by the printing speed and the layer length. One can empirically determine the minimal cooling time by printing simple test structures with short layer lengths (e.g. the wall structure used in this study) and observing the layer deformation at various printing speeds. The minimal cooling time can then be used as a guide to determine the printing speed of complex structures. With proper setting of the syringe temperature and printing speed, one can expect much more successful printing of a given material for HE-3DFP.

5.4. Conclusions

We examined the structural deformation of various thermoreversible food materials using thermographic and rheological measurements. Thermal imaging revealed that the extrusion temperatures were consistently lower than the syringe temperature due to cooling at the nozzle. The extruded materials need to have a certain minimum complex viscosity (i.e. greater than 500 Pa·s) for the proper extrusion of a consistent filament. Critical surface temperatures were obtained from thermal imaging as indicator for sufficient material cooling to maintain stable structures.

The combination of thermal imaging and time-temperature superposition creep measurements confirmed that the structural deformation is driven by high material temperature (i.e. melting) and long printing time (i.e. creep). Sufficient material elasticity is needed in food ink formulations to reduce severe creep behavior at elevated temperatures. Combining the insights from thermographic and rheological measurements can determine the optimal syringe temperature and material cooling time. The optimized printing

parameters can therefore reduce extensive the pre-printing experiments and improve the adaptivity of 3D food printing towards thermoreversible food materials.

Chapter 6 Quantitative analysis of 3D food printing layer extrusion accuracy: contextualizing automated image analysis with human evaluations

This chapter has been published as: Ma, Y., Potappel, J., Schutyser, M. A. I., Boom, R. M., & Zhang, L. (2023). Quantitative analysis of 3D food printing layer extrusion accuracy: Contextualizing automated image analysis with human evaluations. Current Research in Food Science, 6, 100511.

Chapter 6

Abstract

3D food printing can customize food appearance, textures, and flavors to tailor to specific consumer needs. Current 3D food printing depends on trial-and-error optimization and experienced printer operators, which limits the adoption of the technology by general consumers. Digital image analysis can be applied to monitor the 3D printing process, quantify printing errors, and guide optimization of the printing process. We here propose an automated printing accuracy assessment tool based on layer-wise image analysis. Printing inaccuracies are quantified based on over- and under-extrusion with reference to the digital design. The measured defects are compared to human evaluations via an online survey to contextualize the errors and identify the most useful measurements to improve printing efficiency. The survey participants marked oozing and over-extrusion as inaccurate printing which matched the results obtained from automated image analysis. Although under-extrusion was also quantified by the more sensitive digital tool, the survey participants did not perceive consistent under-extrusion as inaccurate printing. The contextualized digital assessment tool provides useful estimations of printing accuracy and corrective actions to avoid printing defects. The digital monitoring approach may accelerate the consumer adoption of 3D food printing by improving the perceived accuracy and efficiency of customized food printing.

6.1. Introduction

3D food printing offers design flexibility to create personalized foods with customized appearances and sensory properties. Food materials such as chocolate, purees, and cookie dough have been printed into customized shapes that can appeal to specific consumer cohorts (Lanaro et al., 2017; Pulatsu et al., 2020). By building food structures layer-by-layer, 3D food printing can also modify food texture properties such as hardness and firmness by controlling the infill patterns and percentages of the designed food structures (Derossi et al., 2021; Fahmy et al., 2021). Suitable food textures have been designed and printed for consumers with special dietary needs (e.g. dysphagia patients and people with swallowing difficulties) (Pant et al., 2021). The flavor perception of 3D-printed foods can also be altered, for example by changing the position of the flavor-containing materials to create differences in sweetness and saltiness perception in chocolate waffles and starch-based snacks (Fahmy et al., 2021; Zhu et al., 2020). 3D food printing therefore introduces new opportunities to create customized foods for individual consumer needs.

Although 3D food printing is already possible, printed foods often suffer from poor printing accuracy (i.e. the printed object does not accurately resemble the digital design). Common printing inaccuracies include over- and under-extrusion of printing layers, layer shrinking and/or relaxation, and structural instability. Previous studies have focused on assessing food material printability, which include some aspects of evaluating printing accuracies such as extrudability and structural stability (Kadival et al., 2022; Outrequin et al., 2023). For example, rheological properties such as shear-thinning properties, creep relaxations, yield stress, and flow points have been linked to the extrudability and stability of 3D-printed foods (Ma et al., 2021, 2022; Pulatsu et al., 2020; Zhu et al., 2019). A review by Kadival et al. (2022) highlighted that most food printability studies relied on manual measurements of the structure dimensions to evaluate printability. However, automated and quantitative measurement of printing accuracy can compare different printing results and provide feedback for printability improvement. The 3D food extrudability was quantified by Fahmy et al. (2020) using image analysis. The study measured over- and under-extrusions of extruded starch-based filaments in 2 dimensions. Similarly, Zhu et al. (2019) also used video-based measurement to quantify the stability of 3D-printed tomato puree structures. On top of image-based methods, X-ray tomography (XRT) was also used in several studies to

measure the internal porosity and infill distributions of 3D-printed foods (Agarwal et al., 2022; Derossi et al., 2021). Although the aforementioned studies provide some quantification of printing accuracy, no automated measurement or direct comparison was made between the original digital designs and the resulting printed foods.

In contrast to 3D printing of food, 3D printing of thermoplastics already utilizes image analysis techniques to in-situ monitor printing accuracy. Petsiuk & Pearce (2020) developed a layer-wise monitoring tool to assess the 3D printing quality and track possible printing errors. A follow-up study illustrated the comparison of the measured image data to digitally rendered structures to detect printing anomalies (Petsiuk & Pearce, 2022). Such a smart monitoring system improves the printing accuracy by identifying the causes of anomalies obtained from the automated analysis. Piovarci et al. (2022) developed a closed-loop control system for direct ink writing printers to avoid over- and under-extrusion using image-based reinforcement learning. As food manufacturing is moving towards digitalization and smart processing, various machine vision techniques have been developed for process monitoring and quality evaluation purposes (Zhu et al., 2021). Specifically for 3D food printing, digital image analysis can be promising to quantify printing errors and improve the printing efficiency. Previously, we demonstrated the prediction of food extrudability based on grey-box modeling and the optimization of printing parameters based on computer vision of the extrusion flow rate (Ma et al., 2021, 2023).

Beyond digitally assessing the printing accuracy, human evaluations of the printed food structures are even more important in the context of 3D food printing. Previous sensory studies focused on the sensorial modifications of textures and flavors of 3D-printed foods, while the visual printing accuracy was not often studied extensively in relation to the desirability of consuming 3D-printed foods. An exception is the work of Chirico Scheele et al. (2022) which reported the consumer-rated printing accuracy using a small panel (N = 28). The study showed that participants preferred food structures that closely resembled the digital design, and an increase in the complexity of the printed shape led to higher preference scores. In a follow-up study by the same group (Chirico Scheele et al., 2023), it reported a positive correlation (R^2 = 0.78) between 3D-printed mashed potato fidelity and desirability of consumption based on an online survey with 50 participants. The study also compared manual shape dimension measurements to the survey fidelity rating and suggested

that more variations were found in the survey results than in the manual dimension measurements of the 3D-printed shapes. Therefore, improving 3D printing accuracy can increase desirability of consumption, which is an important first step towards consumer acceptance of 3D-printed foods in the mass market. Furthermore, feedback from manual evaluations can contextualize errors obtained from the dimensional measurements. When developing a digital printing accuracy measurement tool, human evaluations can enhance the applicability of digital methods by contextualizing measurement errors and establishing the relevant tolerance of printing inaccuracy for automated monitoring purposes.

In this study, we aim to develop a layer-wise printing accuracy measuring tool based on automated image analysis and contextualize the digital measurements with human evaluations to establish relevant error tolerance. Cookie dough with different fat sources was 3D-printed and used as example materials for method development purposes. Cookie dough was chosen because it is a common 3D food printing material which also requires post-processing. The layer-wise printing accuracy before and after baking was digitally measured by comparing the 3D-printed cookies to the digital design. An online survey collected visual evaluations of the layer-wise printing accuracy. The survey results and digital assessments were combined to gain insights about printing accuracy and provide guidance to improve future 3D food printing applications.

6.2. Materials and methods

6.2.1. Preparation of printing materials

Wheat flour (Molen de Hoop, the Netherlands), powdered sugar (Van Gilse, the Netherlands), coconut fat (Royal Green, the Netherlands), shortening (Crisco, USA), vegetable oil (Crisco, USA), and butter (Campina, the Netherlands) were purchased from local and online retailers in the Netherlands. Three types of cookie dough composed of different fat ingredients were prepared by using a cookie recipe modified from Pulatsu et al. (2020). Briefly, to prepare 100 g of the cookie dough, i) 20 g of coconut oil, ii) 20 g of shortening, or iii) 10 g of butter and 10 g of vegetable oil was mixed with 17 g of powdered sugar for 5 min at low mixing speed using a kitchen mixer (Kenwood KVL4100, UK), respectively. Then, 49 g of wheat flour was added into the mixture and mixed for 2 min at the same speed. Finally, 14 g of tap water was gradually added into the mixer to form the cookie dough. The cookie dough was mixed for an additional 3 min to obtain a homogenous

texture. After mixing, the cookie dough was rested for 10 min at 20 °C prior to the 3D printing experiment. Table 6.1 provides an overview of the formulations used in this study.

Table 6.1. Formulation overview of the cookie dough used in this study.

Ingredients	Coconut fat cookie	Shortening cookie	Butter and oil cookie
Fat	20 g coconut fat	20 g shortening	10 g butter + 10 g vegetable oil
Wheat flour	49 g	49 g	49 g
Tap water	14 g	14 g	14 g
Sugar power	17 g	17 g	17 g

6.2.2. 3D printing and post-processing

Two digital designs (i.e. block and deer) were sliced using the Slic3r software (https://slic3r.org/) to generate five different printing paths in the form of G-codes. For the block design (50 × 25 × 10 mm), four different printing paths were generated. In specific, 2 infill patterns (rectilinear and honeycomb) and 2 infill levels (20% and 40%) were chosen to make 4 printing paths: rectilinear with 20% infill (RL20), rectilinear with 40% infill (RL40), honeycomb with 20% infill (HC20), and honeycomb with 40% infill (HC40). The deer design was sliced with 0% infill to only print the outline of the geometric design. The digital representations of the printing designs are shown in Figure 6.1.

The cookie dough was carefully transferred into a syringe and printed into the designs based on the corresponding G-codes using an extrusion-based 3D food printer (Procusini 5.0, Germany). The cookie dough was printed onto a calibration plate with visual markers for subsequent image analysis purposes. A retraction of 2 mm was used to avoid material oozing at the start/stop points. The start/stop points are the points where the continuous extrusion was started or stopped (see Figure 6.1). The printing speed was kept constant at 20 mm/s and a nozzle size of 1.2 mm was used throughout all printing experiments. Each printing geometry was printed in duplicate with all three cookie dough formulations listed in Table 6.1. In total, 30 cookie samples were printed (3 formulations × 5 designs × 2 repetitions). After printing, the cookies were baked in a convection oven (Heraeus, Germany) at 200 °C for 15 min. Top-view images (from 50 cm above) of freshly printed and baked cookies were acquired using a digital camera (Oneplus Nord, China).

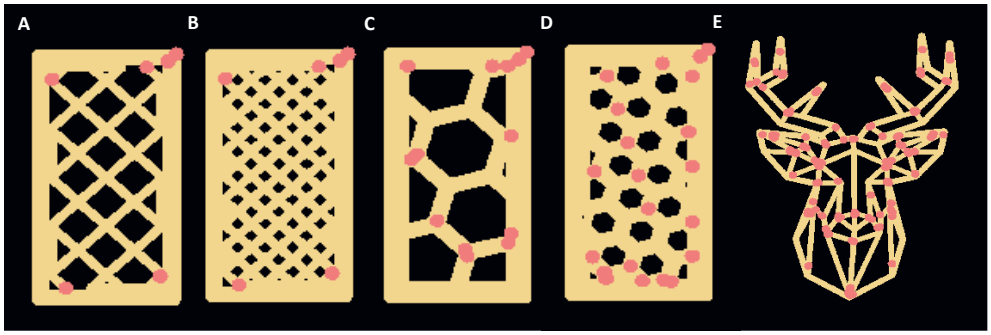

Figure 6.1. Digital representations of the printing designs. A: rectilinear with 20% infill. B: rectilinear with 40% infill. C: honeycomb with 20% infill. D: honeycomb with 40% infill. E: geometric deer. The red dots indicate a start/stop point of the printing extrusion on the printing path.

6.2.3. Human evaluations of printing accuracy

An online survey was designed to collect human evaluations of the 3D-printed cookies. To obtain representative results, 5 freshly printed and 5 baked shortening cookies were chosen to be evaluated in the survey. The first part of the questionnaire collected the participants' demographic information and familiarity with 3D food printing. For the second part of the survey, 10 sets of 2 images (examples shown in Figures 6.2A and B) were presented to the participants in random order. Within each image set, the first image was the top view image of the printed object, and the second image was the corresponding digital design of the printed object regenerated using G-codes (see section 2.4.2). A printing line width of 1.5 mm was used to generate all the digital layer images. This line width was set to be slightly larger than the nozzle size (1.2 mm) because expansion of the extruded filament was expected (Ma et al., 2021). The participants were asked to rate the overall accuracy of the printed object in reference to the digital design, using a range from 0 to 100. The left extreme (0) was labeled as "not accurate" while the right extreme (100) was labeled as "very accurate". Subsequently, the participants were asked to identify the printing inaccuracies by clicking on the image of the printed object. A minimum of 3 clicks and a maximum of 10 clicks were required. In total, 101 respondents completed the survey, and the survey results were visualized using a click frequency heatmap (Figure 6.2C). To generate the heatmap, the images of the printed cookie were divided into grids of 9 × 9 pixels, and the number of inaccurate positions was counted within each grid. The frequency values in the grids were then passed through a Gaussian filter to smooth the frequency

distribution across neighboring grids. The smoothed frequency values were then visualized with a heatmap to identify the printing inaccuracies perceived by the participants.

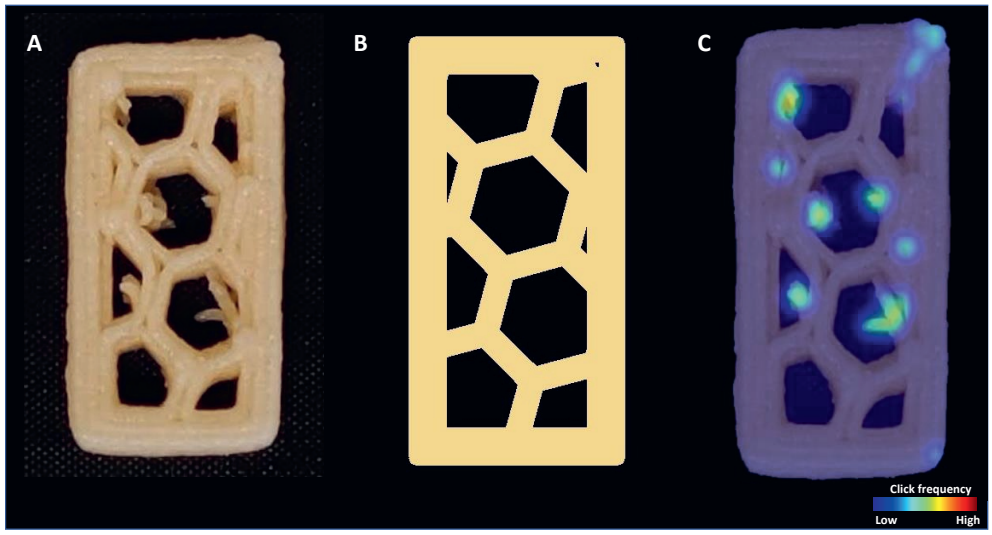

Figure 6.2. Examples of images used in the online survey and a representative result. A: top view of the printed object (20 × 50 mm). B: Digital design of the printed object. C: Click frequency heatmap obtained from the survey.

6.2.4. Automatic image analysis of printing accuracy

6.2.4.1. Image acquisition and preprocessing

Image analysis was used to digitally assess the printing accuracy using the same top-view images as used in the online survey. An automated image analysis pipeline (Figure 6.3) was developed to generate digital layer images based on the G-code, quantify the over- and under-extrusion of the printed cookies, and calibrate the digital assessment based on results from human evaluations. Prior to the analysis pipeline, the raw image (4000 × 3000 pixels) was first automatically cropped and perspective transformed to match the reference frame (240 × 150 mm) as marked by the 4 green visual markers. The cropped and transformed image (2400 × 1500 pixels) was scaled using the known distance between the visual markers. The Otsu automatic thresholding method was applied to segment the printed object from the background (Otsu, 1979).

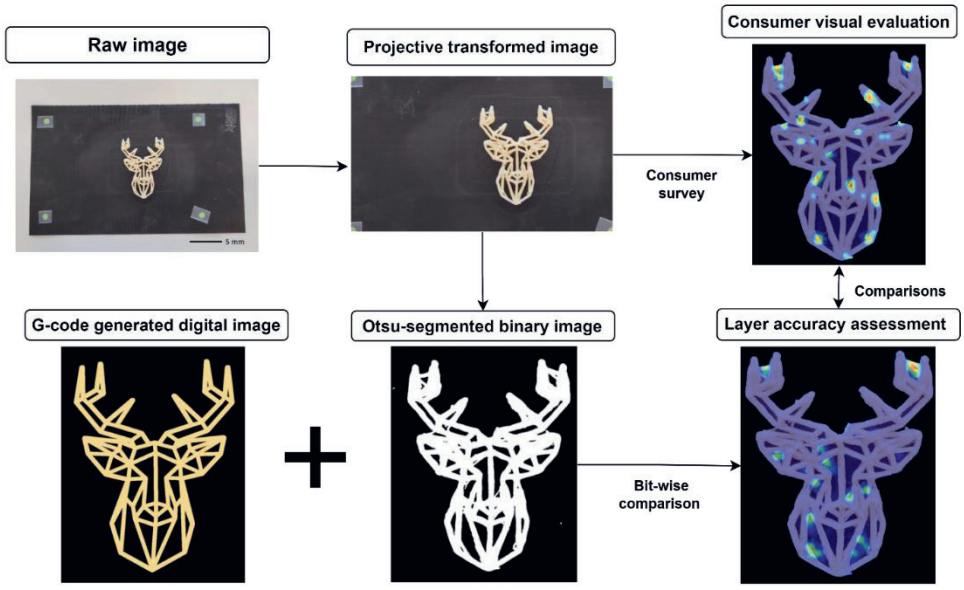

Figure 6.3. Overview of the automated image analysis pipeline to assess layer-wise printing accuracy and comparison to human evaluations.

6.2.4.2. Digital layer image generation

The G-code of the design was parsed into cartesian coordinates of x, y, and z positions of each movement. The corresponding feed rate (F) and extrusion distance (E) were also obtained from the same G-code file. All pairs of motions (X, Y, Z) were connected to iteratively generate the digital layer image. The width of each line was calculated by approximating the cross-sectional area of the extruded filament as a flattened tube. Figure 6.4A shows the ideally extruded filament in a cylindrical shape with a cross-sectional circle (⌀ d) and a given length of L. Upon printing onto a surface, the ideally extruded viscous printing material was flattened into a tube, of which the cross-sectional area can be approximated as a rectangle with 2 semi-circular edges (Ma et al., 2021). Based on the conservation of extrusion volume, the filament width (W) from point A (x_1, y_1, E_1) to point B (x_2, y_2, E_2) is calculated with:

$$W = \frac{\pi \Delta E D^2}{4XH} + \frac{3}{4}\pi H \qquad \text{Eq. 1}$$

where $X = \sqrt{(x1 - x2)^2 + (y1 - y2)^2}$, $\Delta E = E_2 - E_1$, H is the layer height, and D is the syringe diameter.

The pairs of printing motions were then iteratively drawn as connected lines to generate the digital layer image based on the scaling factor of the segmented object image.

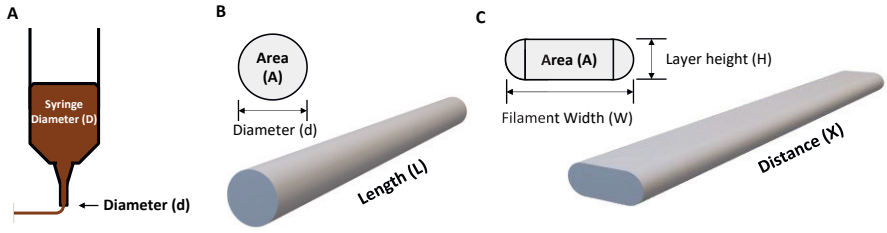

Figure 6.4. Schematic illustration of the filament width estimation. A: schematic illustration of an extrusion-based food printhead. B: ideally extruded filament. C: filament that was extruded onto a flat surface.

6.2.4.3. Layer-wise printing accuracy assessment

The layer-wise image analysis method provides three ways to quantify the printing accuracy, namely the solid infill, the degree of over-extrusion, and the degree of under-extrusion. The infill (%) was measured for the block designs. To measure the infill, the filled pixels of the segmented object image were counted and divided by the total number of pixels within the block structure. The degree of infill quantifies how closely the printed object resembles the designed degree of infill, which directly impacts the texture of the printed foods.

Over- and under-extrusion were measured from top-view images of the freshly printed cookies, shift factors (in x and y directions) between the digital layer image and the segmented object image were obtained by cross-correlating the two images. The G-code-based layer image was shifted to match the center of mass of the segmented object image. Bitwise logical operations were then performed to examine the degrees of over- and under-extrusion of the printed object relative to the G-code designs. The areas of under-extrusion and over-extrusion are calculated by Eq.2 and Eq.3, respectively.

$$U = [P \mid G] \oplus P \qquad \text{Eq. 2}$$

$$O = [P \oplus G] \oplus U \qquad \text{Eq. 3}$$

Where *O* and *U* represent the binary images of the over-extruded and under-extruded areas, respectively. *P* is the segmented object image, and *G* is the shifted digital layer image based on the G-code. The '⊕' represents the XOR logical operation and '|' represents the OR logical operation. An illustration of the pixel-wise comparison is shown in Figure 6.5.

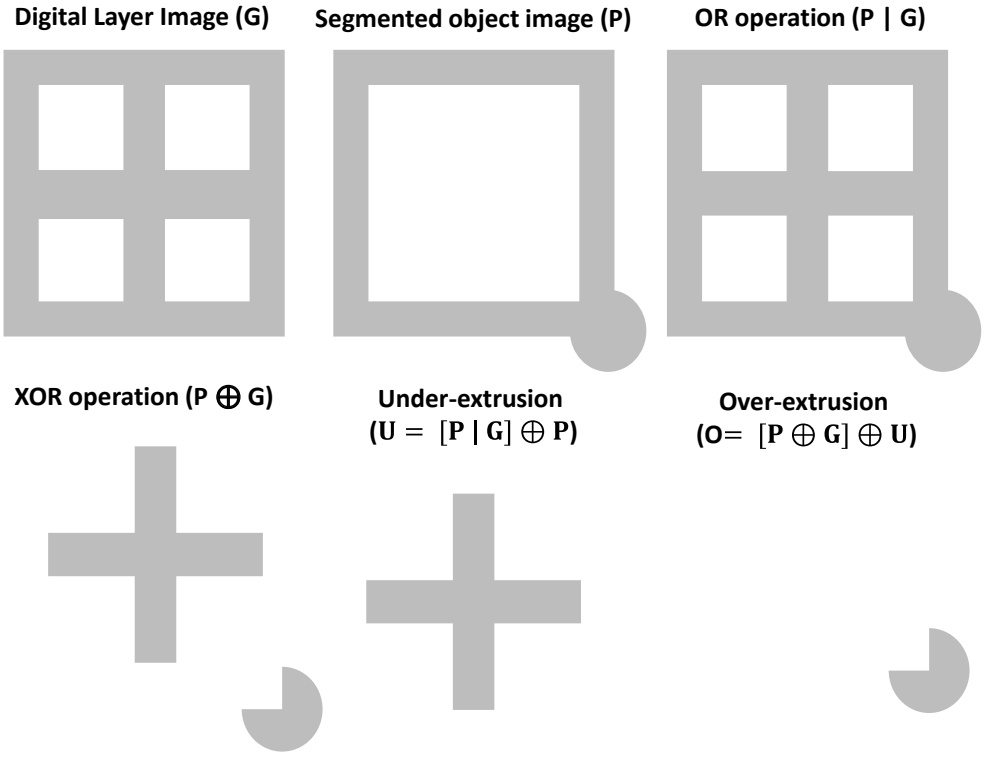

Figure 6.5. A schematic illustration of the OR and XOR logical operation to extract the over- and under-extrusion areas. The '⊕' represents the XOR logical operation and '|' represents the OR logical operation.

Preliminary analysis showed that under-extrusion occurs consistently across the complete printed structures, while over-extrusion is more sporadic. To further localize the over-extruded positions on the printed object, the over-extruded proportions were calculated within 9 × 9 grids to evaluate the local printing accuracy. With *n* grids, the O_n were calculated using Eq.3 Over-extrusion indices (i_{over}) were calculated based on Eq.4.

$$i_{\text{over n}} = \frac{\sum O_n\,[\,o=1]}{\sum P_n\,[\,p=1]+1} \qquad \text{Eq. 4}$$

Where *n* represents the *n*th grid in the original image and *p* represents the pixels within the P_n image grid. The lists of indices (i_{over}) of each image were further normalized using a modified percentile normalization technique (Eq. 5) to account for extreme values calculated from Eq. 4. The normalized i'_{over} was visualized with a heatmap as the initial evaluation of the printing accuracy assessment.

$$\begin{cases} if\ i > q_I, 99\% & i' = 1 \\ if\ i =< q_I, 99\% & i' = \frac{i - \min(I)}{q_I, 99\% - \min(I)} \end{cases} \quad \text{Eq. 5}$$

Where i' is the normalized over- or under-extrusion index, $q_I, 99\%$ is the 99th percentile of $I_{over.}$

Since baking may induce additional layer dimension changes, the same layer printing accuracy measurements were also performed on the images of baked cookies. "Incompletion from design" was quantified based on Eq. 2 by comparing the digital layer image and the segmented baked cookie image. Similarly, "expansion from design" was calculated based on Eq. 3 and visualized using Eq. 4 &5 by comparing the digital layer image and the segmented baked cookie image. The changes between over-extrusion and expansion from design and the changes between under-extrusion and incompletion from design were compared to evaluate the impact of baking to layer printing accuracy.

6.2.5. Data analysis and software availability

Pair-wised t-tests, analysis of variance, and Pearson's correlation tests were conducted using the R programming language. The automated image analysis software was developed using the OpenCV, NumPy, Pandas, and Scikit Image libraries in the Python programming language. The software including a graphical user interface, raw scripts, 3D designs, and the online survey can be accessed through https://git.wur.nl/yizhou.ma/layer-wise-printing-accuracy.

6.3. Results & Discussions

In the following sections, the human evaluation of the printing accuracy is introduced to establish the baseline of the printing accuracy of the 3D-printed samples prepared in this study. Then, printing accuracy measurements from automated image analysis are present

and contextualized with the results from human evaluations to establish measurement relevance and error tolerance.

6.3.1. Human evaluations of printing accuracy

In total, 101 valid survey results were obtained from the online questionnaire. The participants consisted of 63 female, 36 male, and 2 non-binary persons with a mean age of 29 years old. Because the survey participants mostly came from food research institutions and companies, 91% of the participants had at least heard about the concept of 3D food printing (i.e. 'a little familiar') (Figure 6.A1). Figure 6.6 summarizes the human-rated printing accuracy results. Overall, some variation in the accuracy ratings was observed across all samples. Because the participants of the online survey were untrained, no reference or calibration was done to prime the accuracy towards a certain range. Nevertheless, for each of the block designs, the freshly printed cookies scored significantly higher in printing accuracy compared to the baked ones ($P < 0.05$). Baking induces a series of physicochemical changes in cookie dough, including water evaporation, fat melting, and starch gelatinization (Pulatsu et al., 2020). As a result of baking, cookies generally spread, collapse in height and their structure deforms (Kim et al., 2019). The dimensional changes negatively impacted the human-rated printing accuracy because they result in further shape deviations from the digital designs. However, for the deer structure, no accuracy difference was observed between the fresh and baked samples, possibly due to the complex structural design, which contains less of the regular geometric elements such as grids and hexagons, in which printing inaccuracies are easily detected. Visual food design complexity has shown to improve food attractions and consumer liking in fine dining and children dining settings (Hamilton et al. 2018; Michel et al. 2014). Therefore, printing more complex structures may alleviate the negative impact of baking by offering more attractive food designs. Meanwhile, according to Chirico Scheele et al. (2022), higher shape complexity also leads to higher consumer preference for 3D-printed foods. Simple geometries (such as the blocks in this study) may be more suitable to evaluate printing stability of food materials in laboratory settings for formulation/process optimization purposes. However, for the perception by consumers, the 3D printing of complex and customized food shapes might be more suited.

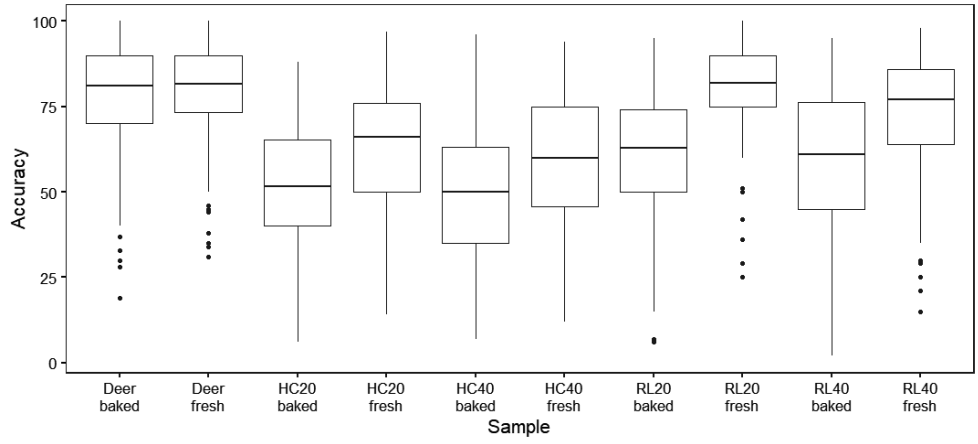

Figure 6.6. Human-rated printing accuracy of the shortening cookies. HC20 = honeycomb pattern with 20% infill, HC40 = honeycomb pattern with 40% infill, RL20 = rectilinear pattern with 20% infill, and RL40 = rectilinear pattern with 40% infill.

In the same survey, the inaccurate printing positions were also marked. A strong inverse correlation ($r = 0.86$) was found between the total number of inaccurate positions and the human-rated accuracy, indicating that participants marked more inaccurately printed positions on images with a lower accuracy score (Figure 6.A2). After confirming the validity of the online survey, the inaccuracies were visualized and overlayed with a digital layer image of the original design. Human evaluations captured printing inaccuracy caused by two typical printing defects, namely material oozing and over-extrusion at the start/stop points.

Figure 6.7 shows a representative example of the inaccuracy heatmap generated by the visual evaluations of the questionnaire participants. Some of the inaccuracies can be related to material oozing, which is a common defect in 3D printing of soft materials such as hydrogels and foods (Fahmy et al., 2020; Keong & Hua, 2018). Oozing occurs when the printing flow is not effectively stopped due to material elasticity and/or low viscosity. As observed in Figure 6.7, the oozed positions appear to be in between start/stop points on a printing path. During printing, an excess of material flows out of the nozzle when the print head travels to the next start/stop point. In printing parameter optimizations, oozing can be reduced by adjusting the retraction length of the print head (i.e. in the G-codes). For example, Liu et al. (2018) specifically optimized the retraction length to compensate for the oozing of a potato/strawberry juice gel during printing.

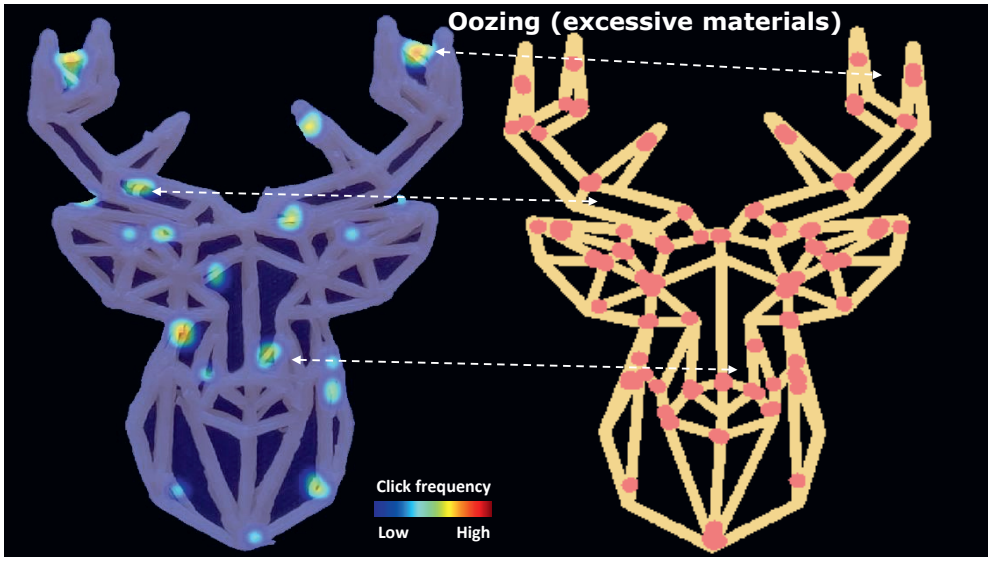

Figure 6.7. Printing inaccuracies (e.g. oozing) indicated by human evaluations of the freshly printed deer-shaped cookie. The dashed arrows indicate the oozing effects. The red dots represent the start/stop points of a printing layer.

Another representative type of inaccuracy marked manually is over-extrusion at the start/stop points (Figure 6.8). The extrusion pressure and flow need to be equilibrated at the beginning or at the end of the extrusion, which leads to variations in material flow (Ma et al., 2023). For the 3D-printed cookies featured in this study, a consistent 2-mm retraction at a speed of 60 mm/s was set in the printing settings. In reality, the speed of the retraction was not fast enough to rapidly stop the extrusion flow, which can lead to over-extrusion of the material at the stop point of a continuous extrusion path. At the start of an extrusion path, the retracted 2 mm needs to be compensated by quickly bringing the piston down, which can lead to an over-extrusion at the beginning of a printing segment. The over-extrusion at the start/stop points can be explained by the shear-thinning behavior of the cookie dough. A rapid push of the piston increases the pressure in the syringe, which then reduces the printing material's viscosity, leading to the observed over-extrusion shown in Figure 6.7. For 3D printing of soft materials, a continuous extrusion of the printing materials across the printing path is therefore preferred over having multiple start/stop segments (Fernandez et al., 2019). Our results from the survey support this finding. Thus, optimizing the printing path by using continuous extrusion may improve the printing accuracy as perceived by human evaluators.

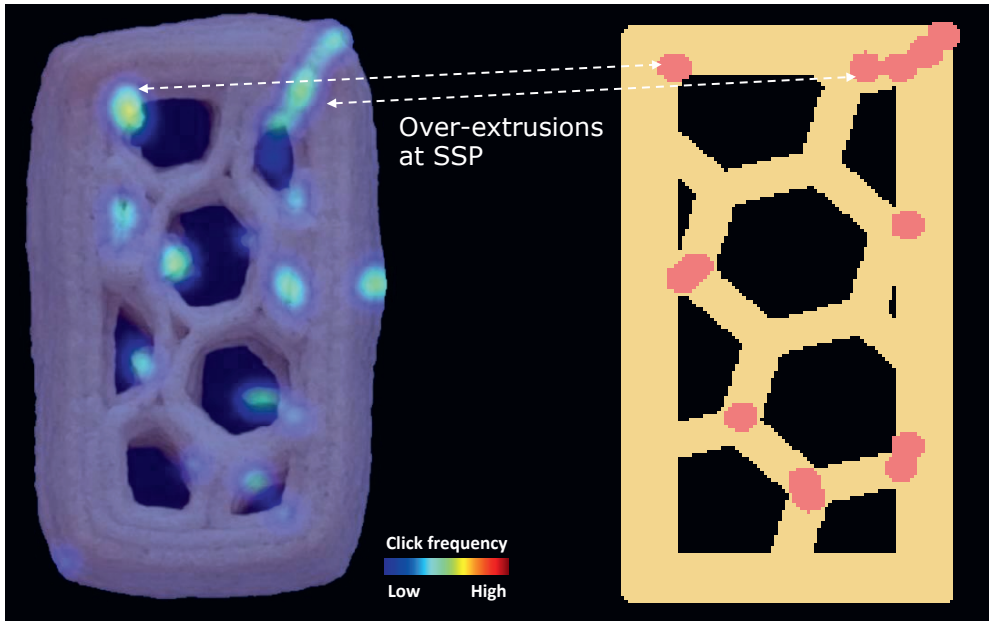

Figure 6.8. Printing inaccuracies (over-extrusion at start/stop points) indicated by human evaluations of a baked cookie with a 20% honeycomb infill pattern (20 × 50 mm). The dashed arrows indicate the over-extrusion effects. The red dots represent the start/stop points of a printing layer.

Overall, the printing inaccuracies marked by survey participants are related to over-extrusion defects rather than those of under-extrusion. This is likely due to that we surveyed layer printing accuracy of the final printed shape. In 3D food printing applications, under-extrusion of printing materials often occurs at the beginning of an extrusion and is more observable when printing single layers (Fahmy et al., 2020; Ma et al., 2023). During 3D printing of multiple layers, the under-extruded portions can be covered by subsequent layers, which makes under-extrusion less recognizable from the top-view. In contrast, over-extrusion is more observable and directly comparable with the digital design using the automated image analysis measurement. Therefore, a quantitative approach is needed to measure the over-extrusion to monitor and control the 3D food printing process and achieve better printing accuracy. The insights from the online survey serve as the basis for the subsequent evaluation of the printing accuracy using the automated digital assessment tool.

6.3.2. Layer-wise digital image analysis of printing accuracy

Layer-wise digital image analysis is used to describe how well the freshly-printed or post-processed food structure resembles the original digital design. In this study, we measured the degree of layer infill (%) before and after baking as a general indicator for the textural modifications. Then, the over- and under-extrusion of the printed cookies were quantified to connect the observed printing inaccuracy to corrective control actions.

6.3.2.1. Layer infill measurement

The degree of infill of the block designs was first measured based on the layer-wise image analysis method. It determines the porosity of the printed structure, which is a common design parameter to control the textural properties of 3D-printed foods (Fahmy et al., 2022; Zhu et al., 2021). Figure 6.9 highlights the measured degree of infill of cookies before and after baking by analyzing the corresponding top-view images. Even though the 2D infill setting in the Slic3r software was either 20 or 40%, the measured infill of the digital layer image was 77 or 88%, respectively. The deviation between the software infill settings and the measured infill % shows that the Slic3r software setting is not an accurate estimation of the infill of the true layer. Severini et al. (2016) reported a similar difference between the software infill settings and the solid fractions of the printed object. The authors suggested that the software infill calculation does not include the external shell, which constitutes a large part of the solids in the printed structure. For accurate estimations of the infill % and structural porosity, one should use the digital layer image generated from this study as the reference rather than simply relying on the slicing software settings.

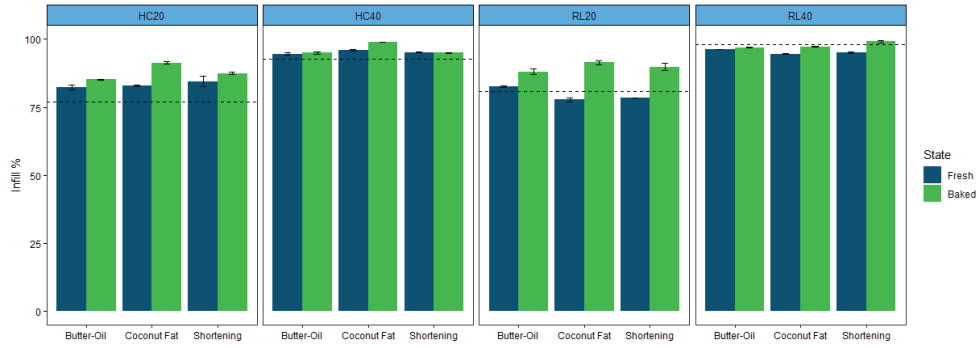

Figure 6.9. Layer infill % measured by the digital image analysis method developed in this study. HC20 = honeycomb pattern with 20% infill, HC40 = honeycomb pattern with 40% infill, RL20 = rectilinear pattern with 20% infill, and RL40 = rectilinear pattern with 40% infill. The error bar indicates the standard deviation of the averaged infill % (n = 2). The dashed line indicates the degree of infill calculated from the digital layer image obtained from the G-code in section 2.4.2.

Across the different structures, except for the RL40, most of the printed structures exceeded the degree of infill of the digital design. This is likely due to over-extrusion. For RL40, the designed infill obtained by analyzing the G-code generated image is over 90%, which makes the effect of over-extrusion less apparent. Overall, baking leads to a significant increase in the degree of infill for all structures ($P < 0.05$). The baking-induced cookie dough spread agreed with the human evaluation results discussed in section 3.1. For textural modification purposes, one should therefore determine the degree of infill of the baked cookies (e.g. or porosity) and how that influences the cookie texture, rather than only relying on the degree of infill of the digital structure or the freshly printed objects. For example, in some previous studies, researchers used X-ray computed tomography to directly measure the true porosity of the 3D objects (Derossi et al., 2021; Severini et al., 2018), which is an effective method to quantify textural modification and structural porosities in laboratory settings. For practical situations, the degree of infill based on our layer-wise image analysis provides 2D infill measurement that can offer rapid and cost-effective estimations suitable for routine 3D food printing applications.

6.3.2.2. Over-extrusion

For all cookies, the baked version had significantly ($P < 0.05$) more over-extrusion compared to the freshly printed cookie dough (Figure 6.10). The spreading of baked cookies aligned with previous observations from the survey and the measured degrees of infill (section 3.1,

and section 3.2.1). The increased over-extrusion after baking leads to reduced accuracy of the printed structures. It is worth noting that all samples exhibit some over-extrusion when compared to the digital designs. The source of this may be the die-swelling during extrusion-based 3D food printing (Le-Bail et al., 2020). Cookie dough is first compressed and extruded through a small nozzle, after which the elastic cookie dough can relax which leads to transversal expansion of the filament. Such a die-swell effect results in wider filaments, which contributes to the observed over-extrusion shown in Figure 6.10. No significant difference ($P > 0.05$) was found among the fat ingredients. While the fats had different melting points, all cookie doughs contained solid fat crystals, and exhibited a similar die-swell during extrusion and spreading after baking.

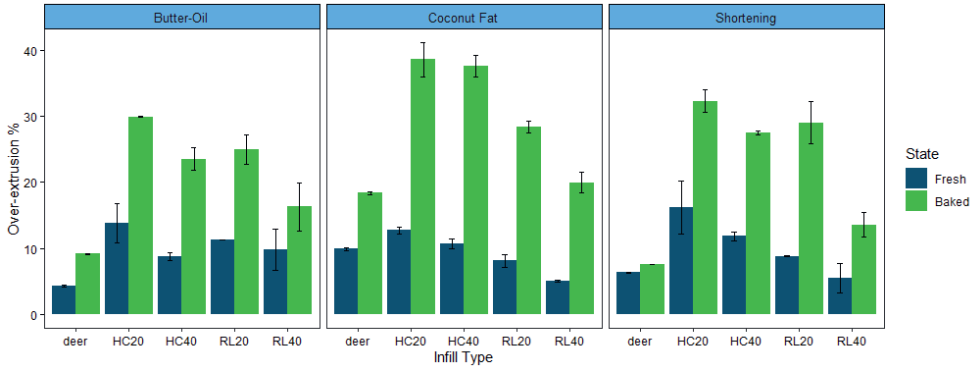

Figure 6.10. Over-extrusion % (fresh) and expansion from design % (baked) 3D-printed cookies measured by the layer-wise image analysis method developed in this study. HC20 = honeycomb pattern with 20% infill, HC40 = honeycomb pattern with 40% infill, RL20 = rectilinear pattern with 20% infill, and RL40 = rectilinear pattern with 40% infill. The error bar indicates the standard deviation of the averaged over-extrusion % or expansion from design % (n = 2).

Over-extrusion at the level of the whole image provides an overview of the printing accuracy. Using the automated image analysis tool, we can also localize the printing inaccuracies within a given structure similar to the human evaluations discussed in section 3.1. These localized printing inaccuracies may identify the cause of the printing defects and help to eventually improve the printing paths to minimize the inaccuracies. Figure 6.11A highlights the over-extruded positions of a freshly printed coconut oil cookie (RL20) on a heatmap. The over-extrusions are sparse across the rectilinear block structure, rather than distributed evenly. Compared to the digital layer image (Figure 6.11B), the measured over-extruded positions overlap with the start/stop points. This observation agrees with the

human evaluations, in which participants also marked the over-extrusions at the start/stop points. The automated layer-wise image analysis therefore can capture over-extrusion similar to human evaluations. In addition, some oozing is identified in Figure 6.11A, which aligns with the survey results discussed in section 3.1. Both human evaluations and automated image analysis suggest that over-extrusion is likely to occur when the extrusion flow is disrupted (e.g. at start/stop points).

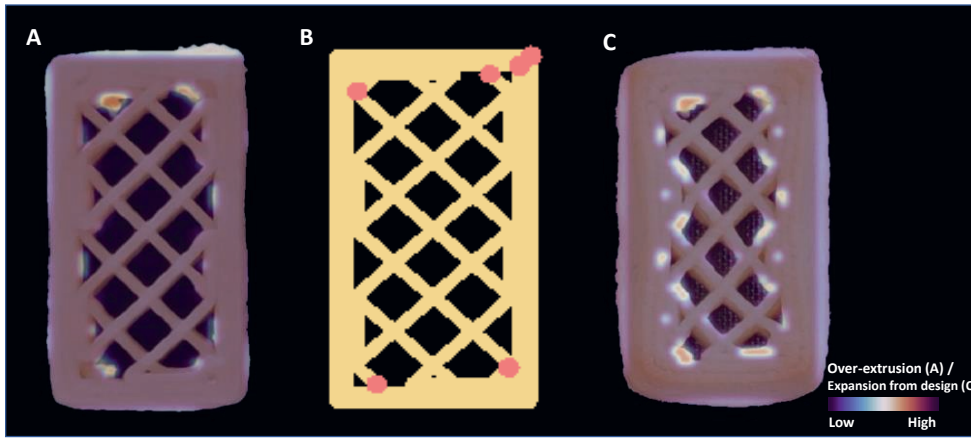

Figure 6.11. A: over-extrusion visualization of the freshly printed coconut oil cookie. B: digital layer image of the rectilinear pattern and 20% infill (20 × 50 mm). C: expansion from design visualization of the same cookie after baking. The red dots represent the start/stop points of a printing layer.

When evaluating the same cookie before and after baking, many more over-extruded positions are identified in Figure 6.11C. These all appear between the external shell and the infill lines, indicating some structural deformation during baking (i.e. the external shell collapsed towards the pore-filled center). In general, a decrease in height and an increase in width and length by baking is observed (Kim et al., 2019). As shown in Figure 6.10, after baking, the layer-wise over-extrusion increases for the RL20 coconut cookie. The reduced printing accuracy of a 3D printed food after processing is consequently not only determined by the printing process, but also by the post-processing treatment (Petsiuk & Pearce, 2020). Corrective control actions such as reducing the printing speed and adjusting the baking parameters may alleviate the observed over-extrusion during printing or post-processing.

Overall, the automated image analysis provides comparable over-extrusion results as human evaluations of the freshly-printed samples. The human evaluations contextualize the digital

measurements, which support that human assessment and digital image analysis recognize the same level of printing inaccuracy in terms of over-extrusion. Digitally quantifying over-extrusion can therefore be applied for in-line monitoring and post-printing screening purposes. When determining the printing accuracy of the final product, post-processing parameters should also be considered as structural changes such as collapse and deformation are likely to happen during post-processing. By routinely monitoring the printing accuracy of freshly printed and post-processed structures, future studies may be able to connect post-processing parameters to printing accuracy, which can use the digital image data obtained from this study for further process optimization purposes.

6.3.2.3. Under-extrusion

While over-extrusion is an apparent indicator of inaccurate printing, under-extrusion provides another aspect of layer accuracy characterization. Figure 6.12 highlights the measured under-extrusion for all the 3D-printed cookies. Overall, the extent of under-extrusion (up to 15%) is less than the extent of over-extrusion (above 30%). In contrast to the deer design, the block designs consistently had less than 8% under-extrusion. This lower degree of under-extrusion matches with our earlier speculation that 3D printing operators may have some selection bias to avoid printing with little or no extrusion flow.

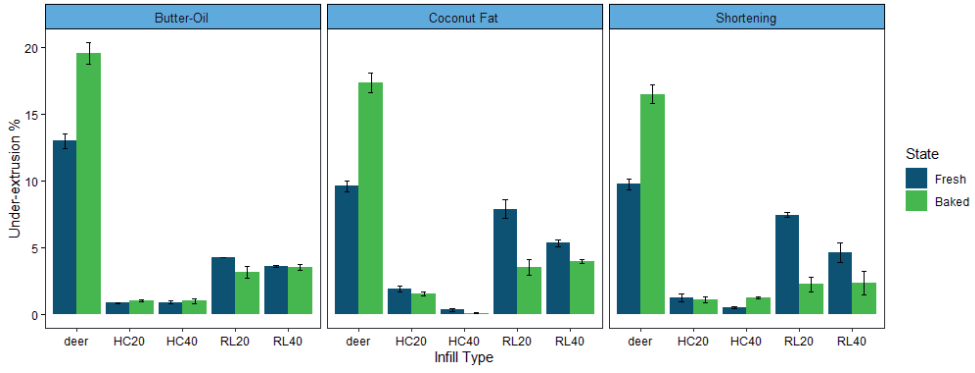

Figure 6.12. Under-extrusion % (fresh) and incompletion from design % (baked) 3D-printed cookies measured by the layer-wise image analysis method developed in this study. HC20 = honeycomb pattern with 20% infill, HC40 = honeycomb pattern with 40% infill, RL20 = rectilinear pattern with 20% infill, and RL40 = rectilinear pattern with 40% infill. The error bar indicates the standard deviation of the averaged under-extrusion % or incompletion from design % (n = 2).

A general decreasing trend is observed when comparing the under-extrusion of the freshly printed and baked blocks. This decrease in under-extrusion correlates with the increase in over-extrusion as discussed in previous sections, which can be explained by the baking expansion and spread of the cookie dough. However, it is interesting to observe that for the deer design, more under-extrusion is found for both the freshly printed and the baked structures. Because the deer design is a single-line geometrical drawing, the increase of under-extrusion in the freshly printed structure may indicate a misposition between the printed structure and the digital layer image. After extrusion, the single extruded lines are subject to relaxation, which may appear as shrinking or rounding off of the printed shape, causing the misposition as highlighted in Figure 6.13A. Due to the larger surface area of the deer structure, the structure may experience more moisture loss during the same baking time, which then causes further shrinking and misposition of the baked deer structure (Figure 6.13B). In addition, as shown in Figures 6.10 and 6.12, over-extrusion and under-extrusion can co-exist at the whole image level, emphasizing the necessity to localize the printing inaccuracy and analyze the specific regions of error.

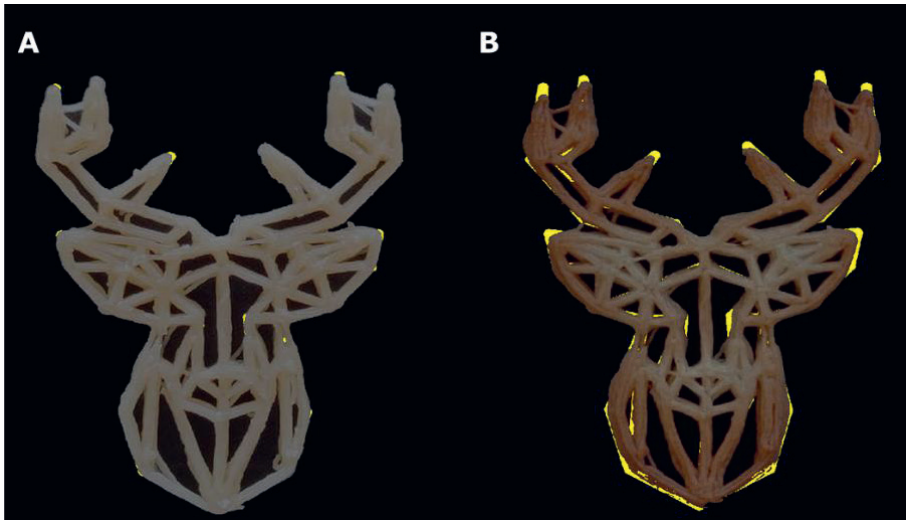

Figure 6.13. Under-extrusion visualizations of freshly printed (A) and baked (B) deer structures printed with the shortening cookie dough. The yellow color represents the missing position of the print in comparison to the digital design.

Figure 6.14 shows some examples of block designs to compare the locations of under-extrusion to the inaccuracies identified by the survey participants. The yellow pixels highlight

the missing positions compared to the digital layer image (Figure 6.14A). For a freshly printed cookie, consistent under-extrusion is found as the highlighted yellow regions are evenly distributed around the infill lines. The survey participants did not identify such a consistent under-extrusion as printing inaccuracy (Figure 6.14B). The human-rated printing inaccuracies are driven by over-extrusion. After baking, the cookie dough spreads and deforms, which reduces some of the under-extrusion as measured via the layer-wise method (Figure 6.14C). However, the under-extrusion positions still do not overlap with the human-rated inaccurate positions. Human evaluations do not identify consistent printing accuracy errors such as the under-extrusion observed in Figure 6.14A, but rather mostly see irregularities. This illustrates the valuable insights collected from human evaluations, which can help calibrate the digital method to best identify relevant printing defects. Without the human evaluation reference, the layer-wise digital method may measure excessive under-extrusion of a given structure and reject it as an inaccurate print, while consumers would not mind. Contextualizing the various errors in printing accuracy by calibrating with human evaluations is therefore vital to the applicability of the digital method developed in this study.

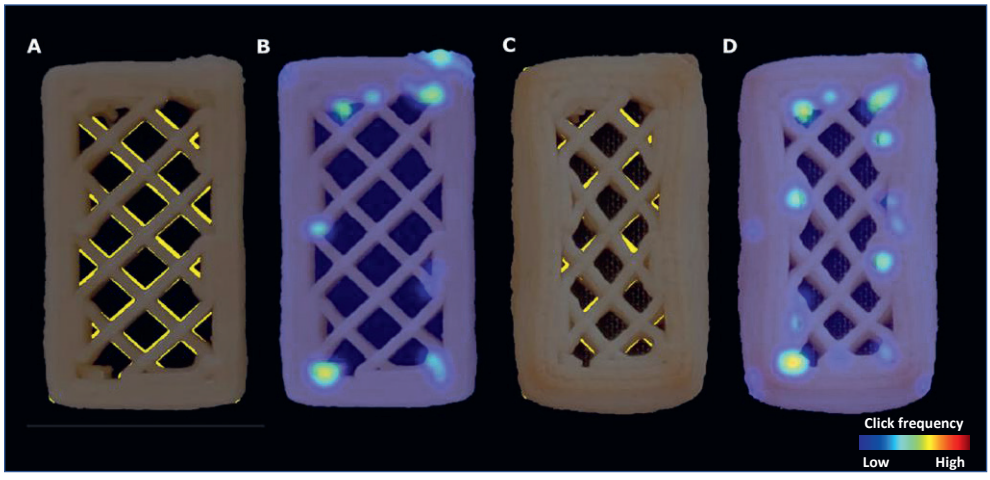

Figure 6.14. A: visualization of under-extrusion of the freshly printed coconut oil cookie with the rectilinear pattern and 20% infill (20 × 50 mm). B: the same cookie evaluated manually. C: baked coconut oil cookie with the rectilinear pattern and 20% infill (20 × 50 mm). D: the same cookie evaluated manually. The yellow color in A and C represents the missing position of the print in comparison to the digital design.

6.3.3. General discussion

Layer-wise image analysis is a simple and automated monitoring technique to measure 3D printing accuracy. Usually, the target of 3D printing is to replicate digital designs as closely as possible, so any defects (e.g. over- and under-extrusions) should be avoided as much as possible (Piovarci et al., 2022). Printing anomalies (e.g. blocked nozzle, incomplete print) are well-defined and monitored in 3D plastic and metal printing applications (Petsiuk & Pearce, 2021). However, for 3D food printing, there is no standardized definition of printing quality solely based on numerical measurements. Because the ultimate purpose of 3D food printing is to provide customized foods, consumer opinions should be included when performing printing quality assessment. Therefore, a digital assessment tool should be validated with feedback from humans. Even though under-extrusion was frequently detected by the automated image analysis method, the survey participants did not recognize under-extrusion as inaccurate printing in the current study, as long as it occurs consistently across the structure. This observation may be different when the consumers taste printed foods with under-extrusions, as they may have less mechanical strength and carry a different textural property. For the end application of 3D food printing, consumer inputs should define what type of printing accuracy is important, which can then be used to calibrate the digital quality assessment tool(s) developed in this study.

Automatically detecting the printing inaccuracies provides indications of 3D-printed food quality, but it will be more beneficial to link the detected inaccuracies to corrective actions during printing. The most effective action, as suggested by Petsiuk & Pearce (2020), is to stop faulty printing jobs when irreversible defects are identified. This automatic shut-down function can certainly save time and printing waste in manufacturing, but more specific actions may increase the adaptability of 3D printing. For example, in Figure 6.15, when oozing is detected, additional retractions can be built into the subsequently printed structure (via modification of the G-code), which provides a dynamic amount of retractions based on the image analysis feedback. This adaptive approach is especially helpful when producing multiple structures in a continuous printing series, which is often the case for personalized food productions. Furthermore, quantifying the layer-wise printing accuracy using image analysis can provide insight about the effects of material properties such as shear recovery and creep relaxation. For example, an increase of the printing line width or consistent geometric shrinking can be linked to certain rheological properties of the specific

printing materials. Formulation adjustments can then be implemented to minimize the apparent printing errors by including additional functional ingredients. Finally, with such a digital method, one can further optimize post-processing parameters by comparing the freshly printed and post-processed printing accuracy. The automated image analysis method provides rapid feedback to collectively optimize printing material formulation, printing parameters, and post-processing parameters.

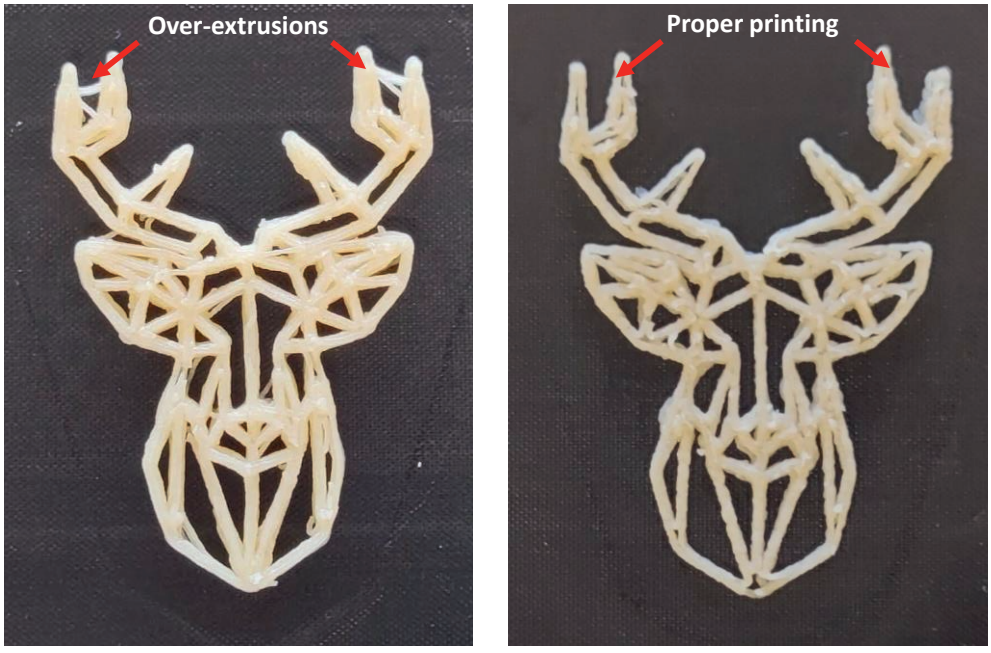

Figure 6.15. Corrective action showcase. A: Original deer structure printed with the shortening cookie dough. B: Improved deer structure to prevent over-extrusion by increasing the level of retractions. The red arrows indicate the accuracy improvement before and after the corrected retraction.

Although layer-wise image analysis can provide actionable assessment for 3D food printing, the current monitoring approach comes with some limitations. For all structures featured in this study, no bottom layer was printed to provide a color contrast to segment the printed structure from the background. Therefore, the layer-by-layer assessment is not possible using a single 2D camera. In addition, corrective actions such as increasing the amount of retraction are still manually implemented. Further automation of the 3D food printing process is limited by the current system which does not allow for in-line adjustment or closed-loop control. To address these limitations, future implementations of the layer-wise

monitoring method may use high-resolution 3D cameras to capture both the color and depth information of a given layer. Sub-millimeter resolution of depth could enable segmentation of a single layer to allow layer-by-layer printing accuracy assessment. Ultimately, sophisticated printing controllers can be adapted from metal and plastic printers to 3D food printing, which can empower in-line control during 3D food printing.

6.4. Conclusions

In this study, automated layer-wise image analysis was employed to quantify 3D food printing accuracy in terms of over- and under-extrusion. The measured printing inaccuracy was compared to human evaluations to contextualize the digital measurements. Human evaluators identified inaccurate printing aspects as oozing and over-extrusion localized at the start/stop points on a printed structure. The human-rated and digital evaluations both captured over-extrusion of 3D-printed cookies. Baking in general negatively impacts the printing accuracy of 3D-printed cookies with simple geometries. While the digital method captured under-extrusion as a printing defect, human evaluations did not identify consistent under-extrusion as inaccurate printing in the survey. The insight from the human evaluations can therefore guide the digital assessment based on layer-wise image analysis. Based on the digital assessment, corrective actions such as increasing retractions to prevent oozing can be realized to improve the printing accuracy. A digital method guided by human insights can provide simple and automated evaluations of 3D food printing accuracy and provide meaningful guides to improve printing accuracy and efficiency.

6.5. Appendix

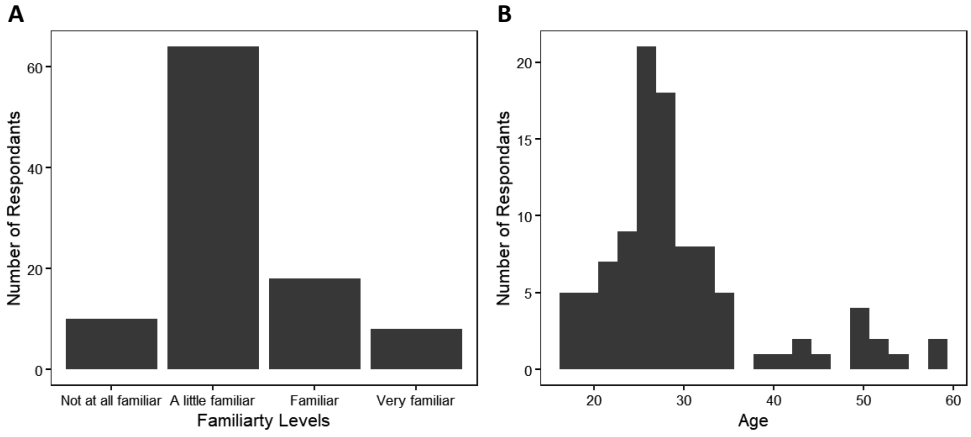

Figure 6.A1. Familiarity levels (A) and age (B) distributions of the survey participants.

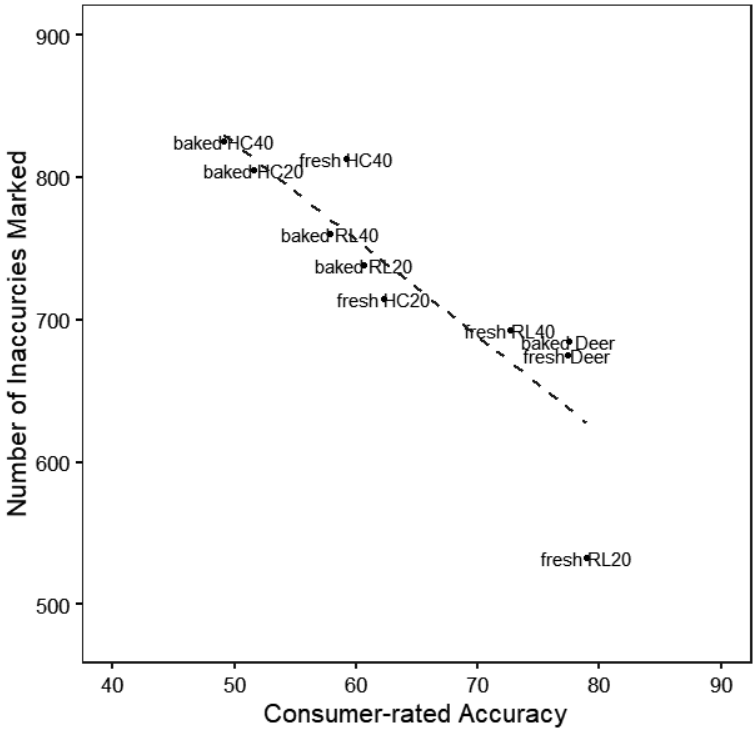

Figure 6.A2. Consumer-rate 3D printing accuracy vs. total number of 3D printing inaccuracies marked per image by survey participants. Correlation = 0.88.

Chapter 7 Fracture mechanics with digital image correlation guides infill design of 3D-printed snack bars with modulated flexural properties

This chapter has been accepted for publication in Virtual and Physical Prototyping as: Ma, Y., Schutyser, M. A. I., Boom, R. M., & Zhang, L. (2024). Quantification of fracture mechanics with digital image correlation guides the infill design of 3d-printed snack bars with modulated flexural properties..

Chapter 7

Abstract

Customization of food texture is a promising application of 3D food printing. Although material compositions, processing parameters, and structural porosity can impact the food texture, the ability to design complex infill patterns is unique to 3D food printing. This study systematically investigated the impact of infill designs on the flexural properties of 3D-printed snack bars made from pea ingredients, by changing the infill angles and orientations. An infill angle perpendicular to the outer shell surface results in larger flexural strength, while an infill angle parallel to the shell increases the structure's flexural elongation. Creating crossed structures did not improve the flexural properties of the samples. Digital image correlation was used to visualize the deformation behavior and fracture propagation of 3D-printed snack bars during mechanical tests. Using the strain maps generated, the designs of the 3D-printed snack bars were modulated to achieve desired flexural properties. Overall, this study shows that it is feasible to customize 3D-printed food texture while maintaining its total calorie content, by simply changing the infill design.

7.1. Introduction

3D food printing can produce personalized foods tailored towards the individual's preferences and nutritional needs. Because of its production flexibility, 3D food printing can fabricate food products with customized appearances, texture, and flavor profiles targeting different consumer preferences (Ma & Zhang, 2022). Among its customizing capabilities, texture modulation is one of the most studied applications of 3D food printing. Various studies attempted to customize 3D-printed food texture through altering the inner structure by changing the infill density of a given design. The infill density represents the solid fraction in a food structure, which directly determines its porosity at the macro level. Derossi et al. (2021) proposed the concept of "programmable" food texture based on 3D food printing. By changing the macroscopic pore density and distributions of 3D-printed cereal snacks, the authors outlined a relation between food hardness and the relative density based on the Gibson-Ashby model. Similarly, Fahmy et al. (2022) carried out a set of experiments to model textural changes in the elastic regime by altering the infill density using finite element modelling (FEM). This further supports the concept of texture modulation based on 3D food printing. Several others studies reported similar results using different food materials such as cheese, lemon mousse, and mashed potatoes to demonstrate 3D food printing as a method to modify food texture (Chow et al., 2021; Le Tohic et al., 2018; Liu et al., 2020).

Although changing the infill density can be effective to modify the texture, sometimes it is difficult to change the amount of porosity in a food structure because food applications are limited to a fixed amount of starting materials (e.g. to control the amount of calories per serving). In this case, texture modulation can be achieved by modifying the infill patterns, which determine the spatial distribution of the pores in a food structure. For example, Zhu et al. (2021) conducted instrumental and sensory analysis to demonstrate the impact of infill patterns on the hardness and chewiness of 3D-printed protein bars. The study reported that a design with a concentric infill pattern had a softer sensory perception compared to rectilinear and layered patterns. Similarly, the impact of infill patterns on the texture of 3D-printed cookies was explored in a different study (Maldonado-Rosas et al., 2024). Their 3D-printed cookies contained triangled and squared pores while having the same solid fraction. The flexural properties of the samples made with different infill shapes were determined by

performing three-point bending tests. Designs with squared pores were stronger but less elastic compared to those with triangled pores. This study further suggests that the infill pattern can impact the overall mechanical properties of 3D-printed foods. The detailed, internal fracture mechanism of 3D-printed food structures and its interaction with infill patterns remain however unelucidated. This lack of clarity makes it challenging to modulate infill designs of a food structure to achieve specific texture profiles.

From a material science perspective, many 3D-printed snack bars with macroscopic pores can be classified as sandwich structures, with the top and bottom faces sheeted by solid materials while the core contains macroscopically distributed, porous solids (Rajpal et al., 2018). Sandwich structures made of metal and thermoplastics in other application areas are studied extensively in terms of core shapes and orientations. Those designs are analogous to the infill patterns in the context of 3D food printing (Zaharia et al., 2020). Three-point bending tests are commonly used to characterize the strength and fracture process of sandwich structures. Previous studies showed that upon three-point bending, a sandwich structure experiences a combination of core shear fracture (breaking of the infill structure) and shell delamination (breaking of the shell structure) (Liu et al., 2023). In food studies there has been little attention to the detailed fracture mechanics of such sandwich structures prepared by 3D printing until now, even though three-point bending tests have been applied to study brittle solid biscuits (Kim et al., 2012).

To complement the mechanical analysis, the fracture process can be recorded by a digital camera and analyzed with digital image correlation (DIC). Based on the frame-by-frame image analysis, the DIC algorithm tracks the displacement of a deformed material surface relative to a reference (the undeformed surface) to quantify the material deformation. Previous studies applied the DIC analysis as a complementary method to mechanical texture analysis of surimi and plant-based meat analogue (Park et al., 2023; Schlangen et al., 2023). The results from DIC visualize the strain distribution on the surface of a material, making it an effective method to characterize fracture mechanics of complex food materials such as 3D-printed snack bars.

This study systematically characterizes the fracture mechanics of 3D-printed snack bars as impacted by various infill designs. It should be noted that the infill design is not the only

factor to determine the textural properties of 3D-printed foods. Composition and processing parameters are other known factors that can impact the overall texture of foods, but in the context of 3D food printing, it is hypothesized that the design flexibility can further modulate the texture of foods made of the same composition and processes. To test this hypothesis, pea-based snack bars are 3D-printed into sandwich structures with solid shells and various infill designs, all having the same solid fraction (i.e. the same caloric content). The 3D-printed snack bars are baked and then subjected to 3-point bending tests coupled with DIC to examine their fracture mechanics upon flexure. The obtained fracture mechanics information is related to design parameters such as the infill angle and layer orientation. The insights gained from various measurements are used to modify the infill designs and produce 3D-printed snack bars with a diverse range of flexural properties.

7.2. Materials and methods

7.2.1. Sample preparations

A pea-based formulation was modified from Venkatachalam et al. (2023) as the printing material throughout this study. Insoluble fiber, pregelatinized starch, native starch, and protein were kindly provided by Cosucra (Belgium). To prepare 100 g of the printing material, 13.7 g of insoluble fiber, 12 g native starch, 6.8 g of soluble protein, and 1.7 g of pregelatinized starch were mixed for 1 min using a kitchen mixer (Kenwood Kitchen Mixer, UK). After dry mixing, 65.9 g of water was gradually added to the mixing bowl and mixed for 5 min to produce a consistent paste. The sample is further homogenized and degassed using a vacuum mixer (Thinky Vacuum Mixer ARV-310LED, USA) at a speed of 2000 rpm and a pressure of 30 kPa for 2 min at 20 °C. The sample was then equilibrated at room temperature (20 °C) for 1 hour prior to the 3D printing experiments.

7.2.2. 3D printing and post-processing

The pea-based printing material was loaded into a 200-mL syringe, which was connected to a pneumatic dispenser (Performus, Nordson EFD, USA). The pneumatic dispenser is controlled by a 3-axis precision motion stage (PI, Germany) to perform the extrusion-based 3D food printing. The printing path was designed using 3D printing control software (SPiiPlusSPC, ACS Motion Control, Israel). An overview of the printing designs can be found in Figure 7.1. A cuboid of 60 mm x 10 mm x 10 mm was filled with different rectilinear patterns, of which the infill angles and spacings were varied to create different infill designs

with almost identical extrusion lengths, leading to consistent weights of the 3D-printed samples. The rectilinear pattern was chosen in this study due to its simplicity and high 3D printing accuracy as reported in a previous study (Ma et al., 2023). The infill orientation was also alternated for the samples with infill angles of 30 and 75° to create crossed infill patterns. The alternation was appiled every layer or every other layer to create binary crossed and ternary crossed infill patterns. The designs were 3D-printed in duplicates using a nozzle size of 1.2 mm at 40 mm/s with a layer height of 0.7 mm. Fourteen layers were printed in total, resulting in a design height of 9.8 mm.

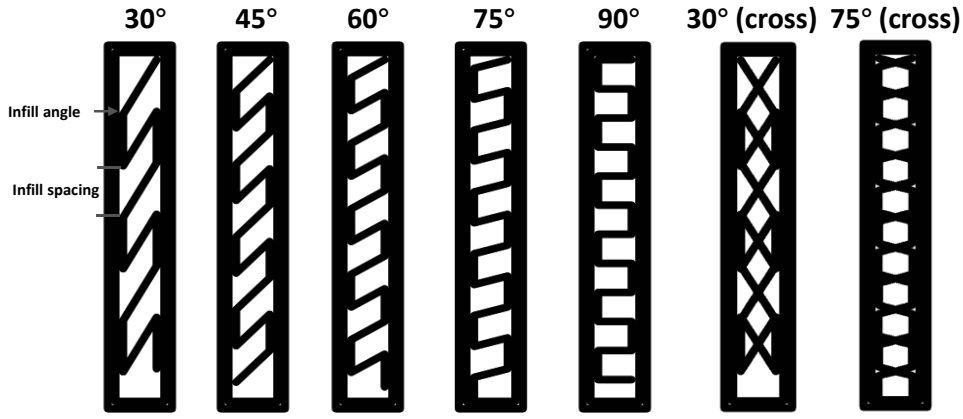

Infill spacing (mm)	Infill angle (°)	Extrusion length (mm)
4.8	90	385
5.1	75	385
5.4	60	384
6	45	384
8.5	30	383

Figure 7.1. An overview of the rectilinear infill designs (60mm x 10 mm x 10 mm): top view of the infill structure, infill spacing, infill angles, and their corresponding extrusion length.

After 3D printing, the samples were frozen at -20 °C for 3 hours and then baked in a convection oven (Leventi, Levens Middleby, the Netherlands) at 140 °C between 15 and 18 min to reach a final moisture content of 25 ± 1%. The baked samples were placed in an air-tight container at room temperature (20 °C) to allow moisture equilibration for at least 12 hours. The moisture-equilibrated samples were then used for further texture and/or x-ray tomographic analysis.

7.2.3. Finite element modelling

Finite element modelling (FEM) was conducted to evaluate the flexural properties of the rectilinear designs used in the 3D food printing experiments. 3D models were drawn based on the 2D designs in Figure 7.1 using SolidWorks (Dassault Systèmes, Vélizy-Villacoublay, France) for FEM simulation of a 3-point bending test. To simulate the 3-point bending test, two support bars and one impactor were assembled with the 3D structure. The support bars have a span of 40 mm and were fixed on one of the solid shell of the design as the displacement boundary. Preliminary experiments showed that a mesh size of 0.5 to 1.5 mm results in mesh size independence. For all simulations, the 3-point bending assembly (3D structure, supports, and impactor) were meshed with a size of 1.2 mm to obtain about 100 000 tetrahedron elements. The impactor was set to deflect a flexure displacement of 2 mm from the center of the top shell of 3D structure. To evaluate the impact of the designs of the structures on their flexural properties, material properties of low density polyethylene (LDPE) were taken as reference. The model was solved using the nonlinear analysis option in SolidWorks in a pseudo-time span of 1 s. In the solved model, the meshes contacting the impactor were selected and the von Mises stress of the meshes was averaged to approximate the flexure stress measured in a three-point bending test. The corresponding displacement of the impactor was recorded to calculate the flexural modulus of each design.

7.2.4. Texture analysis and digital image correlation

The baked samples were subjected to a three-point bending test using a universal testing machine equipped with a 2 000 N load cell (Instron, Illinois, USA). A solid shell side of the sample was placed on the support span (L) of 40 mm, and the impactor flexed the sample from the mid-point of the top shell at a deformation rate of 2 mm/min for a flexure distance of 20 mm. The flexure test was terminated when the load cell measured less than 0.1 N of force or when the impactor travelled the total flexure distance (20 mm). The corresponding force (f) over the flexure distance (y) was recorded to calculate the flexure strain (ε_{Flex}) and stress (σ_{Flex}) using equations 1 and 2 (van Vliet, 2013):

$$\sigma_{Flex} = \frac{3fL}{2wH^2} \qquad \text{eq. 1}$$

$$\varepsilon_{Flex} = \frac{6Hy}{L^2} \qquad \text{eq. 2}$$

Where w is the width (mm) of the cuboid, H is the height (mm) of the rectangular rod.

Prior to the 3-point bending test, the front surface of the sample was spray-painted with black speckles (OK Spuitlak Mat, Wolvega, the Netherlands) for the digital imaging correlation (DIC) analysis. The randomly distributed black speckles enhance the contrast of the DIC analysis. A digital camera (Sony 4 K FDR-AX53) equipped with a Zeiss 2.0/4.4–88 mm lens recorded the 3-point bending process at 25 frames per second. The DIC analysis was then conducted using the recorded videos to visualize the strain deformation on the surface of the 3D-printed samples.

The 3-point bending videos were analyzed with the open-source software "Ncorr2" developed by Blaber et al. (2015). The speckled surface of the sample was selected as the region of interest (ROI), and the software divided the ROI into a virtual grid with subsets. The deformation within each subset was represented by the correlation between the current image and the reference image (i.e. the non-deformed sample). A correlation coefficient was then calculated between the original position of the subset P (x,y) and the deformed position P′ (x′,y′). Based on this approach, all subset movements during the 3-point bending test were calculated using the DIC method. The calculated correlation matrix was then scaled into the distance space, and the flexural deformation of the sample was visualized by plotting the local strains of each subset on a heatmap.

7.2.5. X-ray tomographic analysis

The internal structure of selected 3D-printed samples was analyzed with X-ray microtomography (GE Phoenix v|tome|x m tomographer, General Electric, Wunstorf, Germany). A 240kV micro focus tube with a tungsten target produced X-rays with a voltage of 100 kV and a current of 100 µA. X-ray images were recorded by a GE Dynamic41|200 detector array with 2024 × 2024 pixels (pixel size 200 µm). The samples were placed 117 mm from the X-ray source to obtain a spatial resolution of 30 µm. To avoid beam hardening, a 0.1 mm Cu filter was placed in front of the detector. 2D scans of the sample were performed from the frontal and transversal perspectives to visualize the layer stacking and internal porosity of the 3D-printed samples. The obtained X-ray images were compared to the DIC strain visualizations to gain complementary insights on flexural deformation of the 3D-printed samples.

7.3. Results & Discussions

7.3.1. Flexural properties impacted by infill angles

Finite element modelling (FEM) simulations were first conducted to examine the impact of the infill angles on the flexural properties of the designed structures, using a standard engineering material (i.e. low density polyethylene, LDPE). Figure 7.2A shows the simulated flexure stress over a range of 0.07 flexure strain. To facilitate comparison amongst the designs, the relative flexure stress is reported with the highest flexure stress scaled to 1. It is clear that the infill angle impacts the flexural deformation of the structures. Within the 0.07 strain, the flexural deformation is generally elastic as indicated by the linear relation between the flexural stress and strain. The corresponding flexure modulus of each design is calculated and shown in Figure 7.2B. Normalization is used to highlight the difference among the designs (i.e. the highest flexural modulus was scaled to 1). The sample with 90° infill has the largest flexural modulus in the elastic regime. While variations in flexure moduli are observed among infill angles of 60°, 45°, and 75°, the sample with 30° infill has a much smaller flexural modulus, indicating a weaker structure upon bending. The results from the FEM simulation suggests that even with the same solid fraction, designs with different infill angles lead to variations in flexural behavior in the elastic regime.

Three-point bending tests were performed to experimentally characterize the flexural behavior of 3D-printed snack bars made of different infill angles. Figure 7.2C shows the measured flexure curve with a flexure strain range of 0 to 0.07. In the elastic regime, a similar trend in the flexural moduli is observed between the simulated and the measured results. This agreement shows that FEM simulations are effective to estimate the flexure moduli among different rectilinear infills when designing rigid 3D-printed food structures. A similar conclusion was drawn by Fahmy et al. (2022) who successfully simulated Young's modulus of 3D-printed cereal snacks based on compression tests. According to our simulated relative flexural moduli (Figure 7.2D), an increase of the infill angle perpendicular to the outer shell generally results in a more rigid structure in terms of the flexural modulus. The elastic flexure of the sandwich structure is largely determined by the thickness of the shell and the relative density of the core (Liu et al., 2023). For the printed structures in this study, both the thickness of the shell and the relative density of the core were set to be identical among the infill designs. The differences in elastic flexure therefore come from the

core structure's resistance to the shell flexure. With a 90° infill, the sample's core is structured perpendicular to the shell, creating the largest resistance to flexure upon bending. When the infill angle decreases and the structure becomes more parallel to the shell, the resistance to flexure may weaken, leading to more shell flexure as observed in Figure 7.2.

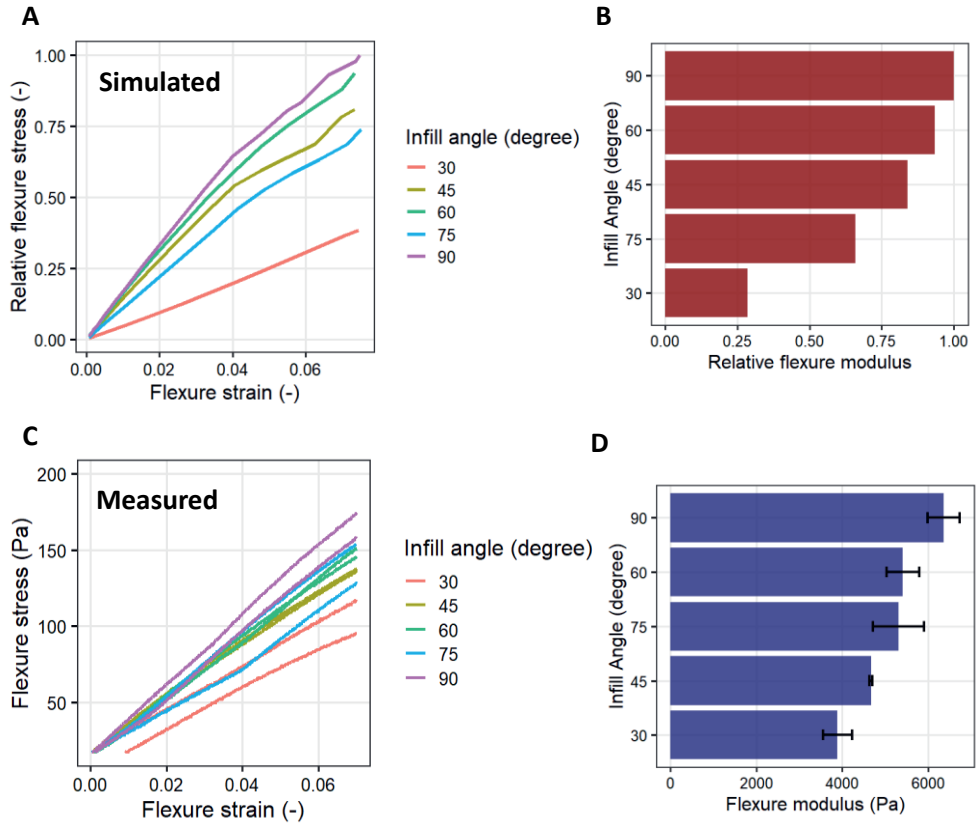

Figure 7.2. A: simulated stress over flexure strain of the designs varied in infill angles. B: relative flexure modulus calculated based on A. C: measured flexure stress over flexure strain (0 to 0.07) based on three-point bending tests (n = 2). D: flexure modulus (Pa) calculated based on the stress-strain curves shown in C, the error bar represents standard deviation from duplicated measurements.

Moreover, the experimentally obtained flexural curve from three-point bending tests provides insights beyond the elastic regime. After the initial linear-elastic response, a non-linear phase is observed where in which the flexure stress gradually approaches a plateau while the with increasing flexure strain continues to increase (Figure 7.3). The final phase of the flexure curve involves a fluctuating falling phase typical of porous structures, where

different elements of the structure fails with a rapid decrease of the overall flexure stress with fluctuations (Liu et al., 2023). Figure 7.3 reveals differences in the maximal flexure stress and failure strain (i.e. largest flexure strain with a stress measurement) of the 3D-printed snack bars. To highlight the differences, Figure 7.4A summarizes the flexural properties into a texture map by plotting the maximal flexure stress against its corresponding strain of bars with varied infill angles. Although with some variations in repetitions, the design with 90° infill is still the most rigid with the highest maximal flexure stress measured, while the design with 30° infill has the lowest maximal flexure stress. Overall, the maximal flexure stress decreases as the infill angle reduces, indicating that the perpendicular core support of the 90° infill gives the most resistance to flexure, similar to what is observed for flexure moduli (Figure 7.2). Although with less rigidity, the 30° infill design shows the most flexural deformation with the largest flexure strain (Figure 7.4A). This indicates the classic strength-deformation trade-off reported by Maldonado-Rosas et al., (2024) and among previous studies in food packaging films (Fabra et al., 2008; Tong et al., 2023). The rectilinear infill structures designed in this study therefore have the potential to modulate the flexural properties of 3D-printed snack bars by adjusting their strength and elongation balance.

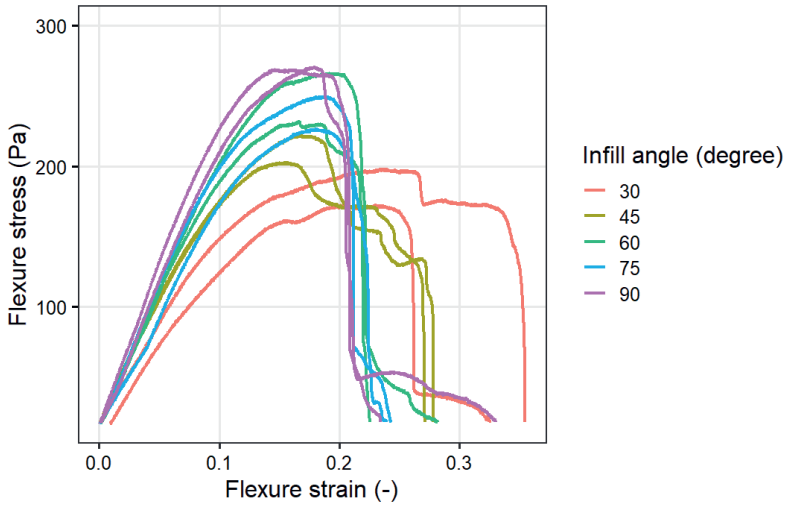

Figure 7.3. Measured flexure stress over flexure strain of the designs varied in infill angles obtained from three-point bending tests (n = 2).

To further characterize the behavior under flexure, Figures 7.4B and C highlight the strain maps of bars made with 30 and 90° infills when reaching the maximal flexure stress, respectively. At maximal flexure stress, strain mostly occurs in the core of the sandwich structure. This is similar to what Liu et al. (2023) reported on composite sandwich structures made of carbon fiber-epoxy resin. The maximal flexure stress is associated with breakage of the infill structure, indicative of core fracture. Although both samples exhibited core fracture, the strain distributions are different between the samples with 30° and 90° infill. Specifically, for the 30° infill design, one side of the structure shows the most strain changes while the rest of the infill structure remains relatively less impacted (Figure 7.4B). When the infill angle is changed to 90°, in Figure 7.4C, the core strain is equally distributed across the infill structure, giving more rigidity against flexure compared to the sample with 30° infill design. The strain distributions confirm the different fracture mechanics measured by the mechanical tests in Figure 7.3.

After reaching the maximal flexure stress, the 3-point bending proceeded until complete failure of the structure. At this failure point, the shell of the structures is completely deformed and all perceivable stress has gone. Figure 7.4D shows that the bar with 90° infill has the lowest elongation and failed at a flexure strain of around 0.23. In general, the elongation increases (i.e. the flexure strain at failure increases) as the design's infill angle decreases. Figure 7.4D confirms the strength-elongation balance mentioned before, indicating that rectilinear infill angles can modulate the overall flexural elongation by compensating the flexural strength. Shell delamination occurs as highlighted by the largest local strain close to the impactor (Figures 7.4E and F). The impactor compressed the top shell of the structure, leading to a severe deformation but no failure of the structure. Failure of the sandwich structures occurs when the bottom shell is tensioned apart, which is a common source of deformation found in 3-point bending tests (van Vliet, 2013). Maldonado-Rosas et al. (2024) also reported that tension from the bottom layer caused 3D-printed cookies to fail during a 3-point bending test. Therefore, reinforcing the bottom shell with higher solid fraction may improve flexure strength of 3D-printed snack bars. Overall, with all samples containing the same solid fraction, changing the rectilinear infill angles can result in different flexural properties of the 3D-printed snack bars. The strength-elongation balance is identified both at fracture and failure points in the 3-point bending tests, and the flexural properties can be potentially modulated by changing the infill angles to create either

elongated but soft samples (e.g. 30° infill angle) or strong but brittle samples (e.g. 75 and 90° infill angle).

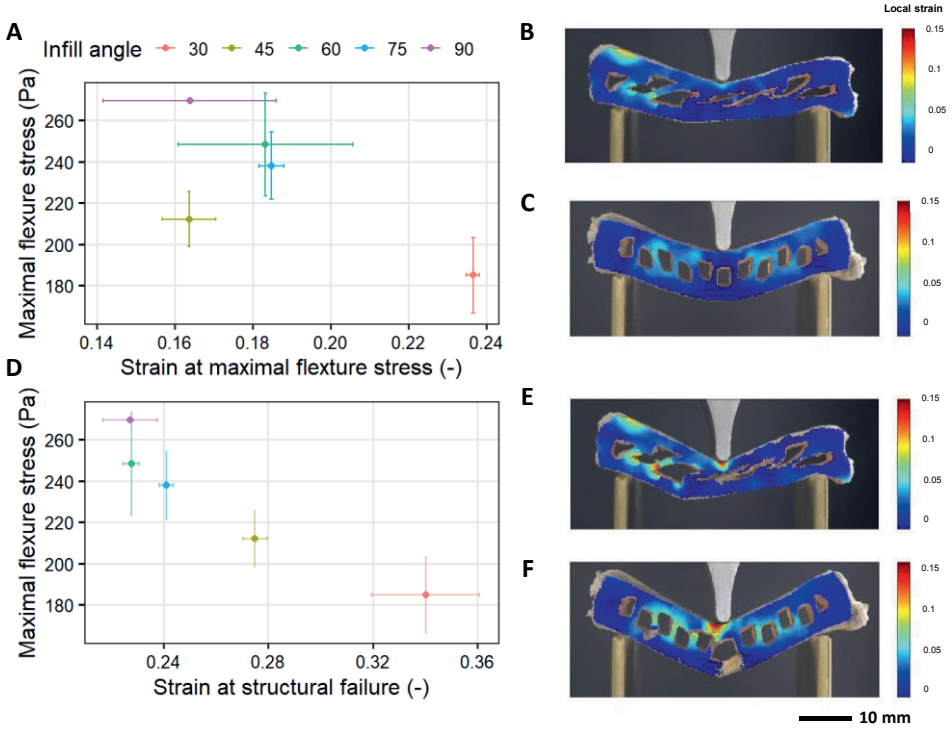

Figure 7.4. A: texture map (fracture strain vs fracture stress) of 3D-printed samples varied in infill angles. B: DIC strain map of a 3D-printed sample with 30° infill angle at fracture point. C: DIC strain map of a 3D-printed sample with 90° infill angle at fracture point. D: texture map (failure strain vs fracture stress) of 3D-printed samples varied in infill angles. E: DIC strain map of a 3D-printed sample with 30 ° infill angle at failure point. F: DIC strain map of a 3D-printed sample with 90 ° infill angle at failure point. The heatmap represents the strain changes with respect to the undeformed image of each sample.

7.3.2. Flexural properties impacted by layer orientations

Another parameter to consider when designing rectilinear infill is the layer orientation. In 3D-printing applications, it is common to alternate orientations among different layers to create crossed structures as reinforcement. In this section, we examined 2 types of crossing, a binary cross (i.e. alternating every other layer) and a ternary cross (i.e. alternating every 2 layers). The FEM-simulated results are first shown in Figures 7.5A and B. Alternating the layers improved the overall strength of the structure compared to the uniformly stacked layers for both samples with 30 and 75° infill. However, the trend from FEM (Figure 7.5A and B) did not agree with the measured flexural curve (Figure 7.5C and D). In the three-

point tests, similar flexure progression in the near-linear regime was observed between the crossed and uniformly stacked samples, and no clear flexure strength improvement among the crossed structures. Figure 7.5D reveals that the flexure moduli are comparable among structures with the same infill angle: the differences in flexure moduli between the 30 and 75° infill designs exist regardless the differences in layer orientation. The mismatch between the simulated results using model material and the experimental results of the 3D-printed snack bars can be expected. The FEM simulation assumed ideal 3D printing performance with a perfect structure build-up, whereas the actual 3D printing of the snack bars is prone to structuring defects. Further structure analysis is needed to reveal the inner structure of the 3D-printed snack bars with crossed infill designs.

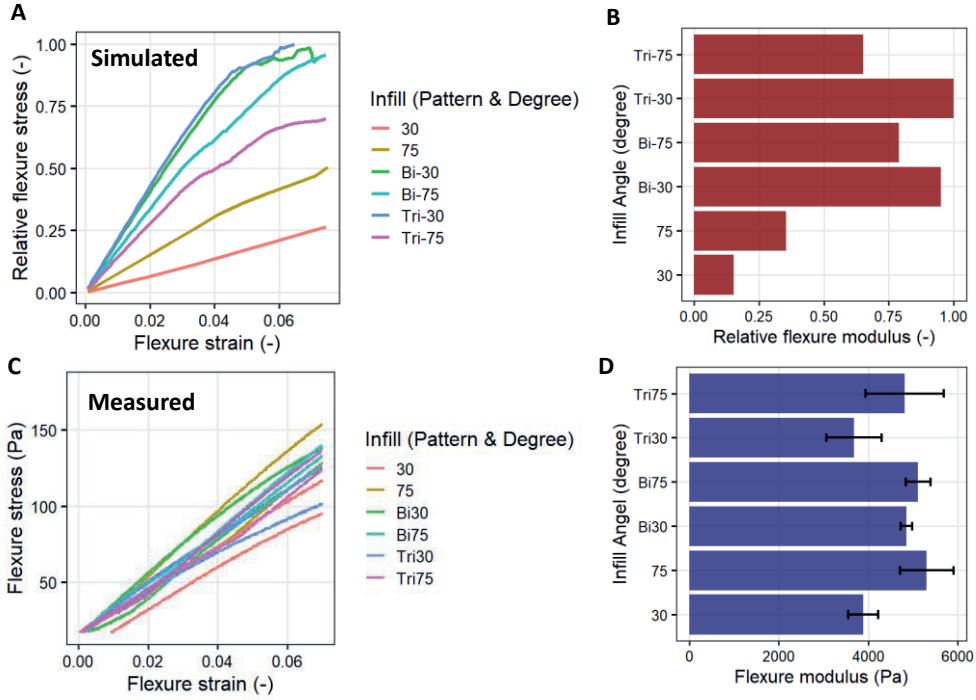

Figure 7.5. A: simulated stress over flexure distance of the designs varied in infill angle orientations (Bi: binary alternation, Tri: ternary alternation). B: relative flexure modulus calculated based on A. C: measured flexure stress over flexure strain (0 to 0.07) based on three-point bending tests. D: flexure modulus (Pa) calculated based on B.

Figure 7.6 reveals that the entire three-point bending measurements of designs varied in infill angle orientations. Layer orientation did not impact the fracture and failure behaviors

of the 3D-printed snacks, whereas some differences are observed between the 30 and 75° infill designs. To further examine the flexural property difference, Figure 7.7A shows a texture map comparing the maximal flexure stress of the crossed and stacked designs. Alternating the layer orientation resulted in no significant difference ($P < 0.05$) in terms of maximal flexure stress. The differences in flexure properties still originate from the infill angle difference (i.e. 30 vs 75°). Designs with 30° infill angle were more deformable and less rigid compared to the ones made with 75° infill, similar to what was observed in Figure 7.4. When considering structural failure points, a similar trend is observed in Figure 7.7B: designs with 30° infill have larger shell elongation as compared to the samples made with 75° infill. The results from 3-point bending tests further confirm that the crossed infill designs do not have improved flexural properties compared to other structures assessed in this study.

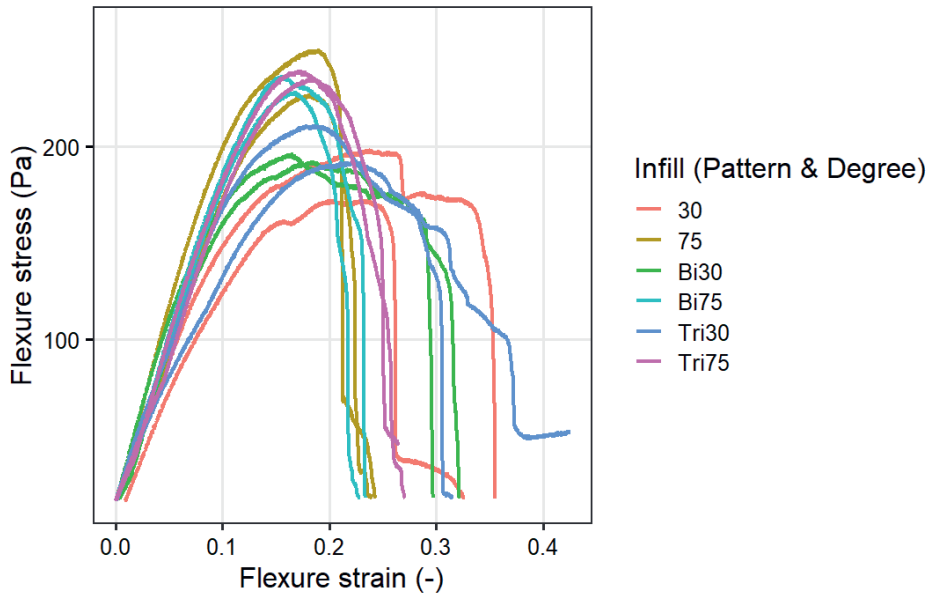

Figure 7.6. Measured flexure stress over flexure strain of the designs varied in infill angle orientations obtained from three-point bending tests (n = 2).

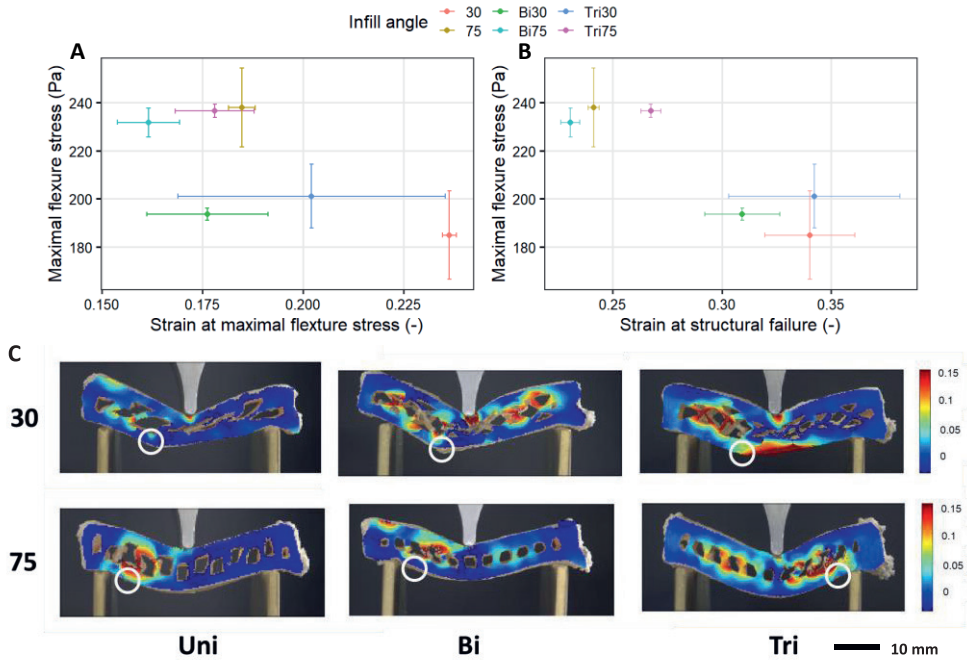

Figure 7.7. A: texture map (fracture strain vs fracture stress) of 3D-printed samples varied in infill angle orientations (Bi: binary alternation, Tri: ternary alternation). B: texture map (failure strain vs fracture stress) of 3D-printed samples varied in infill angle orientations. C: DIC strain maps of 3D-printed samples varied in infill angle orientations at failure point. The right circles indicate the failure positions on each sample.

The DIC analysis visualizes the strain distribution of stacked and crossed structures at failure (Figure 7.7C). The failure pattern is similar across the designs with 30° infill, as indicated by the red circles on the Figure 7.7C. Even though the impactor indented and compressed the top shell with large deformation, the failure of the structure still originates from the tensioned bottom layer. Among the designs with 75° infill, the failure strain maps are also similar, with one side of the inner structure having the most strain changes. The shell delamination again occurs at the bottom, showing a consistent shell failure mechanism. Overall, the DIC strain maps agree with the mechanical measurements showing minimal difference in fracture mechanics between the stacked and crossed samples. The primary difference in fracture mechanics may be caused by the infill angle of the rectilinear designs rather than the layer orientations. Our results also suggest that crossed rectilinear structures do not improve flexural strength, and that layer orientation is an ineffective parameter to modulate the texture for 3D-printed snack bars.

The observations made are counterintuitive and against the common insight that triangle shapes reinforce the flexure strength of beam structures (Deshpande & Fleck, 2001). A possible reason for this disagreement is inadequate fabrication of the crossed structure using 3D food printing. Since 3D food printing builds a structure layer-by-layer, the infill layer crosses are made by suspending food materials over the previously printed layer. The pea-based paste used in this study may be insufficiently capable of achieving overhanging, and without proper overhanging, the printed layer can fall onto the previous layer, resulting in local collapse preventing proper formation of crossed structures. Figure 7.8 shows an X-ray image of the stacked and crossed samples made with 30 and 75° infill. In Figure 7.8A, the transversal scan reveals a uniformly stacked infill structure (30°) with minimal cavities. However, when the layers are crossed, cavities and curved filaments (as pointed by the red arrows) can be observed in Figures 7.8B and C. These cavities and curved filaments can be caused by undesired collapses that occurred during the 3D-printing and baking process. A similar inner structural trend is found in samples made with 75 ° infill with cavities and inconsistent layer fusion in the crossed structure (Figures 7.8E and F). Compared to the uniformly stacked samples, the crossed samples also suffer from poor layer fusion. Layer fusion is a known challenge of 3D food printing, as most food materials do not go through an active fusion process similar to melting and solidification of thermoplastics. Without proper layer fusion, the crossed structure cannot be regarded as uniform. Instead, some interface between the layers should be included when simulating the flexure process. The FEM simulation made in this study ignores any local collapse or poor layer fusion, which can explain the disagreement observed between the simulated and measured results. In summary, mechanical texture analysis, DIC analysis, and X-ray tomography confirm that 3D-printed snack bars made from a pea-based paste cannot fabricate crossed structures with proper fusion and intact triangle supports.

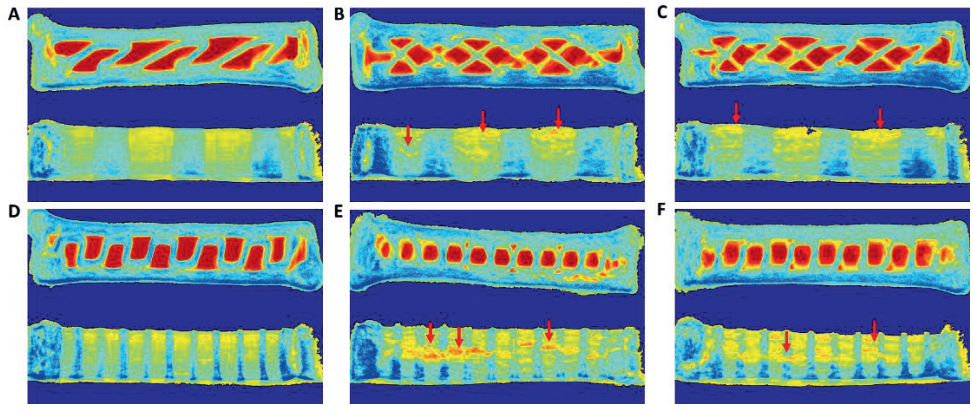

Figure 7.8. Frontal (top) and transversal (bottom) X-ray scans of no-alternation at 30° infill angle (A), binary alternation at 30° infill angle (B), ternary alternation at 30° infill angle (C), no-alternation at 75° infill angle (D), binary alternation at 75° infill angle (E), ternary alternation at 75° infill angle (F). The red arrows indicate the cavities and improper overhangs.

7.3.3. Modifying infill designs to modulate flexural properties

After understanding the fracture mechanics of 3D-printed snack bars during a 3-point bending test, the 75° rectilinear infill design was modified to alter its flexural properties based on the visualized strain fields shown in section 3.1. The uniformly stacked 75° rectilinear infill design showed high flexural strength, but less elongation based on the 3-point bending test (Figure 7.4). The near-perpendicular infill structure provides rigid support to the shell when deformed by the impactor. To improve flexural elongation, the modified design removes a support core in the middle of the structure but includes additional shell thickness (Figure 7.9A). This infill design change maintains the overall solid fraction of the structure, while it improves the elongation of the shell reducing the core support structure. Figure 7.9B compares the flexural properties between the original and modified designs. Overall, the modified structure had lower maximal flexure stress compared to the original design, while having a larger elongation upon bending. This is again an elongation-strength trade-off demonstrated by a simple change of the infill design. When comparing the modified design with the original stacked designs, Figure 7.9C shows that a weakened core support at the bending position reduces the flexural strength, and fracture may have occurred when the impactor punctured the top shell of the modified structure. After reaching the maximal flexure stress, Figure 7.9B shows an irregular decrease of the flexure stress after reaching the maximal stress, indicating sequential fracture of the top and bottom shells. This fracture

behavior leads to more elongation during the 3-point bending test, as shown by the large flexure strain at failure in Figure 7.9D. In terms of the failure mechanics, the modified 75° infill design is very similar to the original 30° infill design with a low flexure strength and a high elongation. This design change demonstrates how a simple change in structure design can result in a large difference in flexure properties of 3D-printed snack bars. We can thus create a specific modification of the infill design, by systematically characterizing the fracture mechanics of 3D-printed snack bars. These insights will allow us to create food products with a diverse range of flexural properties.

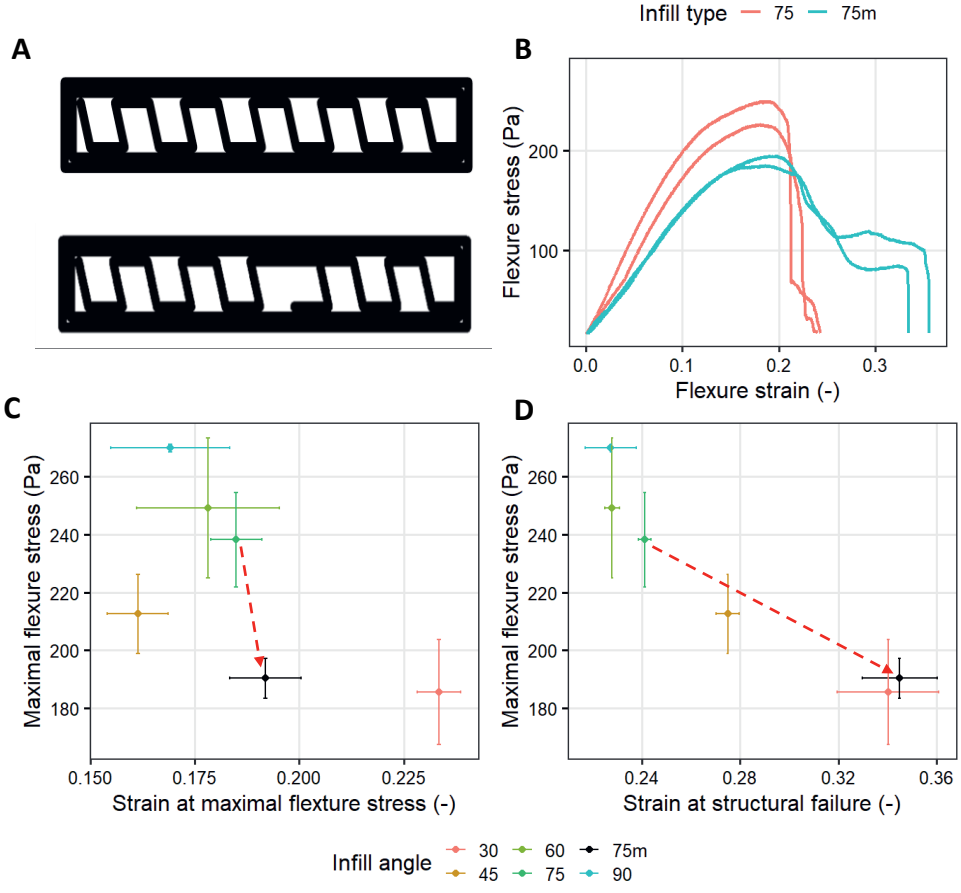

Figure 7.9. A: original (top) and modified (bottom) 75° infill design. B: measured flexure stress over flexure strain of original (75) and modified (75m) infill structures. C: texture map (fracture strain vs fracture stress) of original (75) and modified (75m) infill structures. D: texture map (failure strain vs fracture stress) of original (75) and modified (75m) infill structures.

This design modification was based on the observations with the DIC strain visualization of the 3D-printed snacks shown in previous sections. While the mechanical texture analysis measures the overall strength and elongation, the strain visualization provides additional information about the local deformation and failure of a given structure. Understanding localized deformation is especially helpful in 3D food printing applications as this technology can quickly adapt food structures. The visualized strain fields provide feedback to food structure designs, which can guide structural optimizations to modulate food textures. The vision-guided design modifications can be potentially extended to other food structuring applications. For example, Schlangen et al. (2023) applied tensile tests coupled with DIC to visualize and understand anisotropic structures in plant-based meat analogues. The obtained visualized deformation data can potentially direct future formulation and processing parameter optimizations when producing meat analogue products. With low-cost video cameras and open-source analysis software available, combining mechanical texture analysis with DIC becomes a feasible option for food science researchers to comprehensively modulate and adapt the mechanical properties of food structures.

7.4. Conclusions

This study systematically characterized the flexural properties of 3D-printed snack bars made with various infill designs. With a constant solid fraction and the same post-processing parameters, the infill angle of a 3D-printed structure can impact its flexural properties and result in a specific strength-elongation balance.

Flexural strength can be improved by changing the infill angle perpendicular to the outer shell to provide more core support, while an infill angle more parallel to the outer shell improves the structure's flexural elongation. Creating crossed layer structures has minimal impact on the overall flexural properties due to poor layer fusion and insufficient overhanging of the pea-based printing material. The flexural deformation process is visualized by digital image correlation (DIC), which highlights the local strain changes during the 3-point bending test.

The visualized fracture mechanics can guide the modification of the infill design to optimize the flexural properties of 3D-printed snack bars. For future research, the structures characterized by mechanical tests can be further evaluated through sensory panels to

understand texture perceptions induced by 3D-printed snack bars. A thorough understanding of how the 3D structure design modulates the food texture may accelerate the development of personalized foods and will help to mature 3D food printing into a consumer-ready technology.

Chapter 8 General discussion

8.1. Introduction

3D food printing as an emerging technique can enable customized food designs, modify sensorial properties, and tailor to specific nutritional values based on individual's preference. Consuming these personalized foods can bring additional sensory enjoyment, fulfill dietary needs, and potentially improve the wellness of specific individuals. To produce personalized foods, 3D food printing needs to fabricate food structures in a timely and accurate manner. This thesis aimed to develop monitoring, evaluation, and optimization strategies to effectively produce 3D-printed foods with complex food ingredients. Through machine vision and predictive modelling, a set of digital methods was developed and demonstrated to improve the current 3D food printing performance. This chapter first summarizes the findings and solutions developed in this thesis. The discussion continues with a general control strategy to synchronize material flow and nozzle motion of 3D food printing and a set of guidelines for digitally optimizing complex food processes. Some directions for future research are suggested towards the end of this chapter.

8.2. Optimizing 3D food printing one dimension at a time

This thesis begins with a review of the current development of 3D food printing for personal food production (**Chapter 2**). A common strategy to control the texture of 3D-printed foods is to alter the infill density and patterns of food structures. The spatial distributions of ingredients can also impact flavor perceptions in 3D-printed foods. After reviewing the current literature of 3D food printing, chapter 2 concluded that longitudinal consumer insights of 3D food printing are still needed. In addition, from an engineering perspective, robust 3D printers should be developed to produce personalized foods timely and accurately. Various strategies to improve the 3D printing performance of foods based on machine vision technologies were then studied.

In **Chapter 3**, an extrudability assessment tool was designed for rapidly and automatically screening potential food printing materials. The experimental data suggested that the extrusion flow rate and printing pressure can characterize the shear-thinning behavior of complex food materials. The line extrudability of various food materials was successfully predicted using data-driven models, using a dataset of food printing materials with diverse rheological properties. Such an approach of combining experimental data with theoretical

models (known as gray-box modelling) was effective to determine the optimal parameter settings for complex food processes such as extrusion-based 3D food printing. **Chapter 4** demonstrated the development of a computer vision system to continuously measure the extrusion rate and filament width during 3D food printing. The nozzle motion was then optimized for the extrusion rate and the die-swell ratio of the food materials, to improve the layer deposition and 3D-stacking of food structures. This method is modular and simple to be implemented on existing 3D food printers and can significantly improve the printing accuracy of food printing materials with different rheological properties.

Monitoring and assessing 3D-printed structures were subsequently achieved using an infrared (IR) camera (**Chapter 5**). Thermography can quantitatively assess the stability of printed foods during hot-extrusion 3D printing. A critical surface temperature was identified as the temperature above which the printed structure collapses during 3D food printing. The observed critical surface temperature was linked to the sol-gel transition temperature that was measured with independent rheological tests. Insufficient cooling and extended printing times can cause instability in the printed food structure during 3D food printing. In addition, developing a yield stress upon cooling is necessary for obtaining a stable food structure.

Not only should a 3D-printed structure be stable, it also needs to accurately resemble the intended digital design. In **Chapter 6**, a contextualized, automated, layer-wise image analysis method was developed and validated to quantify the 3D printing accuracy of foods. Automated and manual evaluations both indicated over-extrusion as the primary source of inaccurate printing, but consistent under-extrusion was not perceived as inaccurate by human evaluators. The automated assessment tool can therefore guide corrective actions to improve 3D food printing accuracy by minimizing over-extrusion.

After achieving good printing accuracy, the final research chapter (**Chapter 7**) of this thesis demonstrated the use of digital design to tune the texture of 3D-printed foods with the digital design. Changing the infill designs of 3D-printed foods can impact the mechanical properties. Combined with digital image correlation, the fracture mechanics of 3D-printed snack bars were visualized and contextualized with strain-stress curves. This chapter

exemplifies how food structure designs can create targeted texture profiles made from the same food material.

From one-dimensional optimization of material flow to 3-dimensional optimization of textural properties, this thesis thus demonstrates that a combination of machine vision and use of predictive models can monitor, evaluate, and optimize 3D printing of complex food systems for improved printing results.

8.3. Synchronizing material flow and printing motion

Extrusion-based 3D food printing fabricates structures using a layer-by-layer approach, so its 3D printing accuracy relies on the accuracy in layer printing. On a typical 3D food printer, one or multiple printheads are attached to a 3-axis mechanical platform to print layers of food materials in the 3D space. The printhead is responsible for generating a proper food material flow, while the mechanical platform creates the corresponding motions to deposit the materials onto the correct target positions. To achieve a good layer printing accuracy, the flow rate of the food material needs to be synchronized with the printing speed of the nozzle (Figure 8.1). Any mismatch of the flow and motion results in printing defects such as over and/or under extrusion.

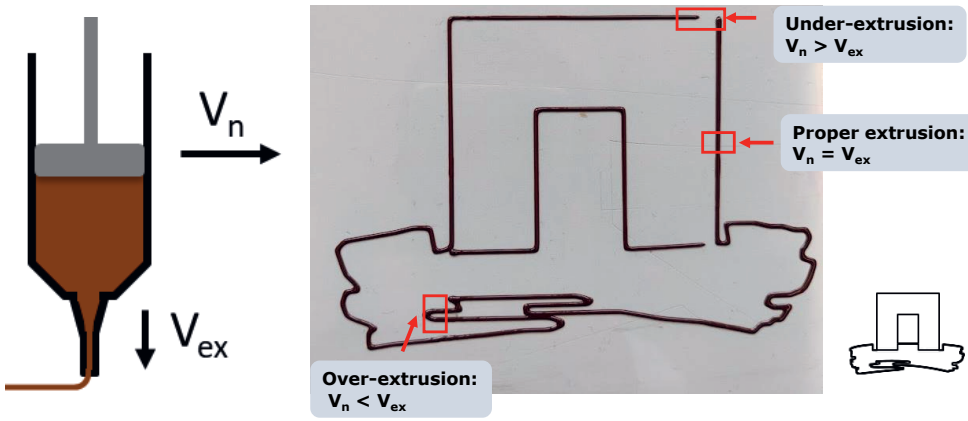

Figure 8.1. Flow-motion harmony: a demonstration of the flow rate (V_{ex}) and printing speed (V_n) and how they can impact layer printing accuracy during extrusion-based 3D food printing.

Since most food printing materials are shear thinning, controlling the material flow is challenging due to the nonlinear relation between the extrusion pressure and material flow

rate. **Chapters 3 and 4** showed that the rheological properties and the instant material flow rates impact the overall extrudability and line printing accuracy of various food materials. During 3D food printing, material flow is interrupted by non-printing motion (i.e. the platform needs to move to a certain position prior to material deposition), meaning that the printhead needs to rapidly stop and resume the material flow during multiple times in a printing job. Printing inaccuracies were found to be often associated with these start-stop points when making non-printing movements (**Chapter 5**). The rapid changes in flow rate are especially difficult to control and optimize considering the complex flow behavior of the materials. To accurately synchronize material flow and printing motion, the current practice involves manual trial and error experiments to calibrate system parameters such as the speed of retraction, the level of extrusion multiplier, and priming the printhead with pre-printing extrusion to alleviate the impact of flow inconsistency on printing accuracy. A digital calibration method was proposed in **Chapter 4** to adapt the printhead acceleration profiles based on the observed flow rate increase. Food material flow is further impacted by material compression inside the syringe. While most pure food materials are incompressible, air is often included in printing materials in practical situations, and this leads to compressibility of the overall material. Air incorporation occurs at random, and therefore can result in varying compressibility of the same material, making it very difficult to model this compressibility issue. Therefore, in practice, proper degassing steps such as vacuum centrifugation are often required to standardize the printing material prior to 3D food printing.

While controlling the complex food material flow is very important for achieving proper layer printing accuracy, one should also consider the mechanical motion of the printing platform. The mechanical platforms commonly found in 3D food printers are made of 3 linear actuators, each responsible for one axial motion in the Cartesian vector space (X, Y, Z) (Go et al., 2017). Each axial motion has certain limits in velocity, acceleration and jerk based on the torque generated by the associated stepper motor. When the printing motion involves a curved path, a bi-axial movement is required (i.e. one axis needs to decelerate, while the other axis accelerates to the target printing velocity). Variation in motion can result in an inconsistent velocity profile of the printhead. Figure 8.2 demonstrates that, with a constant platform acceleration, the variation in the momentary velocity increases as the target velocity increases from 20 to 60 mm/s. The disturbance of the velocity is observed

especially at each turn of the "M" path. The severe variations in instant printing speeds shown at 60 mm/s indicate that this speed is beyond the mechanical limit of properly printing the designed "M" shape. Therefore, mechanical engineers have devoted efforts into motion planning and trajectory optimization to maintain consistent motion velocity during 3D printing. For example, Comminal et al. (2019) developed a numerical simulation approach to smooth corners and avoid corner rounding and swelling during thermoplastic 3D printing. Some of the path planning optimization algorithms are available in commercial slicer software to minimize non-printing travel (i.e. fewer start-stop points), round corners, and adaptively slice the layer height to mitigate impacts from mechanical limitations. From a hardware perspective, upgrading the motion platform with servo motors and higher torque limits can also improve printing accuracy caused by poor motion performance (Go & Hart, 2017). One should note however that there is a balance between the hardware capacity and the required printing accuracy needed for specific applications: improving food printing accuracy may not always add to the consumer-perceived accuracy as found in **Chapter 6**.

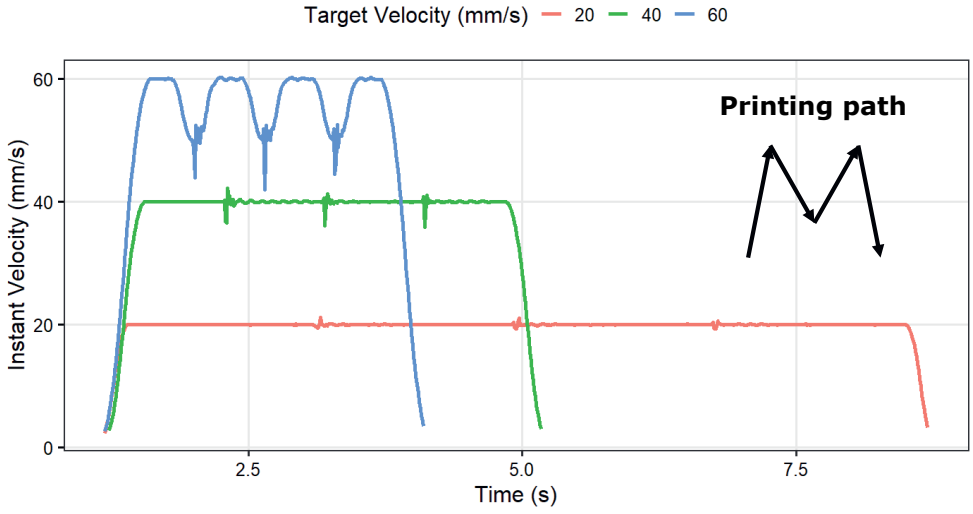

Figure 8.2. Instant velocity over time when printing an "M" shaped path with target velocities of 20, 40, and 60 mm/s using a precision motion stage from Physik Instrumente. The instant velocity data were scoped from a motion controller (ACS, Israel) at 100 Hz.

Overall, flow-motion synchronization is essential for good layer printing accuracy, and this involves both proper understanding and control of the material rheology and using robust

mechanical hardware. Inconsistencies from material flow are caused by material properties, extrusion delays, and material compressibility due to air inclusions. Flow calibration is therefore needed to achieve near-constant material flow. Unsynchronized flow and motion can also stem from mechanical limitations of the printing platform. Proper motion planning algorithms and robust printing platforms with high torque and servo-drive motors can alleviate some defects induced by such improper mechanical motions. With a well synchronized combination of material flow and printing motion, one can expect significantly improved overall 3D food printing accuracy.

8.4. Digital optimization of complex food processes

While extrusion-based 3D food printing was the object of study throughout this thesis, it is only one instance of a wide range of food processing unit operations. Many of the solutions developed in this thesis may be transferred to other food processes. The current practice of digitally optimizing food processes generally involves rapidly measuring parameters of interest and using predictive models to guide their control. With (near) real-time measurement of parameters, control algorithms (either closed-loop or open-loop) can continually adjust control parameters to maintain the production consistency and achieve the target product quality. In this thesis, **Chapter 4** demonstrated the use of feedforward optimization to improve the extrusion accuracy of 3D food printing. Because a computer vision measurement can estimate the extrusion flow rate near-real-time, a control algorithm can be relatively simple by adjusting the corresponding printing acceleration profiles. Similarly, in **Chapter 5**, deformation of 3D-printed food structures was characterized with thermographic measurements. Even though the real-time control loop was not implemented in that study, straightforward control actions can be implemented such as simply stopping the printing motion to allow enough cooling time for a freshly printed material. The cases shown in **Chapters 4 and 5** illustrate that a direct measurement of key parameters can be used for simple and effective control of the 3D food printing process in near real-time. Other ways of sensing such as spectroscopy, ultrasound, and in-line rheometry also have been integrated into various food processing plants for process control purposes (Grassi & Alamprese, 2018). Integration of sensors into a process may however disrupt the existing process setup and lead to practical difficulties for cleaning and maintenance. Therefore,

future development of sensors should be modular and generalizable to adapt to a wide range of available food processes.

By using sensor data, one can simulate a given food process and optimize processing parameters using multiphysics and/or data-driven models. Multiphysics simulations (also known as "white-box models") are useful for virtually optimizing designs of food processing equipment (Datta, 2008). By changing and optimizing the physical dimensions and processing capabilities in the simulations, designs can be refined before physically building the equipment. These models require many physical properties as inputs to achieve accurate simulations. Finding these parameters often requires specialized analytical equipment, which may not always be feasible for emerging food processes like 3D food printing, which is designed to work with a set of diverse materials, and in diverse settings; for example in consumer's homes.

Another modelling approach is data-driven modelling (also known as "black box models") which computationally derives relationships between input and output variables from large datasets. Black box models mainly focus on interpolation of observations made in training datasets, so they often cannot extrapolate well, when there is only a small amount of observations available. In reality, assembling sufficient datasets poses a challenge, especially within a single food production plant. Meanwhile, these black box models can be difficult to interpret and explain, which may lead to trust issues among operators. Therefore, combining white-box and black-box modeling into "grey-box modelling" can alleviate the tradeoff between the model interpretability and data availability when modelling food processes. **Chapter 3** demonstrated a grey-box approach to predict the extrudability by simplifying complex material flows while leveraging existing physical models to improve the prediction efficiency and ensure that the optimized parameter set is physically sounding. This modelling synergy improves its flexibility and interpretability. Implementing grey-box models requires digitized, automated data collection and well-structured databases. For example, the image-based tool presented in **Chapter 3** enables rapid data collection, and the tabulated data can then directly be used to train machine learning models over time. While the predictability of the extrudability is relatively simple, this approach can be readily adapted to optimize other large-scale food production processes with careful data curation.

An often overlooked aspect in digital optimization is context. Context provides the background of the specific process and the practical significance for the final product. Validating digital methods based on industry and consumer perspectives ensures successful optimization strategies. For example, in **Chapter 6** validated 3D printing accuracy measurements based on feedback from human evaluators. Establishing this context transformed the defect measures into actionable improvements. Similarly, in a different study, the authors validated an image-based method to evaluate the fibrousness in plant-based meat analogues (Ma et al., 2023). An automated image analysis method was first developed by segmentation and skeletonization to analyze fiber morphology (Figure 8.3). An expert panel subsequently contextualized the digital scores of the fibrousness ratings and improved the interpretability of the method outputs. When designing new digital methods, considering the context establishes measurement tolerance, corrective actions, and communication to users.

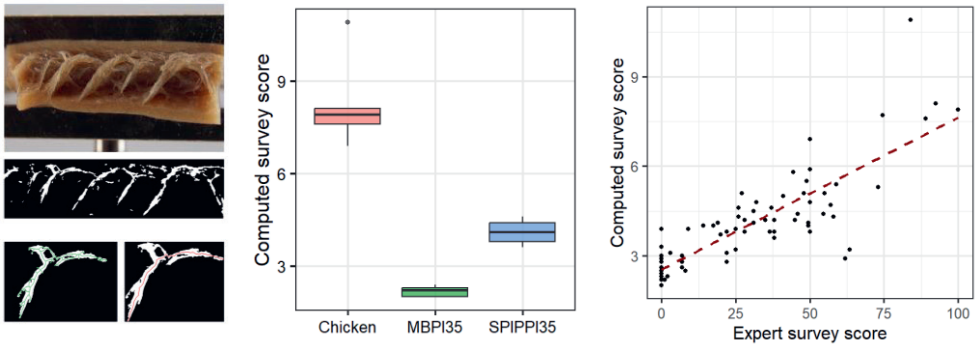

Figure 8.3. Example of contextualizing digital measurements of fibrousness of plant-based meat analogues based on expert-rated fiber scores. MBPI = mung bean protein isolate, SPI = soy protein isolate, PPI = pea protein isolate.

8.5. Future outlook towards digitized food processing

This thesis demonstrated several digital optimization strategies to monitor and control extrusion-based 3D food printing process. The current work in digital optimization can be extended into other types of food processes such as shear cell technology, high-moisture extrusion cooking, and membrane processing. A key area for future research is to implement closed-loop control strategies to deploy these digital methods in production settings. Although open-loop demonstrations were provided in **Chapters 4 & 6**, the

detection and control steps were not yet automatically linked. Similarly, the structural deformation observed in **Chapter 5** were not connected to the 3D printer's controller to make any corrective actions. Similar closed-loop controls have been developed and demonstrated in thermoplastic 3D printing: commercial 3D printers were modified to implement machine vision-based defect detection and corrective actions (A. L. Petsiuk & Pearce, 2020; A. Petsiuk & Pearce, 2022). Due to the variation in the properties of food printing material, implementing a closed-loop control may require further development of 3D printer control algorithms, as previously discussed regarding the importance of synchronizing material flow and printing motion.

Innovation in control algorithms can further accelerate the adoption of digital methods developed in this thesis for commercial, ready-to-use 3D food printers. Figure 8.4 shows a proposed 3D food printing system with various controllers and database integrated. The calibration or open-loop controllers serve as the parameter optimizer at the pre-printing stage. An extrusion test powered by computer vision algorithms (**Chapter 3**) can inform the 3D food printer's initial parameter settings for printing speed, nozzle accelerations, extrusion latency, and retraction distance. During the 3D printing process, a dual camera machine vision controller can monitor the printed object height and layer accuracy in real time. Based on the feedback from layer height and accuracy, parameters such as printing speed, layer height, retraction distance can be modified in real-time to maximize the final 3D printing accuracy. The last element in this system is the accumulation of monitoring data that can be used for model predictive control and guide printing material optimization. The obtained monitoring and evaluation data are labelled with the printing material and parameter details for future modelling purposes.

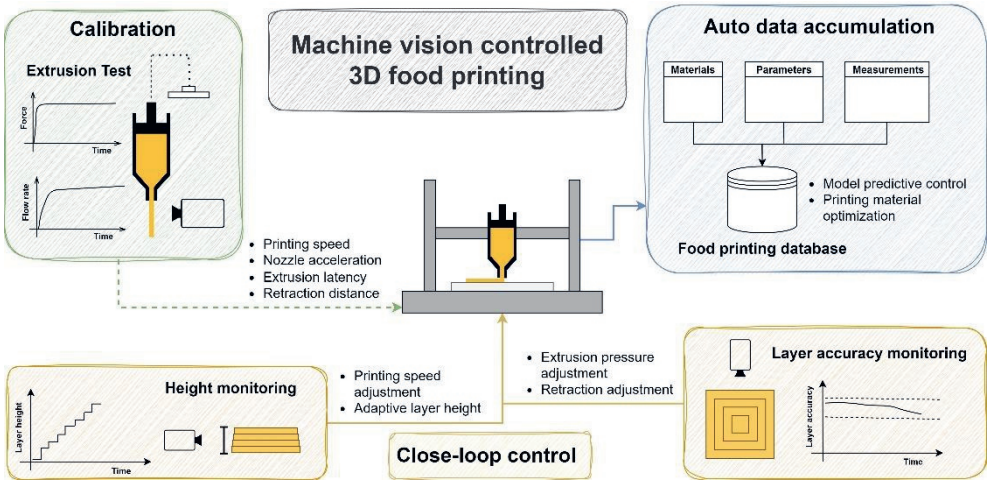

Figure 8.4. An extrusion-based 3D food printing system integrated with vision controllers and a responsive database.

With proper control methods implemented, one can expect to have better reliability and robustness in building complex and stable food structures using 3D food printing. The applications of 3D food printing have been explored and discussed in **Chapter 2**. The printing resolution, structure integrity, and manufacturing speed can be improved with digital optimization. As a robust structuring tool, 3D food printing can potentially create food products with tailored sensory properties as requested by individual users. **Chapter 7** demonstrated an example of modulating the food texture by only changing the infill structure using a well-controlled 3D food printer. This chapter provided an initial case of testing the true design feasibility of 3D-printed foods and their applications to create innovative food products. With digital optimization implemented (Figure 8.4), 3D food printing can efficiently produce repeatable and true-to-design food structures with a variety of materials. However, the concept still needs further contextualization by more consumer-based studies to validate the concept of food personalization and the potential application of 3D food printer as a viable tool to create personalized foods.

The concept of digital optimization can be extended to other types of food processing operations. This thesis chose 3D food printing as a demonstrative process due to its small physical scale and production flexibility. However, food operations across the food production chain have been working towards digitalization. Some of the work in this thesis

was inspired by the successful application of digital technologies in the post-harvest field (Marvin et al., 2022; Verboven et al., 2020). The integration of spectroscopic imaging, x-ray scans, and digital twins has proven to be viable for post-harvest sorting, fruit/vegetable defect analysis, and supply chain optimization. Some studies are now also focusing on digitally optimizing food processes. For example, a recently filed patent by Ho et al. (2023) outlined a control scheme based on machine learning for meat analogue production. Overall, for food processing, the current efforts devoted into digitalization could be more systematic. Even though grey-box modelling for dairy production was mentioned by Roupas in 2008, the detailed actions are still not very clear to optimize food processes using digital technologies. A combination of technological advancements (reliable, cheap, and easy-to-use sensors) and data curation strategies (well-structured and system-wise integrated database) is still needed to achieve digital optimization beyond 3D food printing.

8.6. Concluding remarks

3D food printing is a suitable technology to produce personalized foods that fulfill the nutritional requirements and preferences of individual consumers. This thesis demonstrated the feasibility of applying digital methods to monitor, evaluate, and optimize 3D food printing. Several applications based on machine vision techniques and grey-box modelling principles were demonstrated to improve the line extrudability, structural stability, and design flexibility of 3D-printed foods. The optimized 3D food printing showed improvements in terms of 3D printing accuracy and stability of a wide range of complex food materials. By connecting the studies together, this thesis suggests that material flow and printing motion should be synchronized to each other to ensure high printing accuracy. Rapid measurements and predictive models can be combined to form hybrid models (grey-box models) and should be well contextualized to provide meaningful and actionable optimizations.

Such a digitized system will enable on-demand personalized food production with different types of printing materials and designs. Timely and accurately printed personalized foods can lead to healthier diets based on specific nutritional needs, while the food customizations can bring happiness and additional enjoyment to consumers. It is also possible to adapt the findings for 3D printing to the digital optimization of other food processes, by combining sensor integration and predictive models to establish control. As digital technologies become further integrated into the food production chain, the industry can expect more

efficient and robust production systems, reduced trial-and-error experiments, and improved time and labor management to prepare us for a more sustainable next-generation of food processing.

References

Agarwal, D., Wallace, A., Kim, E. H. J., Wadamori, Y., Feng, L., Hedderley, D., & Morgenstern, M. P. (2022). Rheological, structural and textural characteristics of 3D-printed and conventionally-produced gluten-free snack made with chickpea and lupin flour. Future Foods, 5, 100134. https://doi.org/10.1016/j.fufo.2022.100134

Ahmed, J. (2017). Chapter 9—Time–Temperature Superposition Principle and its Application to Biopolymer and Food Rheology. In J. Ahmed, P. Ptaszek, & S. Basu (Eds.), Advances in Food Rheology and Its Applications (pp. 209–241). Woodhead Publishing. https://doi.org/10.1016/B978-0-08-100431-9.00009-7

Alruwaili, M., Lopez, J. A., McCarthy, K., Reynaud, E. G., & Rodriguez, B. J. (2019). Liquid-phase 3D bioprinting of gelatin alginate hydrogels: influence of printing parameters on hydrogel line width and layer height. Bio-Design and Manufacturing, 2(3), 172–180. https://doi.org/10.1007/s42242-019-00043-w

Barthelmé, S., & Tschumperlé, D. (2019). imager: an R package for image processing based on CImg. Journal of Open Source Software, 4(38), 1012. https://doi.org/10.21105/joss.01012

Berghmans, M., Thijs, S., Cornette, M., Berghmans, H., De Schryver, F. C., Moldenaers, P., & Mewis, J. (1994). Thermoreversible Gelation of Solutions of Syndiotactic Poly(methyl methacrylate) in Toluene: A Two-Step Mechanism. Macromolecules, 27(26), 7669–7676. https://doi.org/10.1021/ma00104a023

Blaber, J., Adair, B., & Antoniou, A. (2015). Ncorr: Open-Source 2D Digital Image Correlation Matlab Software. Experimental Mechanics, 55(6), 1105–1122. https://doi.org/10.1007/s11340-015-0009-1

Breiman, L. (2001). Random forests. Machine learning, 45(1), 5-32. https://doi.org/10.1023/A:1010933404324

Burey, P., Bhandari, B. R., Howes, T., & Gidley, M. J. (2008). Hydrocolloid Gel Particles: Formation, Characterization, and Application. Critical Reviews in Food Science and Nutrition, 48(5), 361–377. https://doi.org/10.1080/10408390701347801

Canny, J. (1986). A computational approach to edge detection. IEEE Transactions on pattern analysis and machine intelligence 6, 679-698. https://doi.org/10.1109/TPAMI.1986.4767851

Caulier, S., Doets, E., & Noort, M. (2020). An exploratory consumer study of 3D printed food perception in a real-life military setting. Food Quality and Preference, 86, 104001. https://doi.org/10.1016/j.foodqual.2020.104001

Celis-Morales, C., Livingstone, K. M., Marsaux, C. F., Macready, A. L., Fallaize, R., O'Donovan, C. B., Woolhead, C., Forster, H., Walsh, M. C., Navas-Carretero, S., San-Cristobal, R., Tsirigoti, L., Lambrinou, C. P., Mavrogianni, C., Moschonis, G., Kolossa, S., Hallmann, J., Godlewska, M., Surwiłło, A., … on behalf of the Food4Me Study. (2017). Effect of personalized nutrition on health-related behaviour change: Evidence from the Food4Me European randomized controlled trial. International Journal of Epidemiology, 46(2), 578–588. https://doi.org/10.1093/ije/dyw186

Chen, H., Xie, F., Chen, L., & Zheng, B. (2019). Effect of rheological properties of potato, rice and corn starches on their hot-extrusion 3D printing behaviors. Journal of Food Engineering, 244, 150–158. https://doi.org/10.1016/j.jfoodeng.2018.09.011

Chen, J., Mu, T., Goffin, D., Blecker, C., Richard, G., Richel, A., & Haubruge, E. (2019). Application of soy protein isolate and hydrocolloids based mixtures as promising food material in 3D food printing. Journal of Food Engineering, 261, 76–86. https://doi.org/10.1016/j.jfoodeng.2019.03.016

Chirico Scheele, S., Binks, M., Christopher, G., Maleky, F., & Egan, P. F. (2023). Printability, texture, and sensory trade-offs for 3D printed potato with added proteins and lipids. Journal of Food Engineering, 351, 111517. https://doi.org/10.1016/j.jfoodeng.2023.111517

Chirico Scheele, S., Hartmann, C., Siegrist, M., Binks, M., & Egan, P. F. (2022). Consumer assessment of 3d-printed food shape, taste, and fidelity using chocolate and marzipan materials. 3D Printing and Additive Manufacturing, 9(6), 473–482. https://doi.org/10.1089/3dp.2020.0271

Chow, C. Y., Thybo, C. D., Sager, V. F., Riantiningtyas, R. R., Bredie, W. L. P., & Ahrné, L. (2021). Printability, stability and sensory properties of protein-enriched 3D-printed lemon mousse for personalised in-between meals. Food Hydrocolloids, 120, 106943. https://doi.org/10.1016/j.foodhyd.2021.106943

Comminal, R., Serdeczny, M. P., Pedersen, D. B., & Spangenberg, J. (2019). Motion planning and numerical simulation of material deposition at corners in extrusion additive manufacturing. Additive Manufacturing, 29, 100753. https://doi.org/10.1016/j.addma.2019.06.005

Costakis, W. J., Rueschhoff, L. M., Diaz-Cano, A. I., Youngblood, J. P., & Trice, R. W. (2016). Additive manufacturing of boron carbide via continuous filament direct ink writing of aqueous ceramic suspensions. Journal of the European Ceramic Society, 36(14), 3249–3256. https://doi.org/10.1016/j.jeurceramsoc.2016.06.002

Dankar, I., Haddarah, A., Omar, F. E. L., Sepulcre, F., & Pujolà, M. (2018). 3D printing technology: The new era for food customization and elaboration. Trends in Food Science & Technology, 75, 231–242. https://doi.org/10.1016/j.tifs.2018.03.018

Derkach, S. R., Ilyin, S. O., Maklakova, A. A., Kulichikhin, V. G., & Malkin, A. Y. (2015). The rheology of gelatin hydrogels modified by κ-carrageenan. LWT - Food Science and Technology, 63(1), 612–619. https://doi.org/10.1016/j.lwt.2015.03.024

Derossi, A., Caporizzi, R., Paolillo, M., & Severini, C. (2021). Programmable texture properties of cereal-based snack mediated by 3D printing technology. Journal of Food Engineering, 289, 110160. https://doi.org/10.1016/j.jfoodeng.2020.110160

Derossi, A., Caporizzi, R., Paolillo, M., Oral, M. O., & Severini, C. (2021). Drawing the scientific landscape of 3D Food Printing. Maps and interpretation of the global information in the first 13 years of detailed experiments, from 2007 to 2020. Innovative Food Science & Emerging Technologies, 70, 102689. https://doi.org/10.1016/j.ifset.2021.102689

Elbadawi, M., Castro, B. M., Gavins, F. K., Ong, J. J., Gaisford, S., Pérez, G., ... & Goyanes, A. (2020). M3DISEEN: A novel machine learning approach for predicting the 3D printability of medicines. International Journal of Pharmaceutics, 590, 119837. https://doi.org/10.1016/j.ijpharm.2020.119837

Ertay, D.S., Yuen, A., Altintas, Y. (2018). Synchronized material deposition rate control with path velocity on fused filament fabrication machines. Additive Manufacturing 19, 205–213. https://doi.org/10.1016/j.addma.2017.05.011

Fabra, M. J., Talens, P., & Chiralt, A. (2008). Tensile properties and water vapor permeability of sodium caseinate films containing oleic acid–beeswax mixtures. Journal of Food Engineering, 85(3), 393–400. https://doi.org/10.1016/j.jfoodeng.2007.07.022

Fahmy, A. R., Amann, L. S., Dunkel, A., Frank, O., Dawid, C., Hofmann, T., Becker, T., & Jekle, M. (2021). Sensory design in food 3D printing – Structuring, texture modulation, taste localization, and thermal stabilization. Innovative Food Science & Emerging Technologies, 102743. https://doi.org/10.1016/j.ifset.2021.102743

Fahmy, A. R., Becker, T., & Jekle, M. (2020). 3D printing and additive manufacturing of cereal-based materials: Quality analysis of starch-based systems using a camera-based morphological approach. Innovative Food Science & Emerging Technologies, 63, 102384. https://doi.org/10.1016/j.ifset.2020.102384

Fahmy, A. R., Vogt, U. T., Jekle, M., & Becker, T. (2022). Hardness targeted design and modulation of food textures in the elastic-regime using 3D printing of closed-cell foams in point lattice systems. Journal of Food Engineering, 320, 110942. https://doi.org/10.1016/j.jfoodeng.2022.110942

Fernandez, F., Compel, W. S., Lewicki, J. P., & Tortorelli, D. A. (2019). Optimal design of fiber reinforced composite structures and their direct ink write fabrication. Computer Methods in Applied Mechanics and Engineering, 353, 277–307. https://doi.org/10.1016/j.cma.2019.05.010

Ghazal, A. F., Zhang, M., & Liu, Z. (2019). Spontaneous Color Change of 3D Printed Healthy Food Product over Time after Printing as a Novel Application for 4D Food Printing. Food and Bioprocess Technology, 12(10), 1627–1645. https://doi.org/10.1007/s11947-019-02327-6

Go, J., & Hart, A. J. (2017). Fast Desktop-Scale Extrusion Additive Manufacturing. Additive Manufacturing, 18, 276–284. https://doi.org/10.1016/j.addma.2017.10.016

Go, J., Schiffres, S. N., Stevens, A. G., & Hart, A. J. (2017). Rate limits of additive manufacturing by fused filament fabrication and guidelines for high-throughput system design. Additive Manufacturing, 16, 1–11. https://doi.org/10.1016/j.addma.2017.03.007

Godoi, F. C., Prakash, S., & Bhandari, B. R. (2016). 3d printing technologies applied for food design: Status and prospects. Journal of Food Engineering, 179, 44–54. https://doi.org/10.1016/j.jfoodeng.2016.01.025

Greeff, G. P., & Schilling, M. (2017). Closed loop control of slippage during filament transport in molten material extrusion. Additive Manufacturing, 14, 31–38. https://doi.org/10.1016/j.addma.2016.12.005

Guo, C., Zhang, M., & Devahastin, S. (2021). Color/aroma changes of 3D-Printed buckwheat dough with yellow flesh peach as triggered by microwave heating of gelatin-gum Arabic complex coacervates. Food Hydrocolloids, 112, 106358. https://doi.org/10.1016/j.foodhyd.2020.106358

Guo, C., Zhang, M., Devahastin, S. (2020). 3D extrusion-based printability evaluation of selected cereal grains by computational fluid dynamic simulation. Journal of Food Engineering 286, 110113. https://doi.org/10.1016/j.jfoodeng.2020.110113

Haavisto, S., Cardona, M.J., Salmela, J., Powell, R.L., McCarthy, M.J., Kataja, M., Koponen, A.I. (2017). Experimental investigation of the flow dynamics and rheology of complex fluids in pipe flow by hybrid multi-scale velocimetry. Experiments in Fluids 58, 158. https://doi.org/10.1007/s00348-017-2440-9

Hamilton, C. A., Alici, G., & in het Panhuis, M. (2018). 3D printing vegemite and marmite: redefining "breadboards". Journal of food engineering, 220, 83-88. https://doi.org/10.1016/j.jfoodeng.2017.01.008

Hao, L., Mellor, S., Seaman, O., Henderson, J., Sewell, N., & Sloan, M. (2010). Material characterisation and process development for chocolate additive layer manufacturing. Virtual and Physical Prototyping, 5(2), 57–64. https://doi.org/10.1080/17452751003753212

He, C., Zhang, M., & Devahastin, S. (2020). Investigation on Spontaneous Shape Change of 4D Printed Starch-Based Purees from Purple Sweet Potatoes As Induced by Microwave Dehydration. ACS Applied Materials & Interfaces, 12(34), 37896–37905. https://doi.org/10.1021/acsami.0c10899

He, Y., Yang, F., Zhao, H., Gao, Q., Xia, B., & Fu, J. (2016). Research on the printability of hydrogels in 3D bioprinting. Scientific Reports, 6(1), 1–13. https://doi.org/10.1038/srep29977

Hodgson, G., Ranellucci, A., & Moe, J. (2021). Slic3r Manual – Flow Math (Accessed 5 Jan 2021). http://manual.slic3r.org/advanced/flow-math

Huang, M., Zhang, M., & Bhandari, B. (2019). Assessing the 3D printing precision and texture properties of brown rice induced by infill levels and printing variables. Food and Bioprocess Technology, 12(7), 1185–1196. https://doi.org/10.1007/s11947-019-02287-x

Jayaprakash, S., Paasi, J., Pennanen, K., Flores Ituarte, I., Lille, M., Partanen, J., & Sozer, N. (2020). Techno-Economic Prospects and Desirability of 3D Food Printing: Perspectives of Industrial Experts, Researchers and Consumers. Foods, 9(12), Article 12. https://doi.org/10.3390/foods9121725

Kadival, A., Kour, M., Meena, D., & Mitra, J. (2022). Extrusion-based 3D food printing: printability assessment and improvement techniques. Food and Bioprocess Technology, 16, 987–1008. https://doi.org/10.1007/s11947-022-02931-z

Kamlow, M.-A., Vadodaria, S., Gholamipour-Shirazi, A., Spyropoulos, F., & Mills, T. (2021). 3D printing of edible hydrogels containing thiamine and their comparison to cast gels. Food Hydrocolloids, 116, 106550. https://doi.org/10.1016/j.foodhyd.2020.106550

Kapoor, R., & Metzger, L. E. (2008). Process Cheese: Scientific and Technological Aspects—A Review. Comprehensive Reviews in Food Science and Food Safety, 7(2), 194–214. https://doi.org/10.1111/j.1541-4337.2008.00040.x

Keong, B. A. W., & Hua, R. Y. C. (2018). A novel fold-based design approach toward printable soft robotics using flexible 3d printing materials. Advanced Materials Technologies, 3(2), 1700172. https://doi.org/10.1002/admt.201700172

Kim, E. H.-J., Corrigan, V. K., Wilson, A. J., Waters, I. R., Hedderley, D. I., & Morgenstern, M. P. (2012). Fundamental Fracture Properties Associated with Sensory Hardness of Brittle Solid Foods. Journal of Texture Studies, 43(1), 49–62. https://doi.org/10.1111/j.1745-4603.2011.00316.x

Kim, H. W., Lee, I. J., Park, S. M., Lee, J. H., Nguyen, M.-H., & Park, H. J. (2019). Effect of hydrocolloid addition on dimensional stability in post-processing of 3D printable cookie dough. LWT, 101, 69–75. https://doi.org/10.1016/j.lwt.2018.11.019

Kim, H. W., Lee, J. H., Park, S. M., Lee, M. H., Lee, I. W., Doh, H. S., & Park, H. J. (2018). Effect of hydrocolloids on rheological properties and printability of vegetable inks for 3d food printing. Journal of Food Science, 83(12), 2923–2932. https://doi.org/10.1111/1750-3841.14391

Kuhn, M. (2008). Building predictive models in R using the caret package. Journal Of Statistical Software. 28(5), 1-26. https://doi.org/10.18637/jss.v028.i05

Kuo, M.-I., Wang, Y.-C., & Gunasekaran, S. (2000). A Viscoelasticity Index for Cheese Meltability Evaluation. Journal of Dairy Science, 83(3), 412–417. https://doi.org/10.3168/jds.S0022-0302(00)74897-1

Lanaro, M., Forrestal, D. P., Scheurer, S., Slinger, D. J., Liao, S., Powell, S. K., & Woodruff, M. A. (2017). 3D printing complex chocolate objects: Platform design, optimization and evaluation. Journal of Food Engineering, 215, 13–22. https://doi.org/10.1016/j.jfoodeng.2017.06.029

Le Tohic, C., O'Sullivan, J. J., Drapala, K. P., Chartrin, V., Chan, T., Morrison, A. P., Kerry, J. P., & Kelly, A. L. (2018). Effect of 3D printing on the structure and textural properties of processed cheese. Journal of Food Engineering, 220, 56–64. https://doi.org/10.1016/j.jfoodeng.2017.02.003

Le-Bail, A., Maniglia, B. C., & Le-Bail, P. (2020). Recent advances and future perspective in additive manufacturing of foods based on 3D printing. Current Opinion in Food Science, 35, 54-64. https://doi.org/10.1016/j.cofs.2020.01.009

Lee, A. Y., Pant, A., Pojchanun, K., Lee, C. P., An, J., Hashimoto, M., Tan, U.-X., Leo, C. H., Wong, G., Chua, C. K., & Zhang, Y. (2021). Three-Dimensional Printing of Food Foams Stabilized by Hydrocolloids for Hydration in Dysphagia. International Journal of Bioprinting, 7(4), 393. https://doi.org/10.18063/ijb.v7i4.393

Lee, S. K., Anema, S., & Klostermeyer, H. (2004). The influence of moisture content on the rheological properties of processed cheese spreads. International Journal of Food Science and Technology, 39(7), 763–771. https://doi.org/10.1111/j.1365-2621.2004.00842.x

Lin, Y.-J., Punpongsanon, P., Wen, X., Iwai, D., Sato, K., Obrist, M., & Mueller, S. (2020). FoodFab: Creating Food Perception Illusions using Food 3D Printing. Proceedings of the 2020 CHI Conference on Human Factors in Computing Systems, 1–13. https://doi.org/10.1145/3313831.3376421

Lipton, J. I., Cutler, M., Nigl, F., Cohen, D., & Lipson, H. (2015). Additive manufacturing for the food industry. Trends in Food Science & Technology, 43(1), 114–123. https://doi.org/10.1016/j.tifs.2015.02.004

Liu, Q., Zhang, N., Wei, W., Hu, X., Tan, Y., Yu, Y., Deng, Y., Bi, C., Zhang, L., Zhang, H. (2020). Assessing the dynamic extrusion-based 3D printing process for power-law fluid using numerical simulation. Journal of Food Engineering 275, 109861. https://doi.org/10.1016/j.jfoodeng.2019.109861

Liu, Y., Yu, Y., Liu, C., Regenstein, J.M., Liu, X., Zhou, P. (2019). Rheological and mechanical behavior of milk protein composite gel for extrusion-based 3D food printing. LWT 102, 338–346. https://doi.org/10.1016/j.lwt.2018.12.053

Liu, Z., & Zhang, M. (2021). Texture properties of microwave post-processed 3D printed potato snack with different ingredients and infill structure. Future Foods, 3, 100017. https://doi.org/10.1016/j.fufo.2021.100017

Liu, Z., Bhandari, B., Prakash, S., Mantihal, S., & Zhang, M. (2019). Linking rheology and printability of a multicomponent gel system of carrageenan-xanthan-starch in extrusion based additive manufacturing. Food Hydrocolloids, 87, 413–424. https://doi.org/10.1016/j.foodhyd.2018.08.026

Liu, Z., Dick, A., Prakash, S., Bhandari, B., & Zhang, M. (2020). Texture Modification of 3D Printed Air-Fried Potato Snack by Varying Its Internal Structure with the Potential to Reduce Oil Content. Food and Bioprocess Technology, 13(3), 564–576. https://doi.org/10.1007/s11947-020-02408-x

Liu, Z., Liu, J., Zhang, M., Liu, J., & Huang, W. (2023). Study of three-point bending behaviors of composite sandwich structure with re-entrant honeycomb cores. Polymer Composites, 44(1), 673–684. https://doi.org/10.1002/pc.27128

Liu, Z., Zhang, M., & Yang, C. (2018). Dual extrusion 3D printing of mashed potatoes/strawberry juice gel. LWT, 96, 589–596. https://doi.org/10.1016/j.lwt.2018.06.014

Liu, Z., Zhang, M., & Ye, Y. (2020). Indirect prediction of 3D printability of mashed potatoes based on LF-NMR measurements. Journal of Food Engineering, 287, 110137. https://doi.org/10.1016/j.jfoodeng.2020.110137

Liu, Z., Zhang, M., Bhandari, B., & Wang, Y. (2017). 3D printing: Printing precision and application in food sector. Trends in Food Science & Technology, 69, 83–94. https://doi.org/10.1016/j.tifs.2017.08.018

Loveday, S. M., Rao, M. A., Creamer, L. K., & Singh, H. (2010). Rheological Behavior of High-Concentration Sodium Caseinate Dispersions. Journal of Food Science, 75(2), N30–N35. https://doi.org/10.1111/j.1750-3841.2009.01493.x

Lucas, B.D. and Kanade, T., 1981. An iterative image registration technique with an application to stereo vision 81, 674-679

Lucey, J. A., Johnson, M. E., & Horne, D. S. (2003). Invited Review: Perspectives on the Basis of the Rheology and Texture Properties of Cheese. Journal of Dairy Science, 86(9), 2725–2743. https://doi.org/10.3168/jds.S0022-0302(03)73869-7

Ma, Y., & Zhang, L. (2022). Formulated food inks for extrusion-based 3D printing of personalized foods: A mini review. Current Opinion in Food Science, 44, 100803. https://doi.org/10.1016/j.cofs.2021.12.012

Ma, Y., Potappel, J., Chauhan, A., Schutyser, M. A. I., Boom, R. M., & Zhang, L. (2023). Improving 3D food printing performance using computer vision and feedforward nozzle motion control. Journal of Food Engineering, 339, 111277. https://doi.org/10.1016/j.jfoodeng.2022.111277

Ma, Y., Schlangen, M., Potappel, J., Zhang, L., & van der Goot, A. J. (n.d.). Quantitative characterizations of visual fibrousness in meat analogues using automated image analysis. Journal of Texture Studies, n/a(n/a). https://doi.org/10.1111/jtxs.12806

Ma, Y., Schutyser, M. A. I., Boom, R. M., & Zhang, L. (2021). Predicting the extrudability of complex food materials during 3D printing based on image analysis and gray-box data-driven modelling. Innovative Food Science & Emerging Technologies, 73, 102764. https://doi.org/10.1016/j.ifset.2021.102764

Ma, Y., Schutyser, M. A. I., Boom, R. M., & Zhang, L. (2022). Thermographic and rheological characterization of viscoelastic materials for hot-extrusion 3D food printing. Innovative Food Science & Emerging Technologies, 81, 103135. https://doi.org/10.1016/j.ifset.2022.103135

Maldonado-Rosas, R., Pérez-Castillo, J. L., Cuan-Urquizo, E., & Tejada-Ortigoza, V. (2024). The role of controlled voids shape on the flexural properties of 3D printed food: An approach for tailoring their mechanical properties. Virtual and Physical Prototyping, 19(1), e2284816. https://doi.org/10.1080/17452759.2023.2284816

Mantihal, S., Prakash, S., & Bhandari, B. (2019). Texture-modified 3D printed dark chocolate: Sensory evaluation and consumer perception study. Journal of Texture Studies, 50(5), 386–399. https://doi.org/10.1111/jtxs.12472

Marvin, H. J. P., Bouzembrak, Y., van der Fels-Klerx, H. J., Kempenaar, C., Veerkamp, R., Chauhan, A., Stroosnijder, S., Top, J., Simsek-Senel, G., Vrolijk, H., Knibbe, W. J., Zhang, L., Boom, R., & Tekinerdogan, B. (2022). Digitalisation and Artificial Intelligence for sustainable food systems. Trends in Food Science & Technology, 120, 344–348. https://doi.org/10.1016/j.tifs.2022.01.020

McHugh, M. L. (2012). Interrater reliability: The kappa statistic. Biochemia Medica, 22(3), 276–282. https://doi.org/10.11613/bm.2012.031

Michel, C., Velasco, C., Gatti, E., & Spence, C. (2014). A taste of Kandinsky: Assessing the influence of the artistic visual presentation of food on the dining experience. Flavour, 3, 1-11. https://doi.org/10.1186/2044-7248-3-7

Moetazedian, A., Budisuharto, A.S., Silberschmidt, V.V., Gleadall, A (2020). CONVEX (CONtinuously Varied EXtrusion): a new scale of design for additive manufacturing. Additive Manufacturing 101576. https://doi.org/10.1016/j.addma.2020.101576

Montoya, J., Medina, J., Molina, A., Gutiérrez, J., Rodríguez, B., Marín, R. (2021). Impact of viscoelastic and structural properties from starch-mango and starch-arabinoxylans hydrocolloids in 3D food printing. Additive Manufacturing 39, 101891. https://doi.org/10.1016/j.addma.2021.101891

Moretti, M., Rossi, A., Senin, N. (2021). In-process simulation of the extrusion to support optimisation and real-time monitoring in fused filament fabrication. Additive Manufacturing 38, 101817. https://doi.org/10.1016/j.addma.2020.101817

Nijdam, J. J., Agarwal, D., & Schon, B. S. (2021). Assessment of a novel window of dimensional stability for screening food inks for 3D printing. Journal of Food Engineering, 292, 110349. https://doi.org/10.1016/j.jfoodeng.2020.110349

Nuchitprasitchai, S., Roggemann, M., Pearce, J.M., 2017. Factors effecting real-time optical monitoring of fused filament 3D printing. Progress in Additive Manufacturing 2, 133–149. https://doi.org/10.1007/s40964-017-0027-x

Otsu, N. (1979). A Threshold Selection Method from Gray-Level Histograms. IEEE Transactions on Systems, Man, and Cybernetics, 9(1), 62–66. https://doi.org/10.1109/TSMC.1979.4310076

Outrequin, T. C. R., Gamonpilas, C., Siriwatwechakul, W., & Sreearunothai, P. (2023). Extrusion-based 3D printing of food biopolymers: A highlight on the important rheological parameters to reach printability. Journal of Food Engineering, 342, 111371. https://doi.org/10.1016/j.jfoodeng.2022.111371

Pant, A., Lee, A. Y., Karyappa, R., Lee, C. P., An, J., Hashimoto, M., Tan, U.-X., Wong, G., Chua, C. K., & Zhang, Y. (2021). 3D food printing of fresh vegetables using food hydrocolloids for dysphagic patients. Food Hydrocolloids, 114, 106546. https://doi.org/10.1016/j.foodhyd.2020.106546

Park, H. W., Park, J. W., & Yoon, W. B. (2023). The Relationship between Penetration, Tension, and Torsion for the Fracture of Surimi Gels: Application of Digital Image Correlation (DIC). Processes, 11(1), Article 1. https://doi.org/10.3390/pr11010265

Paxton, N., Smolan, W., Böck, T., Melchels, F., Groll, J., & Jungst, T. (2017). Proposal to assess printability of bioinks for extrusion-based bioprinting and evaluation of rheological properties governing bioprintability. Biofabrication, 9(4), 044107. https://doi.org/10.1088/1758-5090/aa8dd8

Pérez, B., Nykvist, H., Brøgger, A. F., Larsen, M. B., & Falkeborg, M. F. (2019). Impact of macronutrients printability and 3D-printer parameters on 3D-food printing: A review. Food chemistry, 287, 249-257.

Petsiuk, A. L., & Pearce, J. M. (2020). Open source computer vision-based layer-wise 3D printing analysis. Additive Manufacturing, 36, 101473. https://doi.org/10.1016/j.addma.2020.101473

Petsiuk, A., & Pearce, J. M. (2022). Towards smart monitored AM: Open source in-situ layer-wise 3D printing image anomaly detection using histograms of oriented gradients and a physics-based rendering engine. Additive Manufacturing, 52, 102690. https://doi.org/10.1016/j.addma.2022.102690

Piovarci, M., Foshey, M., Xu, J., Erps, T., Babaei, V., Didyk, P., Rusinkiewicz, S., Matusik, W., & Bickel, B. (2022). Closed-loop control of direct ink writing via reinforcement learning. ACM Transactions on Graphics, 41(4), 1–10. https://doi.org/10.1145/3528223.3530144

Pranoto, Y., Lee, C. M., & Park, H. J. (2007). Characterizations of fish gelatin films added with gellan and κ-carrageenan. LWT - Food Science and Technology, 40(5), 766 – 774. https://doi.org/10.1016/j.lwt.2006.04.005

Pulatsu, E., Su, J.-W., Lin, J., & Lin, M. (2020). Factors affecting 3D printing and post-processing capacity of cookie dough. Innovative Food Science & Emerging Technologies, 61, 102316. https://doi.org/10.1016/j.ifset.2020.102316

Raak, N., Abbate, R. A., Alkhalaf, M., Lederer, A., Rohm, H., & Jaros, D. (2020). Concentration-triggered liquid-to-solid transition of sodium caseinate suspensions as a function of temperature and enzymatic cross-linking. Food Hydrocolloids, 101, 105464. https://doi.org/10.1016/j.foodhyd.2019.105464

Rajpal, R., K.p, L., & Gangadharan, K. V. (2018). Parametric studies on bending stiffness and damping ratio of Sandwich structures. Additive Manufacturing, 22, 583–591. https://doi.org/10.1016/j.addma.2018.05.039

Rando, P., & Ramaioli, M. (2021). Food 3D printing: Effect of heat transfer on print stability of chocolate. Journal of Food Engineering, 294, 110415. https://doi.org/10.1016/j.jfoodeng.2020.110415

Ross, M. M., Crowley, S. V., Crotty, S., Oliveira, J., Morrison, A. P., & Kelly, A. L. (2021). Parameters affecting the printability of 3D-printed processed cheese. Innovative Food Science & Emerging Technologies, 72, 102730. https://doi.org/10.1016/j.ifset.2021.102730

Roupas, P. (2008). Predictive modelling of dairy manufacturing processes. International Dairy Journal, 18(7), 741–753. https://doi.org/10.1016/j.idairyj.2008.03.009

Schlangen, M., Schlangen, E., & van der Goot, A. J. (2023). Advanced tensile testing as a new tool to quantify properties of food. Current Research in Food Science, 7, 100577. https://doi.org/10.1016/j.crfs.2023.100577

Schutyser, M. A. I., Houlder, S., de Wit, M., Buijsse, C. A. P., & Alting, A. C. (2018). Fused deposition modelling of sodium caseinate dispersions. Journal of Food Engineering, 220, 49–55. https://doi.org/10.1016/j.jfoodeng.2017.02.004

Schwab, A., Levato, R., D'Este, M., Piluso, S., Eglin, D., & Malda, J. (2020). Printability and shape fidelity of bioinks in 3D bioprinting. Chemical Reviews, 120(19), 11028-11055. https://doi.org/10.1021/acs.chemrev.0c00084

Serdeczny, M.P., Comminal, R., Mollah, Md.T., Pedersen, D.B., Spangenberg, J. (2020a). Numerical modeling of the polymer flow through the hot-end in filament-based material extrusion additive manufacturing. Additive Manufacturing 36, 101454. https://doi.org/10.1016/j.addma.2020.101454

Serdeczny, M.P., Comminal, R., Pedersen, D.B., Spangenberg, J. (2020b). Experimental and analytical study of the polymer melt flow through the hot-end in material extrusion additive manufacturing. Additive Manufacturing 32, 100997. https://doi.org/10.1016/j.addma.2019.100997

Severini, C., Azzollini, D., Albenzio, M., & Derossi, A. (2018). On printability, quality and nutritional properties of 3D printed cereal based snacks enriched with edible insects. Food Research International, 106, 666–676. https://doi.org/10.1016/j.foodres.2018.01.034

Severini, C., Derossi, A., & Azzollini, D. (2016). Variables affecting the printability of foods: Preliminary tests on cereal-based products. Innovative Food Science & Emerging Technologies, 38, 281–291. https://doi.org/10.1016/j.ifset.2016.10.001

Severini, C., Derossi, A., Ricci, I., Caporizzi, R., & Fiore, A. (2018). Printing a blend of fruit and vegetables. New advances on critical variables and shelf life of 3D edible objects. Journal of Food Engineering, 220, 89–100. https://doi.org/10.1016/j.jfoodeng.2017.08.025

Shahbazi, M., Jäger, H., & Ettelaie, R. (2021). Application of Pickering emulsions in 3D printing of personalized nutrition. Part II: Functional properties of reduced-fat 3D printed cheese analogues. Colloids and Surfaces A: Physicochemical and Engineering Aspects, 624, 126760. https://doi.org/10.1016/j.colsurfa.2021.126760

Sharma, P., Munro, P. A., Gillies, G., Wiles, P. G., & Dessev, T. T. (2017). Changes in creep behavior and microstructure of model Mozzarella cheese during working. LWT - Food Science and Technology, 83, 184–192. https://doi.org/10.1016/j.lwt.2017.05.003

Siacor, F. D. C., Chen, Q., Zhao, J. Y., Han, L., Valino, A. D., Taboada, E. B., Caldona, E. B., & Advincula, R. C. (2021). On the additive manufacturing (3D printing) of viscoelastic materials and flow behavior: From composites to food manufacturing. Additive Manufacturing, 45, 102043. https://doi.org/10.1016/j.addma.2021.102043

Sombatsompop, N., Dangtangee, R., 2002. Effects of the actual diameters and diameter ratios of barrels and dies on the elastic swell and entrance pressure drop of natural rubber in capillary die flow. Journal of Applied Polymer Science 86, 1762–1772. https://doi.org/10.1002/app.11212

Sridharan, S., Meinders, M.B.J., Sagis, L.M., Bitter, J.H., Nikiforidis, C.V., 2021. Jammed Emulsions with Adhesive Pea Protein Particles for Elastoplastic Edible 3D Printed Materials. Advanced Functional Materials n/a, 2101749. https://doi.org/10.1002/adfm.202101749

Steffe, J. F. (1996). Rheological methods in food process engineering. Freeman press.

Sun, Y., Zhang, M., Chen, H. (2020). LF-NMR intelligent evaluation of rheology and printability for 3D printing of cookie dough pretreated by microwave. LWT 132, 109752. https://doi.org/10.1016/j.lwt.2020.109752

Tan, Y. J. N., Yong, W. P., Kochhar, J. S., Khanolkar, J., Yao, X., Sun, Y., Ao, C. K., & Soh, S. (2020). On-demand fully customizable drug tablets via 3D printing technology for personalized medicine. Journal of Controlled Release, 322, 42–52. https://doi.org/10.1016/j.jconrel.2020.02.046

Telea, A., & Jalba, A. (2011). Voxel-based assessment of printability of 3D shapes. In International symposium on mathematical morphology and its applications to signal and image processing (pp. 393-404). Springer, Berlin, Heidelberg. https://doi.org/10.1007/978-3-642-21569-8_34

Teng, X., Zhang, M., & Mujumdar, A. S. (2021). 4D printing: Recent advances and proposals in the food sector. Trends in Food Science & Technology, 110, 349–363. https://doi.org/10.1016/j.tifs.2021.01.076

Theagarajan, R., Moses, J. A., & Anandharamakrishnan, C. (2020). 3D Extrusion Printability of Rice Starch and Optimization of Process Variables. Food and Bioprocess Technology, 13(6), 1048–1062. https://doi.org/10.1007/s11947-020-02453-6

Thomar, P., Nicolai, T., Benyahia, L., & Durand, D. (2013). Comparative study of the rheology and the structure of sodium and calcium caseinate solutions. International Dairy Journal, 31(2), 100–106. https://doi.org/10.1016/j.idairyj.2013.02.005

Tian, X., Li, Y., Ma, D., Han, J., Xia, L. (2021). Closed-Loop Control of Silicone Extrusion-Based Additive Manufacturing Based on Machine Vision. Presented at the ASME 2021 16th International Manufacturing Science and Engineering Conference, American Society of Mechanical Engineers Digital Collection. https://doi.org/10.1115/MSEC2021-63719

Tong, W. Y., Ahmad Rafiee, A. R., Leong, C. R., Tan, W.-N., Dailin, D. J., Almarhoon, Z. M., Shelkh, M., Nawaz, A., & Chuah, L. F. (2023). Development of sodium alginate-pectin biodegradable active food packaging film containing cinnamic acid. Chemosphere, 336, 139212. https://doi.org/10.1016/j.chemosphere.2023.139212

Udyarajan, C. T., Horne, D. S., & Lucey, J. A. (2007). Use of time–temperature superposition to study the rheological properties of cheese during heating and cooling. International Journal of Food Science & Technology, 42(6), 686–698. https://doi.org/10.1111/j.1365-2621.2006.01468.x

Vadodaria, S. S., Warner, E., Norton, I., & Mills, T. B. (2021). Thermoreversible gels – Optimisation of processing parameters in fused Deposition Modelling. Colloids and Surfaces A: Physicochemical and Engineering Aspects, 618, 126399. https://doi.org/10.1016/j.colsurfa.2021.126399

Vancauwenberghe, V., Katalagarianakis, L., Wang, Z., Meerts, M., Hertog, M., Verboven, P., Moldenaers, P., Hendrickx, M.E., Lammertyn, J., Nicolaï, B. (2017). Pectin based food-ink formulations for 3-D printing of customizable porous food simulants. Innovative Food Science & Emerging Technologies 42, 138–150. https://doi.org/10.1016/j.ifset.2017.06.011

Venkatachalam, A., Balasubramaniam, A., Wilms, P. F. C., Zhang, L., & Schutyser, M. A. I. (2023). Impact of varying macronutrient composition on the printability of pea-based inks in extrusion-based 3D food printing. Food Hydrocolloids, 142, 108760. https://doi.org/10.1016/j.foodhyd.2023.108760

Verboven, P., Defraeye, T., Datta, A. K., & Nicolai, B. (2020). Digital twins of food process operations: The next step for food process models? Current Opinion in Food Science, 35, 79–87. https://doi.org/10.1016/j.cofs.2020.03.002

Vliet, T. van. (2013). Rheology and Fracture Mechanics of Foods. CRC Press.

Wedamulla, N. E., Fan, M., Choi, Y.-J., & Kim, E.-K. (2023). Effect of pectin on printability and textural properties of potato starch 3D food printing gel during cold storage. Food Hydrocolloids, 137, 108362. https://doi.org/10.1016/j.foodhyd.2022.108362

Wegrzyn, T.F., Golding, M., Archer, R.H. (2012). Food Layered Manufacture: A new process for constructing solid foods. Trends in Food Science & Technology 27, 66–72. https://doi.org/10.1016/j.tifs.2012.04.006

Wickham, H., Averick, M., Bryan, J., Chang, W., McGowan, L. D. A., François, R., ... & Yutani, H. (2019). Welcome to the Tidyverse. Journal of Open Source Software, 4(43), 1686. https://doi.org/10.21105/joss.01686

Williams, P. (2001). , Implementation of Near-infrared Technology. Near-infrared Technology in the Agricultural and Food Industries, and Edition.

Wilms, P., Daffner, K., Kern, C., Gras, S. L., Schutyser, M. A. I., & Kohlus, R. (2021). Formulation engineering of food systems for 3D-printing applications – A review. Food Research International, 148, 110585. https://doi.org/10.1016/j.foodres.2021.110585

Wright, M. N., & Ziegler, A. (2015). ranger: A fast implementation of random forests for high dimensional data in C++ and R. arXiv preprint arXiv:1508.04409. https://doi.org/10.18637/jss.v077.i01

Wu, P., Ramani, K.S., Okwudire, C.E. (2021). Accurate linear and nonlinear model-based feedforward deposition control for material extrusion additive manufacturing. Additive Manufacturing 48, 102389. https://doi.org/10.1016/j.addma.2021.102389

Xia, H., Lu, J., & Tryggvason, G. (2018). Fully resolved numerical simulations of fused deposition modeling. Part II – solidification, residual stresses and modeling of the nozzle. Rapid Prototyping Journal, 24(6), 973–987. https://doi.org/10.1108/RPJ-11-2017-0233

Yang, F., Zhang, M., Bhandari, B., & Liu, Y. (2018). Investigation on lemon juice gel as food material for 3D printing and optimization of printing parameters. LWT, 87, 67–76. https://doi.org/10.1016/j.lwt.2017.08.054

Zaharia, S. M., Enescu, L. A., & Pop, M. A. (2020). Mechanical Performances of Lightweight Sandwich Structures Produced by Material Extrusion-Based Additive Manufacturing. Polymers, 12(8), Article 8. https://doi.org/10.3390/polym12081740

Zeevi, D., Korem, T., Zmora, N., Israeli, D., Rothschild, D., Weinberger, A., Ben-Yacov, O., Lador, D., Avnit-Sagi, T., Lotan-Pompan, M., Suez, J., Mahdi, J. A., Matot, E., Malka, G., Kosower, N., Rein, M., Zilberman-Schapira, G., Dohnalová, L., Pevsner-Fischer, M., … Segal, E. (2015). Personalized Nutrition by Prediction of Glycemic Responses. Cell, 163(5), 1079–1094. https://doi.org/10.1016/j.cell.2015.11.001

Zeng, X., Li, T., Zhu, J., Chen, L., & Zheng, B. (2021). Printability improvement of rice starch gel via catechin and procyanidin in hot extrusion 3D printing. Food Hydrocolloids, 121, 106997. https://doi.org/10.1016/j.foodhyd.2021.106997

Zhang, J. Y., Pandya, J. K., McClements, D. J., Lu, J., & Kinchla, A. J. (2021). Advancements in 3D food printing: A comprehensive overview of properties and opportunities. Critical Reviews in Food Science and Nutrition, 0(0), 1–18. https://doi.org/10.1080/10408398.2021.1878103

Zhang, L., Versteege, S., Alting, A. C., & Schutyser, M. A. I. (2020). Impact of conjugation with maltodextrin on rheological properties of sodium caseinate. International Dairy Journal, 105, 104660. https://doi.org/10.1016/j.idairyj.2020.104660

Zhu, L., Spachos, P., Pensini, E., & Plataniotis, K. N. (2021). Deep learning and machine vision for food processing: A survey. Current Research in Food Science, 4, 233–249. https://doi.org/10.1016/j.crfs.2021.03.009

Zhu, S., Ribberink, M., de Wit, M., Schutyser, M., & Stieger, M. (2020). Modifying sensory perception of chocolate coated rice waffles through bite-to-bite contrast: An application case study using 3D inkjet printing. Food & Function, 11(12), 10580–10587. https://doi.org/10.1039/d0fo01787f

References

Zhu, S., Ruiz de Azua, I. V., Feijen, S., van der Goot, A. J., Schutyser, M., & Stieger, M. (2021). How macroscopic structure of 3D printed protein bars filled with chocolate influences instrumental and sensory texture. LWT, 151, 112155. https://doi.org/10.1016/j.lwt.2021.112155

Zhu, S., Stieger, M. A., van der Goot, A. J., & Schutyser, M. A. I. (2019). Extrusion-based 3D printing of food pastes: Correlating rheological properties with printing behaviour. Innovative Food Science & Emerging Technologies, 58, 102214. https://doi.org/10.1016/j.ifset.2019.102214

Summary

The food sector continuously explores innovative technologies to produce safe, healthy, and delicious, and sustainable food products to meet the evolving demands of consumers. There is a growing interest in personalized foods, capable of adapting food designs, sensory attributes, and nutritional values to individual needs. Producing personalized foods requires an on-demand process involving a deep understanding of food ingredient interactions, optimization of processing parameters, and the use of automated production techniques. 3D printing stands out as a promising method for personalized food production. However, 3D food printing as an emerging technology still suffers from low production throughput and a high production failure rate. The current 3D-printed foods require extensive development times and trial-and-error experiments to produce, hindering its market adoption. This thesis is dedicated to the development of monitoring, evaluation, and optimization strategies to streamline the 3D food printing process and achieve the "first-time-right" manufacturing goal. Leveraging machine vision techniques and predictive modeling principles, the studies discussed in this thesis aim at enhancing the current performance of 3D food printing to streamline it for the consumer market.

Chapter 2 outlines the existing landscape of 3D food printing for personalized food production. 3D food printing applications modify infill density and spatial distributions of flavor ingredients to achieve texture and flavor customizations. The chapter suggests that future studies need to collect longitudinal consumer preference of consuming 3D-printed foods, and the development of robust 3D printers is needed to produce personalized foods timely and accurately. Based on the learnings, the subsequent chapters developed various strategies to streamline the 3D food printing process using machine vision technologies and predictive modelling.

In **Chapter 3**, an automated image analysis tool was developed to assess the extrudability of various food materials exhibiting different shear-thinning behavior. The relationship between the printing pressure and volumetric flow rate followed a power-law pattern, reflecting the extent of shear-thinning in the food materials. The obtained extrudability data were linked to the shear-thinning properties and printing parameters using data-driven models. A combination of mechanistic parameters and experimental data yielded an effective prediction model to determine optimal printing parameters. This establishes a predictive framework that allows for the quantitative assessment and prediction of extrudability in the

3D printing of intricate food materials. Building on the insights of material extrudability, **Chapter 4** introduced a computer vision tool designed to measure extrusion rate and filament width during 3D food printing. Data obtained from this tool were used to optimize the nozzle motion, which ultimately improved layer deposition accuracy and layer stability. This approach can be easily integrated into current 3D food printers in a modular fashion, improving the printing accuracy of various food materials exhibiting diverse rheological properties.

After understanding the material extrudability and flow, **Chapter 5** utilized an infrared camera to monitor and assess the stability of 3D-printed food structures. The infrared videos recorded the deformation process of various food printing materials and identified a critical surface temperature, above which the structure collapses. The observed deformation and surface temperature data were connected to instrumental rheological tests, which indicated that insufficient cooling and extended printing time led to deformation of 3D-printed food structures. Thermographic and rheological measurements complement each other to improve both material formulations and in-situ printing control for 3D food printing.

Chapter 6 evaluated the layer printing accuracy using automated image analysis. A layer-wise approach was applied to quantify the 3D printing accuracy by comparing the printed and designed layers. The measured layer printing error was then contextualized by a human evaluation panel. The human-perceived errors supported the results from the automated image analysis, indicating over-extrusion as the primary source of inaccurate printing. However, consistent under-extrusion across the layer was not identified as a source of printing inaccuracy based on human assessment. Such an automated and contextualized method can lead to rapid and more meaningful monitoring of 3D food printing accuracy.

After understanding the extrudability, layer stability, and layer accuracy, **Chapter 7** explored image analysis to guide the design of 3D-printed food structures. The impact of infill designs to texture properties was systematically studied in a 3D-printed snack bar application. The fracture mechanics of the snack bars showed that the infill angle is an effective parameter to modulate the flexural properties. Digital image correlation can thus guide the modification of the infill design to achieve a range of flexural properties when 3D-

printing new snack bars. Such a vision-guided approach shows the synergy between experimental observation and the rapid iteration capability of 3D food printing to customize food textures.

Finally, **Chapter 8** reflected on synchronizing material flow and nozzle motion to achieve well-printed 3D food structures. The discussion further included methods of digitally optimizing other food processes such as high temperature shear cell, inspired by the work done in thesis on 3D food printing. Different vision-based methods were combined and outlined into a streamlined 3D food printing operation, which provides a pathway to develop a market-ready 3D food printer.

This thesis reports on the development of a set of machine vision techniques aimed at streamlining the 3D food printing process, ensuring the accurate and timely production of foods with customized designs. By enhancing its efficiency, 3D food printing becomes more commercially viable as a personalized food production tool. With a robust 3D printer in place, it can empower longitudinal consumer studies to comprehensively evaluate the benefits of consuming personalized foods in terms of improving sensory experiences and overall well-being.

Appendix

Acknowledgements

I would like to express my sincere appreciation to the financial support of this thesis from the "Sectorplan Techniek Mechanical Engineering" administered by the Dutch government. Without this public investment, my thesis would not exist.

My supervisors, Lu, Maarten, and Remko, it has been an honor to share the same research vision with you. Thank you all for your support and guidance throughout and beyond this thesis.

My family put pieces in me. They have been supporting me living, studying, and working away from home since I was 16 years old. They shaped who I am today and continue to make great impacts on me. I inherited so much from them to become the person I am today.

For those who are reading this acknowledgement right now, I thank you. You could be a colleague, a friend, a professor, a student, or someone from the future who is interested in my work. Our physical and/or intellectual path has crossed at some point. I hope you find this book a good read.

About the author

Yizhou Ma (August 1995) was born and raised in Xi'an, China. Yizhou obtained his bachelor and master degrees in food science from University of Minnesota and Kansas State University, respectively. He worked as a research and development scientist at Gastrograph AI prior to joining Wageningen University as a PhD candidate in the field of food process engineering in 2020. His professional and personal pursuits center around global responsibility, data-driven research, and sustainable system design.

List of publications

This thesis:

Ma, Y., Schutyser, M. A., Boom, R. M., & Zhang, L., 2021. Predicting the extrudability of complex food materials during 3D printing based on image analysis and gray-box data-driven modelling. *Innovative Food Science & Emerging Technologies*, 73, 102764.

Ma, Y., & Zhang, L,. 2022. Formulated food inks for extrusion-based 3D printing of personalized foods: A mini review. *Current Opinion in Food Science*. 44,100803.

Ma, Y., Schutyser, M.A., Boom, R.M. & Zhang, L., 2022. Thermographic and rheological characterization of viscoelastic materials for hot-extrusion 3D food printing. *Innovative Food Science & Emerging Technologies*, 81, 103135.

Ma, Y., Potappel, J., Chauhan, A., Schutyser, M.A., Boom, R.M. & Zhang, L., 2023. Improving 3D food printing performance using computer vision and feedforward nozzle motion control. *Journal of Food Engineering*, 339, 111277.

Ma, Y., Potappel, J., Schutyser, M. A., Boom, R. M., & Zhang, L., 2023. Quantitative analysis of 3D food printing layer extrusion accuracy: Contextualizing automated image analysis with human evaluations. *Current Research in Food Science*, 100511.

Ma, Y., Schutyser, M. A. I., Boom, R. M., & Zhang, L., Modulating flexural properties of 3D-printed snack bars based on infill designs guided by visualized fracture mechanics (accepted for publication in *Virtual and Physical Prototyping*).

Other publications:

Ma, Y[1]., Schlangen, M[1]., Potappel, J., Zhang, L., & van der Goot, A. J., 2023. Quantitative characterizations of visual fibrousness in meat analogues using automated image analysis. *Journal of Texture Studies*. [1]shared first authorship.

Ma, Y., Zhang L., Automated monitoring and evaluation of food additive manufacturing (book chapter). *In Food additive manufacturing.* CRC Press. (submitted).

Training & professional activities

Discipline specific events	Organizing institute	Year
Rheology course	VLAG / FPH/PCC	2020
3d food printing conference	Jakajima	2020
NIZO plant protein conference	NIZO	2020
NIZO dairy conference	NIZO	2021
Conference on image analysis in agrofood industry	Dutch Chemometrics Society	2021
Big data analysis in the life sciences	VLAG	2021
EFFOST annual conference	EFFoST	2021
3d food printing conference	Jakajima	2021
AMIFOST	Amity University	2022
DFPI - annual event	Digital food processing initiative	2022
Food chemistry and technology conference	United Scientific Group	2022
3d food printing conference	Jakajima	2022
EFFOST annual conference	EFFoST	2023

General courses	Organizing institute	Year
VLAG PhD week	VLAG	2021
Research data management	WGS	2020
Philosophy and ethics of food science and technology	VLAG	2022
Advanced R programming	KU Leuven	2022
Career perspectives	WGS	2023
Scientific publishing	WGS	2023

Other activities	Organizing institute	Year
Preparation of PhD research proposal	FPE	2020
PhD study tour to Singapore	FPE	2022
Weekly group meetings	FPE	2020-24

Research conducted in this thesis is financially supported by “Sectorplan Techniek Mechanical Engineering”.

Cover design by DALL·E 3 with modifications from Yizhou Ma.